Erlend Fjøsne Nordstrand

The Metallurgical Foundation for Manufacturing of CeS-Based Grain Refiners for Steels

Thesis for the degree of Philosophiae Doctor

Trondheim, November 2009

Norwegian University of Science and Technology
Faculty of Natural Sciences and Technology
Department of Materials Science and Engineering

NTNU
Norwegian University of
Science and Technology

NTNU
Norwegian University of Science and Technology

Thesis for the degree of Philosophiae Doctor

Faculty of Natural Sciences and Technology
Department of Materials Science and Engineering

ISBN 978-82-471-1858-0 (printed ver.)
ISBN 978-82-471-1859-7 (electronic ver.)
ISSN 1503-8181

Doctoral theses at NTNU, 2009:227
IMT-Report 2009:119

Printed by NTNU-trykk

Preface

This doctoral thesis has been carried out at the Department of Materials Science and Engineering, the Norwegian University of Science and Technology, NTNU, over a four year period of time from August 2005 to August 2009.

The work is a part of the DISvaDRI (Dispersoids In Steel and value-added Direct Reduced Iron) project, where the focus has been on the manufacturing of grain refiners for steels and their applications in the iron- and steel industry. During the course of the work the author has attended one international conference and prepared two different journal publications, i.e.:

E. F. Nordstrand, Ø. Grong, C. van der Eijk and S. Gaal: "*Oxygen control during manufacturing of CeS-based grain refiners for steel*", Proc. 8th Int. Conf. on Molten Slags, Fluxes & Salts (Molten2009), GECAMIN Ltd., Santiago, Chile, (2009), 847, CD-ROM.

E. F. Nordstrand, Ø. Grong, C. van der Eijk and S. Gaal: "*Phase relations in Ce-Al-Fe-S based grain refiners for steels*", ISIJ Int., **49**(2009), 1051.

E. F. Nordstrand, Ø. Grong, C. van der Eijk and S. Gaal: "*Conditions for CeS formation during manufacturing of Ce-S-Al based grain refiners for steels*", ISIJ Int., **49**(November 2009).

These three publications constitute the main sections of Part II, III, and IV of the thesis. The different parts are autonomous in the sense that they can be red independently of each other, but are presented in a logical sequence to illuminate the progress of the work. Cross-references to the different parts are, however, provided in the text when this is considered to be relevant and appropriate for the context.

Trondheim, September 2009

Erlend Fjøsne Nordstrand

Acknowledgments

First of all, I would like to acknowledge the important contribution from Professor Øystein Grong, who has been my principal thesis supervisor. I am extremely grateful for his excellent supervision and his active role in this project. His interest, great support and encouragement during these years are highly appreciated.

I am also grateful to Dr. Casper van der Eijk and Dr. Sean Gaal at SINTEF-Materials and Chemistry for all valuable advice and great support during these four years.

Finally, I would like to thank Staff Engineer Morten Peder Raanes at the Department of Materials Science and Engineering, NTNU for carrying out the microprobe investigations.

Abstract

This doctoral thesis is concerned with experimental studies of the conditions for CeS formations during manufacturing of Ce-S/Ce-S-Al/Ce-S-Al-Fe based grain refiners for steels. The thesis is divided into five parts. **Part I** gives a general introduction to the concept of steel grain refinement by means of heterogeneous nucleation of acicular ferrite at non-metallic inclusions during the austenite to ferrite transformation.

In **Part II** the conditions for cerium oxide and oxysulphide formation during manufacturing of CeS-based grain refiners for steel have been examined. The small vacuum furnace used in these laboratory experiments is equipped with a graphite heating element, where both the temperature-time programme and the partial pressure of oxygen can be accurately controlled and monitored throughout the melting trials. The results from the optical and electron microprobe examinations of the as-solidified samples show that the liquid Ce-S-Fe-Al melt is prone to oxidation up to about 1600 to 1800 ˚C before the graphite heating element starts to act as an effective oxygen scavenger. The oxidation leads to conversion of CeS to Ce_2O_2S, which is an undesirable microconstituent in the grain refiners. In practice, the problem can be overcome by the use of rapid heating of the melt, which in the present small-scale laboratory experiments needs to be as high as 1000 ˚C/min in order to kinetically suppress the oxygen absorption from the shielding gas.

In **Part III** the phase relations within the Ce-Al-Fe-S system have been clarified, using a combination of optical microscopy and WDS microprobe analyses. As a starting point high-purity charge materials of cerium, aluminium and FeS_2 are melted and superheated to about 2000 ˚C within small tantalum crucibles inside a dedicated laboratory furnace filled with cleaned argon. The phases detected in the as-solidified samples were CeS, Ce_3Al, Fe_2Ce and γ-Ce, along with Ce_2O_2S, which is an undesirable microconstituent in CeS-based grain refiners. It is concluded that FeS_2 can be used as a sulphur source for addition up to about 4 wt% sulphur. At higher levels the Fe-Ta interaction becomes so vigorous that tantalum no longer acts as an inert refractory metal and wetting becomes a major problem. In contrast, aluminium is an essential alloying element in the sense that it prevents the grain refiners from disintegrating in contact with air due to internal oxidation of free cerium by promoting the formation of Ce_3Al.

In **Part IV** the phase relations within the Ce-S-Al system have been clarified, using a combination of optical microscopy and WDS microprobe analyses. As a starting point high-

purity charge materials of cerium, aluminium and Ce_2S_3 were melted and superheated to about 2000 ˚C within small tantalum crucibles inside a dedicated laboratory furnace filled with cleaned argon. The main constituent phases detected in the as-solidified samples are CeS, Ce_3Al, CeAl and γ-Ce, where the CeS phase constitutes a discontinuous dendritic network within the grain refiners. The melting experiments show that pure cerium can dissolve about 6 wt% of sulphur at 2000 ^oC which drops to approximately 1.8 wt% at 1500 ^oC. The measured sulphur solubility is considerable lower than that inferred from the existing binary Ce-S phase diagram, which therefore should be revised to comply with these new measurements. Because alloying with aluminium reduces the sulphur solubility in liquid cerium, the addition of this element should be restricted if a high volume fraction of CeS is desired in the grain refiners. At the same time the use of Ce_2S_3 as a sulphur source in replacement of pyrite (FeS_2) means that aluminium is not actually needed to prevent the grain refiners from disintegrating in contact with air due to internal oxidation.

Finally, in **Part V** up-scaled production of the CeS-based grain refiners has been attempted. As a starting point, batches of about 0.5 kg are made from high purity charge materials of γ-Ce and Ce_2S_3 within a suitable molybdenum crucible using an inductive heating chamber furnace filled with pure argon. Following casting in a water-cooled copper mould, the main phases observed in the as-solidified samples are γ-Ce and CeS. Also some Ce_2O_2S could be detected, but the amount is small, meaning that oxygen pick-up is not a major problem in these up-scaled melting experiments. Furthermore, attempts have been made to re-melt and rapidly solidify one of the produced grain refiners using melt spinning. The experiments show that a fine distribution of spherical-shaped CeS particles with a mean diameter close to 1 μm can be produced by means of this technique. This size is deemed to be optimal with respect to nucleation of acicular ferrite in steels during the austenite to ferrite transformation. Finally, a new and improved production method for CeS-based grain refiners has been suggested, which allows large quantities of materials to be melted, superheated and rapidly quenched in a single batch operation. The idea here is to use gas atomization as the main quenching technique for liquid cerium instead of melt spinning in combination with induction heating and bottom tapping of the crucible.

Table of contents

Part I: Effects of non-metallic inclusions on the microstructure and properties of low carbon structural steels – A literature review

1.1 Introduction

The production of steel has steadily increased since Bessemer in 1855 invented the mass-production of steel, leading to a total world crude steel production of 1,327 million metric tons (mmt) in 2008[1)]. The production of steel has grown steadily and 50% of all steel has been made in the last twenty five years[2)]. The consumption is likely to double again within the next twenty five years. Part of this growth will be possible using current manufacturing technology, but there seems to be a general agreement among the international steel manufactures that faster and cheaper ways to produce the steel are needed in the future.

In addition to cost, the development of new materials with improved mechanical properties is a key issue in steel research. To meet the demands for high performance materials the use of clean steel has normally been considered to be an advantage[3,4)]. The concept of clean steel has existed since the early sixties and involves removal of large inclusions that can act as initiation sites for microvoids and cleavage cracks during service in steel products[5)]. Inclusions can broadly be defined as non-metallic and sometimes intermetallic phases embedded in a metallic matrix, which derive from chemical reactions of the molten steel with its local environments[6)]. Undesired non-metallic inclusions in steel are therefore removed as completely as possible during the steelmaking process in order to improve the quality. This is done through advanced ladle refining treatments[7-9)] and non-metallic inclusion removal techniques[10,11)]. A very precise control of the number density and size distribution of the inclusions has led to a gradual and significant improvement of the steel cleanliness. Indeed, modern ladle metallurgy techniques have been referred to as "the backbone of future steelmaking"[12)].

The concept of clean steel is debatable as it leads us to believe that steel with the lowest possible inclusion content will be the superior one. This is not always true, and a balanced opinion regarding the permissible inclusion level is of great technical and economical importance for both steel producers and steel consumers. In aluminium and cast iron[13,14)], inclusions are widely used to control the microstructure. This is done by addition of a grain refining alloy to the melt, which allows casting of high-quality products in a single batch operation. It is also known from low-alloy steel weld metals that inclusions have a beneficial effect on the mechanical properties[15-18)]. This due to the intragranular nucleation of acicular ferrite at inclusions in the heat affected zone (HAZ), which results in a refined microstructure within the coarse-grained region adjacent to the fusion boundary. It is well known that a small grain size has a positive effect both on the yield strength and the toughness[19,22)]. In addition,

grain refinement can reduce centerline or interdendritic segregation during solidification, which means that problems with high temperature cracking can be minimized[20,21]. In wrought steel products grain refinement has traditionally been achieved through thermomechanical processing. Even in thick steel plates a grain size below 5 μm can be achieved[22], but this requires extensive thermomechanical treatment. Thus there is an enormous potential in energy saving if the thermomechanical processing chain could to be simplified, e.g. by combining thin slab or thin strip casting with modest rolling and conventional heat treatment. In that case, the grain refinement must be achieved by some other means, for example by intragranular nucleation of ferrite at dispersed particles, as in steel weld metals.

In the scientific literature, a lot of information exists on the effect of non-metallic inclusions on the acicular ferrite formation in wrought steel products[20,21,24-31]. It follows from the investigations that if the size distribution of these inclusions can be controlled during ladle refining and casting, a sound foundation for a new solid state possessing route for steel could be laid, where most of the grain refinement is achieved through intragranular nucleation of acicular ferrite at inclusions during the austenite to ferrite transformation.

1.2 The process route in modern steelmaking

The steelmaking process relies on raw materials from a number of sources such as iron ore, coke, limestone and recycled steel scrap. These materials contain impurities, which when added during the steelmaking process inevitably result in low levels of elements not desired in the final steel chemical composition. Modern primary and secondary steelmaking practices can reduce the level of these impurities to a very low level. Figure 1.1 shows schematically the process route in modern steelmaking.

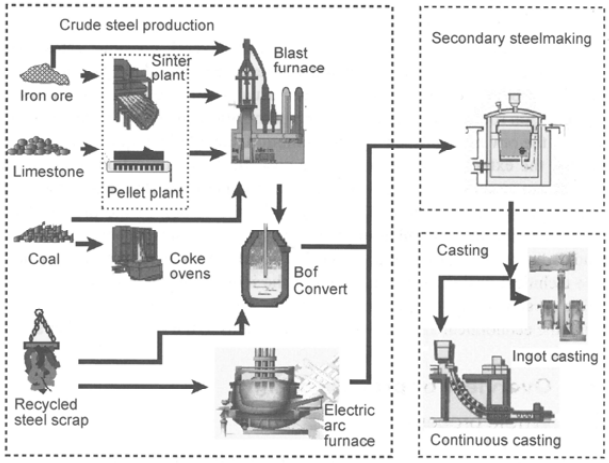

Figure 1.1 Sketch showing the process route in modern steelmaking, where steel scrap and molten iron from the blast furnace is charged into the basic oxygen or into the electric arc furnace in the primary steelmaking. The final compositional adjustments in the liquid steel are made in the secondary steelmaking through ladle refining. At the end the steel is teemed through a continuously casting process or ingot cast[32].

The first step is making pig iron from iron ore in the blast furnace. Second step is where steel scrap and molten iron from the blast furnace are charged into the basic oxygen or the electric arc furnaces, and is called the primary steelmaking. The final compositional adjustments in the liquid steel are made in the secondary steelmaking through ladle refining. At the end the steel is teemed through a continuously casting process or ingot cast.

1.2.1 Pig iron production in the blast furnace

Iron is a moderately reactive metal which joins readily with non-metals such as oxygen. This is why iron in the Earth's crust is found as an ore, in which iron is chemically combined with oxygen or other non-metals. Iron rich ore can be charged directly into a furnace without any further processing, but ore with lower iron content must be further processed through pelletizing before put into a furnace. Removing oxygen from the iron ore is the first step in the manufacture of steel and is done in a blast furnace. A simple sketch which shows the principle of a blast furnace can be seen in Figure 1.2.

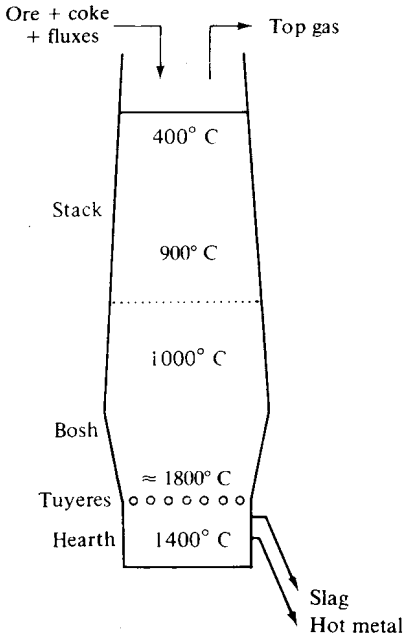

Figure 1.2 A simple sketch showing the principles of the Blast Furnace. Iron ore, fluxes and coke are put into the furnace from the top. Hot air is blasted into the furnace near the bottom making the coke burn, which starts a reaction between the carbon and the iron ore at different temperatures. When oxygen is removed from the iron ore, slag and carbon rich molten iron can be tapped off at the bottom of the furnace[33)].

The blast furnace is a large steel structure about 30 metres high and is lined with refractory firebricks that can withstand temperatures approaching 2000 °C. Iron ore, limestone and coke are charged through the top. Pre-heated air is blasted into the furnace at about 1000 °C through a nozzle near the bottom and ascends at the top after going through numerous chemical reactions. The iron oxide is reduced to molten iron using carbon monoxide gas, which descends from the combustion of coke and air[33)]. Once a blast furnace is started it will continuously run for about ten years with only short stops to perform planned maintenance, and can produce up to 13 000 tonns pig iron per day. Slag which contains sulphur and other impurities like alumina and manganesia that enters the furnace with the iron ore and coke are removed from the top of the molten iron. At the end the iron is tapped from the bottom of the blast furnace. The pig iron contains now between 4 and 4.5 wt% carbon and other impurities which make the metal too brittle for most engineering applications. The next step in the production of steel is to reduce the levels of carbon and other impurity elements in the hot metal.

1.2.2 Conversion of pig iron to steel in the basic oxygen furnace (BOF)

In the basic oxygen furnace the molten iron from the blast furnace is converted into liquid steel by reducing its high carbon content, and is known as primary steelmaking. The BOF generally operates on a charge of 75 percent hot metal and 25 percent scrap, and produce up to 160,000 tons of steel a month with a wide variety of carbon, alloy and high-strength chemistries. Figure 1.3 shows how oxygen is blown into the furnace through a water-cooled oxygen lance. This oxidises the carbon and other unwanted elements in the molten metal. At the same time inert stirring gases and/or oxygen are additionally injected through the converter bottom. The bottom blowing was initially introduced because of its high efficiency in enhancing the mass transfer process in molten steel[32].

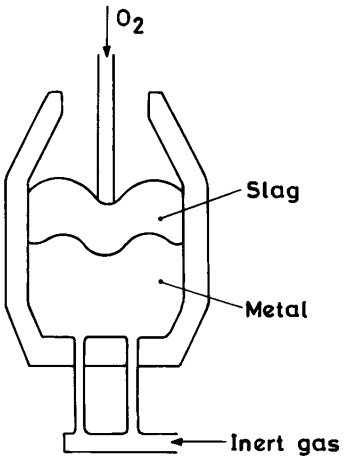

Figure 1.3 Schematic illustration of a Basic Oxygen Furnace (BOF). Pig iron from the blast furnace and along with some scarp metal is put into the furnace. The main purpose of this furnace is to remove the high amount of carbon which descends from the blast furnace process. This is done by blowing oxygen through the melt by using a water-cooled lance inserted through the mouth of the vessel[34].

The furnace needs no heating because the oxygen reacts exothermically with the impurity elements carbon, silicon and manganese. Carbon is oxidised to carbon monoxide gas, which passes from the converter to a cleaning plant and can be re-used as a fuel gas. The rest of the elements in the metal are converted to acidic oxides. They combine with the lime and other fluxes that are added during the blow and produce a slag that floats on the surface of the metal. The steel is tapped from the furnace when it is at the correct temperature and composition. The furnace is tilted and the molten steel runs out via a tap hole into a ladle. This will separate the molten steel from the lighter slag, which remains in the vessel and can be emptied into another

ladle as waste. The next step in the steel making process is to adjust the composition of the primary steel after the customer's specification, and is called secondary steelmaking.

1.2.3 Steel production in the electric arc furnace (EAF)

The Electric Arc Furnace offers an alternative method of bulk steel manufacture. It makes steel from what would otherwise be environmentally damaging scrap metals[35]. Most electric arc furnace installations are based upon the three phases (three electrodes) design, as shown in Figure 1.4. The steelmaking process involves four main steps, charging, melting, blowing and tapping.

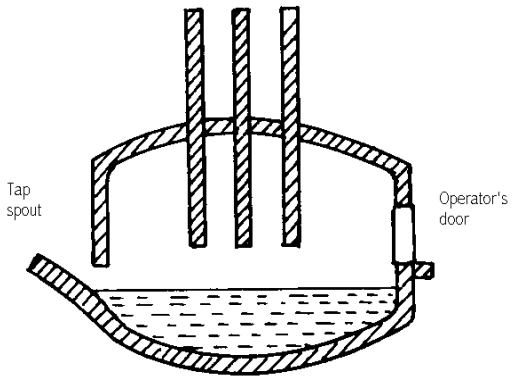

Figure 1.4 Schematic illustration of an Electric Arc Furnace (EAF). The EAF is mainly used to melt scrap, but also prereduced materials and pellets can be charged. The melting is done by an electric arc between the three electrodes and the metal. By tilting the vessel slag and molten steel can be poured into ladles through the operator's door and the tap spout[34].

The main advantage of the EAF lies in its flexibility in accepting a range of charge materials such as scrap, molten iron, prereduced materials and pellets in any proportions. The heat required for melting the scrap in this process is generated by electric arcs struck between carbon electrodes and the metal bath[33]. The control of electric power can be well exercised to impart heat to the bath at different desired rates. This allows a precise control of refining reactions[34]. Blowing oxygen through the melt is later done to oxidise elements such as carbon, silicon and manganese in the scrap metal, which will later float to the top. As in the BOF, carbon monoxide escape as a gas and the other unwanted elements combine with the added lime to make a top slag, which is poured off the surface through the operator's door, as shown in Figure 1.4. The last stage of the process is the tapping of the steel itself. This is done through the spout in the bottom of the furnace and into a ladle. The liquid in the ladle is now ready for secondary steelmaking and casting. Further treatments of the metal from the EAF take place in much the same way as steel from the BOF plant.

1.2.4 Secondary steelmaking

Changing the composition of the molten steel after tapping it from the BOF or EAF is called secondary steelmaking. This confines the final making of steel between the tapping and the teeming in a suitably equipped vessel. Such processes are also known by the terms ladle metallurgy and secondary refining processes. The purposes of secondary refining are many, but the main objectives are to fine-tune the chemical composition of the steel, to improve the homogenisation of temperature and to remove impurities and to reduce the number of inclusions[32]. A number of routes are available, but in general the process should facilitate operations such as stirring with argon or induction, adding alloys, vacuum degassing and arc heating[35-38].

1.2.4.1 Ladle stirring

The simplest form of secondary steelmaking facility is the argon stirring which involves bubbling argon through the steel by injecting gas through porous plugs in the ladle lining, as shown in Figure 1.5.

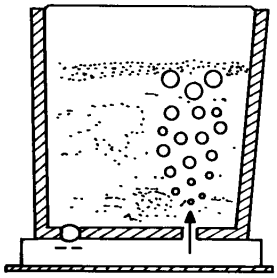

Figure 1.5 Schematic illustration showing the first step in the ladle refining process and involves stirring the molten steel by injecting argon gas through porous plugs in the ladle lining[34].

The stirring is a result of the expansion of the gas due to the heating and the decrease in pressure as gas rises, and homogenises the steel with respect to both temperature and composition. It will also significantly improve the cleanliness of the steel since the stirring encourages the oxide inclusions to float up[37]. As a result the oxygen content of the system goes down, but it also has a positive effect on hydrogen and nitrogen removal[37]. The gas stirring equipment allows addition of synthetic slag, which can assist in removal of impurities[36]. Another method of stirring is the electromagnetic stirring. The flow pattern is in general similar to that for gas stirring and is usually used to separate non-metallic inclusions from the steel. The electromagnetic stirring generally provides lower stirring energy than gas stirring, but the gas stirring has an advantage in its good reliability and lower operational cost[37].

1.2.4.2 Alloying injection

Injection of powder into the ladle was developed in the late sixties to produce very low sulphur steels. A schematic illustration of powder being injected in to the ladle through a lance is shown on the left in Figure 1.6.

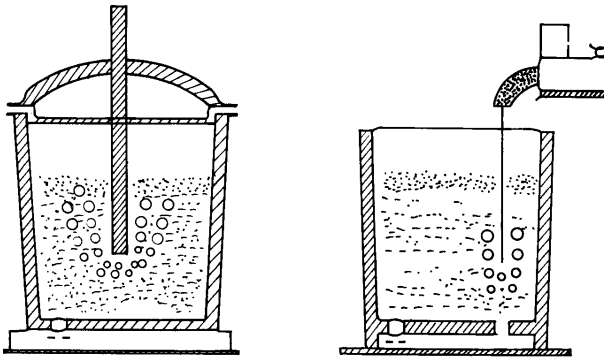

Figure 1.6 Sketches showing different alloying injection techniques. In the sketch on the left, powder is injected into the ladle through a lance with help from a carrier gas. To the right, alloying elements are introduced into the ladle through a cored wire, which is called "wire feeding"[34].

Argon is also in most cases injected, via the lance or through porous-plugs in the bottom, to aid the transportation of the added alloying elements. Sulphur particles have a tendency to elongate during rolling which reduces the thickness strength of the plates. Treatments with for example calcium silicide through powder injection, reduces the number of inclusions and converts those remaining into hard, globular, undeformable particles which are much less detrimental to product quality[36]. Injection of calcium silicide through a cored wire is now a days often preferred instead of powder injection. A schematic set-up of wire injection is also shown in Figure 1.6. The equipment usually consists of an uncoiler, feeder and a guide tube, and the wire can be as thick as 11 mm. There are several advantages with cored wire injection. The wire injection does not require a carrier gas, which results in less turbulence and hence lower nitrogen pick-up. The capital cost for the wire injection process is low as compared to that for powder injection[37].

1.2.4.3 Vacuum degassing

Originally, the vacuum degassing process was developed to reduce the hydrogen content in steel products. This reduced for example a lot of catastrophic cracking accidents seen in forged steel products[36]. The principle of the vacuum treatment is to expose the molten steel to low pressure for a longer period of time. Due to the decrease in the partial pressure of the dissolved gases, mainly hydrogen and nitrogen, they will form bubbles and rise to the top. There exist several

different vacuum treatment methods, but the oldest and one of the leading methods is the RH (recirculation degasser) process which was developed in the late fifties. A schematic illustration of the RH process is shown in Figure 1.7.

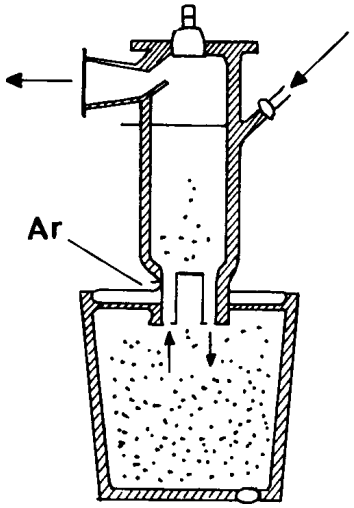

Figure 1.7 Principles of the RH process. The system consists of an upper chamber with a pumping system and with two legs at the bottom immersed into the ladle. Injection of argon into one of the legs causes the molten steel to circulate and the vacuum pump reduces the pressure down to 1 mbar. The degassing occurs when bubbles forms, due to the decrease in pressure, and rises to the surface. The hydrogen or the nitrogen gas that are formed escapes out of the chamber by the pumping system[34)].

The system consists of an upper chamber with a pumping system and with two legs immersed into the ladle. In the RH process the pressure inside the chamber is reduced down to 1 mbar by a strong pumping system[36)]. Argon is injected into one of the legs making the molten steel circulate between the upper chamber and the ladle. The bubbles that are formed rise to the top where they are being pumped away as the arrows in Figure 1.7 indicate. The RH process is a versatile technique and contributes not only to degassing, but also to deoxidation, decarburisation, alloying & trimming and homogenisation of temperature and composition[37)].

1.2.4.4 Ladle reheating

All the pre-treatment in the secondary steelmaking contributes in a decrease in temperature. This heat loss must be compensated either by super-heating of the molten steel in the primary steelmaking process or by using a ladle furnace, as shown in Figure 1.8.

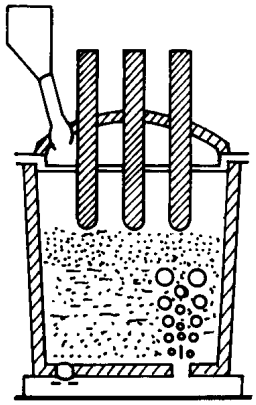

Figure 1.8 Schematic illustration of the ladle furnace. The equipment consists of three graphite electrodes which electrically reheat the molten steel in the ladle. Argon gas is injected from the bottom to ensure thermal transfer and alloying addition can be made through the top lid[34].

Also the continuous casting process has made the use of a ladle furnace more and more important, since it demands teeming temperatures up to 1750 °C[36]. The development of ladle reheating processes has brought a number of advantages. Reheating steel in the ladle allows more time for secondary steelmaking treatments, without the need for increasing tapping temperatures. The ladle furnace itself consists of a station in which steel in the ladle can be electrically reheated up to 4.5 K/min by graphite electrodes passing through a water cooled lid[36]. To ensure the thermal transfer argon gas is bubbled through the molten steel via porous plugs in the bottom. Alternatively, it can be injected through a lance from the top. Additions of alloying elements are usually possible in the ladle furnace through holes in the top lid, as shown in Figure 1.8.

1.2.5 Continuous casting

During the past thirty years the share of steel produced via the continuous casting route has increased remarkably. Compared to ingot casting, continuous casting brings the benefits of higher yield, lower rolling and energy costs, and improved quality. The casting process takes place after the secondary steelmaking. The liquid steel is first teemed into a tundish through a nozzle in the bottom of the ladle, and then from the tundish and down into a mould, as shown in Figure 1.9.

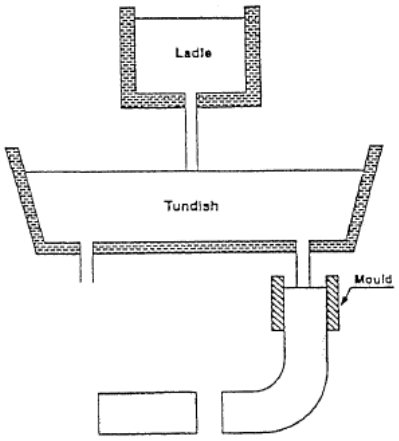

Figure 1.9 Simple sketch of the continuous casting process. First the molten steel is transferred from the ladle and into a tundish. The tundish then delivers continuously liquid steel to the mould at controlled rate[40].

The tundish was originally designed as an intermediate vessel between the ladle and the mould that serves to deliver liquid steel to the mould at controlled rate and to maintain a steady supply of liquid steel to the mould during ladle change[39]. Thus in recent years the continuous casting tundish has also evolved into an useful equipment for steel refining. A modern tundish is designed to carry out various metallurgical operations such as inclusion separation, flotation, alloy trimming, superheat control and homogenisation. These operations have gained considerable importance and are to day considered a separate area of secondary refining referred to as "tundish metallurgy"[40]. The mould it self is the most complex and critical component in the continuous casting process and has various functions[39]:

- Act as a substrate for the formation of thin, hot and crack-free solid shell
- Form the shape of the final product
- Extract heat from the strand at very high rates
- Facilitate the separation of non-metallics from the solidifying shell
- Allow adequate production rates without breakouts

1.3 Effects of non-metallic inclusions on steel properties

In the steelmaking process discussed in Section 1.2 impurities are constantly being removed throughout the whole process. Still some level of impurities will always exist in the metal no matter how good it is refined. These can be exogenous inclusions from accidental incorporation of particles of slag, refractories and dirt in the liquid steel. Alternatively, they can be indigenous inclusions, i.e. compounds of oxygen or sulphur that form in the liquid steel as a result of

decreasing solubility with decreasing temperature[45]. These inclusions can have several negative effects on steels properties, such as reduced fracture strength and increased transition-temperature.

The fracture mechanisms in low alloy steel can be classified into two general categories, ductile fracture[3,41,45-49] and brittle fracture[41-45,50-53,56,58]. Both fracture mechanisms are associated with the presence of secondary phase particles. These particles can lead to the formation of small cracks or voids in the steel matrix, either by decohesion between the matrix/particle interfaces or by fracture of the particle itself[45,46,49,53], as shown in Figure 1.10(a) and 1.10(b), respectively.

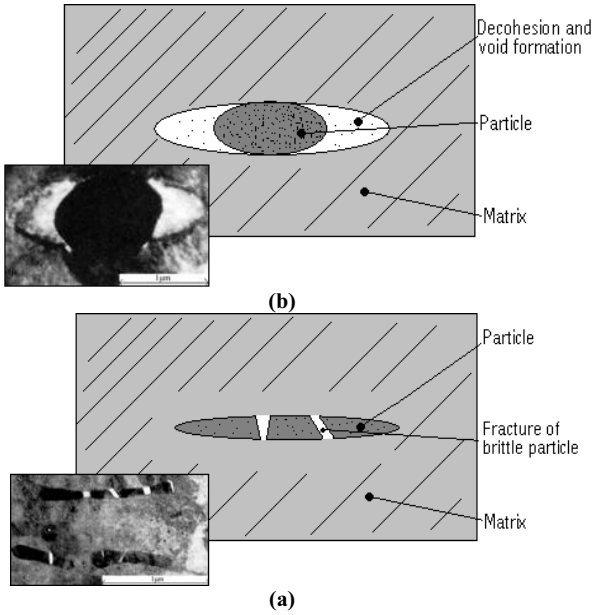

Figure 1.10 Types of crack initiation points observed in low alloy steels. **(a)** Decohesion between the matrix/particle interfaces and **(b)** fracture of a brittle particle[53].

1.3.1 Brittle fracture behaviour

Metals with a body-centred cubic (BCC) lattice such as low alloy steel or hexagonal lattice are subjected to the phenomenon of brittle fracture at low temperatures[42]. Metals with face-centred cubic (FCC) structure do not exhibit brittle fracture even when cooled down to temperatures close to absolute zero. Brittle fracture is characterized by very little deformation, macroscopically there is no evidence of deformation, but investigations involving X-ray diffraction reveals thin layers of deformed metal at the fracture surface[41]. The fracture starts at

micro-cracks in the metal matrix which usually is associated with a particle. Large stress concentration at the tip of the crack, due to little plastic deformation, will cause the crack to propagate normal to the tensile stress. This fracture mechanism is characterized as a cleavage fracture and is rapidly progressing through disruption of atomic bonds in tension[53]. The crack moves through the crystals along planes of low indices, i.e. high atomic density, which in (BCC) iron is along {100} planes[58]. This implies that the fracture surface is comparatively flat within one grain. Since adjacent grains have slightly different orientation, the fracture surface consist of many relatively flat facets, which gives the fracture surface a glittering appearance macroscopically, as shown in Figure 1.11(a).

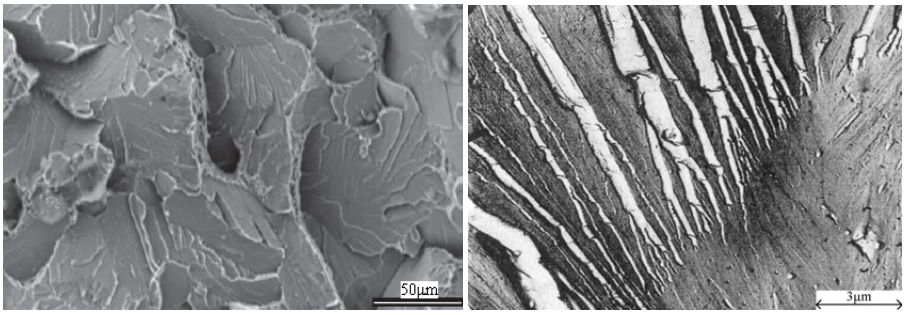

(a) **(b)**

Figure 1.11 Scanning electron image of brittle fracture in steel. **(a)** Cleavage fracture at -46 ˚C[59] and **(b)** appearance of characteristic river pattern in low carbon steel[53].

Within a single grain the cleavage crack can grow initially along a number of parallel planes, which may join further in the grain by the formation of steps[41]. The steps formed by the successive coalescence of cleavage cracks on parallel planes often display a typical pattern, referred to as river pattern, because of its resemblance of the tributaries of a river, see Figure 1.11(b)[53]. Because brittle fracture occurs without warning and usually produces disastrous consequences it should be avoided at all costs[41].

1.3.2 Ductile fracture behaviour

A non-homogeneous material such as low alloyed steel usually consists of a matrix having good plastic properties and with secondary phase particles such as inclusions embedded in the matrix. As already stated, the starting point of a fracture is usually at such particles. Thus, when the particles are stressed, voids form either by cracking of the particle, or by decohesion at the particle/matrix interface, as illustrated previously in Figure 1.10. In ductile fracture the formation of voids begins very early in tensile testing, as a result of the high stress imposed by dislocation pile ups on individual hard particles. These voids will elongate under the influence

of tensile stresses, but additionally a lateral stress is needed for them to grow sideways and link up with the adjacent voids[58]. Crack growth in ductile fracture essentially occurs by a process of void coalescence[45-48]. Figure 1.12(a) shows crack propagation by this process, where the voids are initially nucleated at small sulphide particles[58].

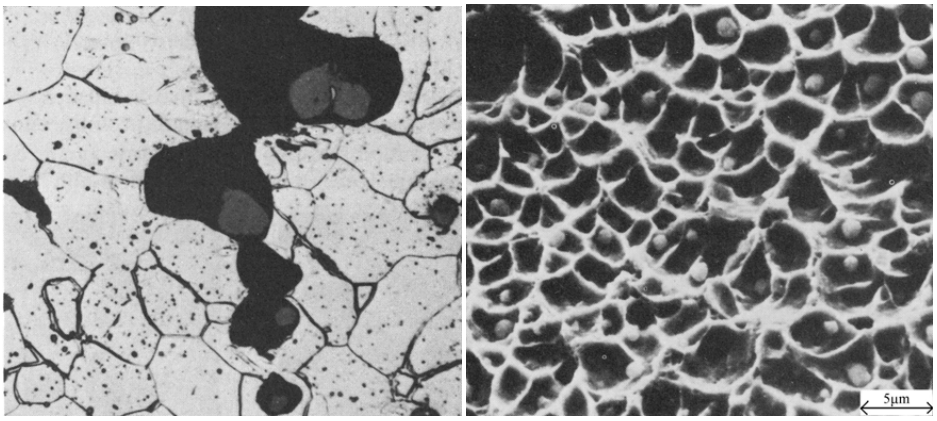

(a) **(b)**

Figure 1.12 Scanning electron micrographs of ductile fracture in low alloy steel, where voids are nucleated at inclusions. **(a)** Growth of a ductile crack by void coalescence and **(b)** fracture surface containing dimples with embedded particles[58].

This leads to the formation of a fracture surface consisting of "dimples", as if it had formed from numerous holes which were separated by thin walls until it fractures. At high magnification, using scanning electron microscope, small particles at the centre of these holes can be revealed, as shown in Figure 1.12(b). The voids appear first at large inclusions, then progressively at smaller and smaller particles[45]. As a result there is a good correlation between inclusion spacing and dimple size in SEM pictures of fracture surfaces[53].

1.3.3 Ductile to brittle transition

In the ductile-to-brittle transition temperature range of low alloyed steels, two fracture mechanisms are in competition; ductile fracture formation at high temperatures and transgranular cleavage formation at low temperatures. For nearly 100 years the Charpy impact test[57] has been used to determine the transition temperature of metallic materials. A standard Charpy V-notch impact test uses a 10 mm square cross section specimen with a 2 mm V-notch craved out at the centre of the specimen[56]. The specimen is broken in a three-point bending by a falling weight attached to a pendulum. The pendulums height, before and after breaking the specimen, determines the amount of energy the specimen absorbs[54,55]. Testing specimens at different temperatures and plotting the consumed energy versus temperature yields a Charpy energy curve from which the transition temperature ($T_{tr.}$) can be determined[59]. Figure 1.13

shows Charpy energy curves in the transverse direction of three hot rolled low alloy steels containing elongated manganese sulphides. The three steels included, referred to as A, B and C, contain varying volume percents of inclusions, ranging from 0.3%, 0.4% and 0.46%, respectively. It follows that the steel cleanliness has a large influence on the impact energy. In this case a high inclusion content results in both a reduction in the upper shelf energy and an increase in the transition temperature, as shown in Figure 1.13.

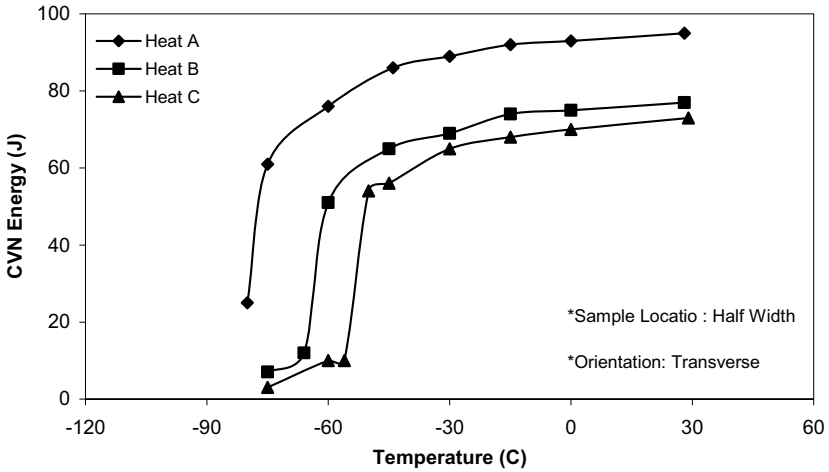

Figure 1.13 A plot showing variation of CVN impact energy (J) with temperature for transverse specimens of steels A, B and C, which contain 0.3%, 0.4% and 0.46% volume percent of inclusions, respectively[44].

A sketch illustrating the different effects inclusions can have on the Charpy energy curve is contained in Figure 1.14.

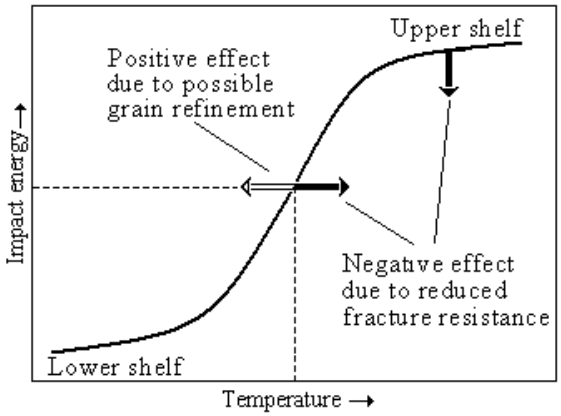

Figure 1.14 Schematic diagram illustrating how inclusions affect the CVN impact energy in steel.

It follows that inclusions will always have a negative effect on steel properties, unless they at the same time contribute to grain refinement.

1.4 Effects of non-metallic inclusions on the microstructure evolution in steels

In general, the mechanical properties of steel products depend on the prior microstructure evolution, i.e. the solidification and the solid state transformation behaviour. As stated earlier small grains have a beneficial effect on both the strength and ductility, and will therefore reduce the brittle to ductile transition temperature.

Non-metallic inclusions can influence the microstructure evolution in different ways. Some particles, that are stable in the liquid state, can act as potent sites for nucleation of delta ferrite crystals during solidification, which may contribute to the development of a fine equiaxed grain structure in the as-cast steel[20,21,23]. Others can retard grain growth by pinning the austenite grain boundaries[60,61]. Certain types of inclusions can also be active catalyst particles for the acicular ferrite formation in low carbon steel during the austenite (γ) to ferrite (α) transformation[18,62]. In the following, some of these points will be further elaborated and discussed in light of information given in recent literature.

1.4.1 Solidification behaviour

During solidification, the first solid phase start to form, which in low alloyed steel usually is delta ferrite. The driving force for solidification is the free energy changes ΔG between the solid and the liquid phase[63]. As the temperature of the melt drops below the melting point T_m, the free energy of the solid becomes lower than the free energy of the liquid. This creates the necessary

driving force for the solidification, as shown graphically in Figure 1.15, which applies to solidification of pure metals.

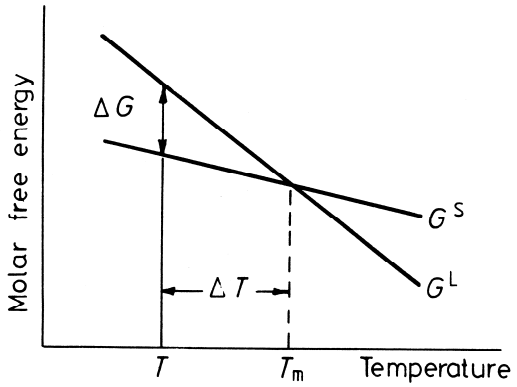

Figure 1.15 Schematic diagram showing how the molar free energy for the liquid and the solid changes close to the meting point for pure metals[63].

During epitaxial solidification, as observed in fusion welds, the transformation from solid to liquid state occurs spontaneous as soon as the liquidus temperature is reach. However, this is usually not the case in real castings since the formation of new surfaces give rise to a positive contribution to the free energy. Hence, a certain degree of undercooling ΔT is necessary to initiate the solidification[64]. The necessary undercooling depends strongly on the type of the heterogeneous nucleation sites available in the melt. If no such nucleation sites are present, the nucleation must occur by homogeneous nucleation, which is associated with large undercooling. That is rarely the case, since there always will be some contamination in the steel after the secondary refining processes. In contrast, heterogeneous nucleation requires much lower undercooling, since the formation of a new surface can occur on an already existing surface, such as the mould wall, inclusions or grain refining particles. These surfaces will assist the nucleation by reducing the interfacial energy between the embryo and the substrate, hence decreasing the positive contribution to the free energy associated with the creation of a new surface. In general, the effectiveness of individual particles to act as heterogeneous nucleation sites can be evaluated from a balance of interfacial energies[65]. In an ideal case, this can be illustrated by means of the spherical cap model by considering the wetting angel β and the radius of curvature r_s, as shown schematically in Figure 1.16.

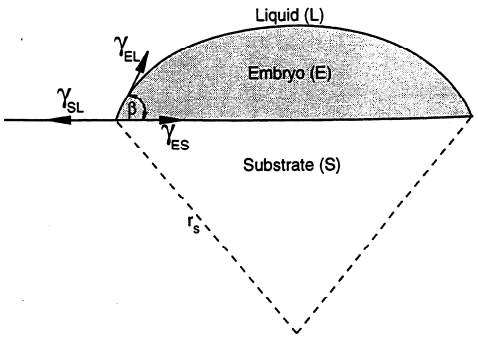

Figure 1.16 Schematic diagram defining the wetting angel β and the radius of curvature r_s of the embryo[29].

It follows from the definitions in Figure 1.16 that a complete wetting (i.e. epitaxial solidification) is achieved when the wetting angel β is zero. If the wetting angle between the solidifying metal and the substrate particle is low, the corresponding undercooling necessary to trigger nucleation is low.

In addition to the interfacial energy balance, the size of the heterogeneous nucleation site is also importance, as illustrated in Figure 1.17.

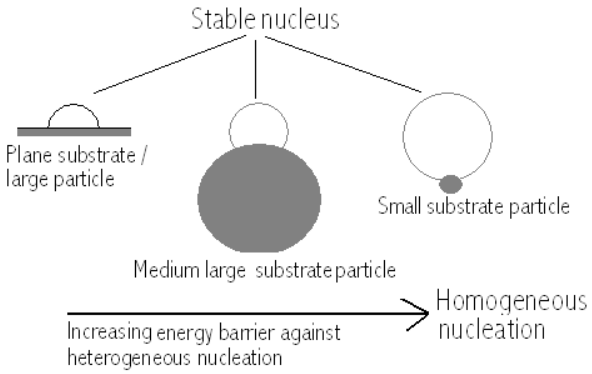

Figure 1.17 Schematic diagram illustrating the effect of particles size on the energy barrier against heterogeneous nucleation.

It follows from Figure 1.17 that the necessary undercooling increases when the size of the substrate decreases. Hence, the energy barrier against heterogeneous nucleation increases, and will in the limiting case approach that of homogeneous nucleation.

In a real casting situation the flat mould wall will be a preferred nucleation site, from which large columnar grains will evolve by a process of competitive growth[66], as shown in Figure 1.18.

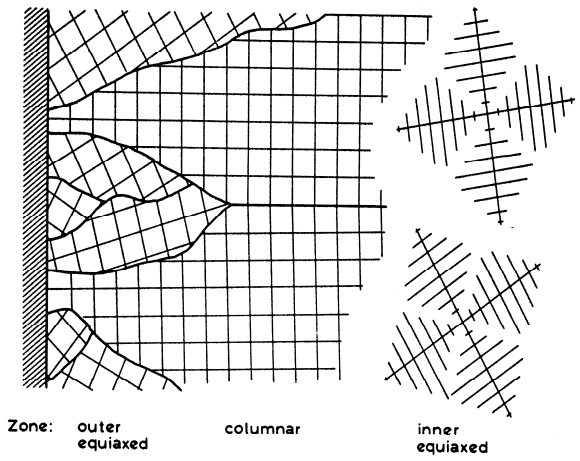

Figure 1.18 Schematic diagram illustrating the formation of columnar and equiaxed grains during solidification[66].

Since there is a compositional difference between the solidifying columnar grains and the melt, as determined by the difference between the solidus and the liquidus line in the phase diagram, a solute-rich boundary layer will build up in front of the advancing solid/liquid interface due to limited diffusion in the melt. In Figure 1.19 the equilibrium liquidus temperature is plotted as a function of distance *x'* from the interface.

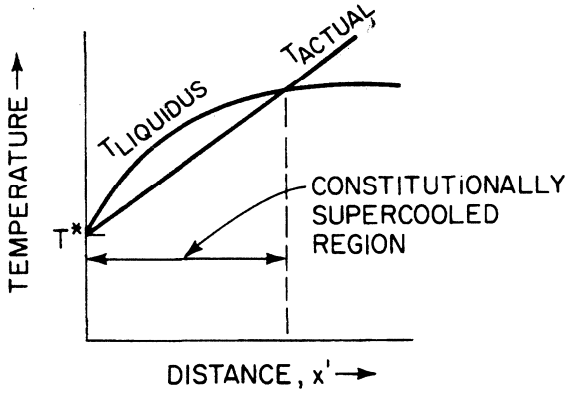

Figure 1.19 Illustration of the actual temperature T_{actual} in the melt and the equilibrium liquidus temperature $T_{liquidus}$ at some distance x' from the solid/liquid interface[64].

The equilibrium liquidus temperature increases with distance from the interface because a low solute content implies a higher liquidus temperature. In Figure 1.19, the actual temperature gradient in the melt is superimposed on the same diagram. It can be seen that the actual temperature T_{actual} in the liquid at the interface is below its equilibrium liquidus temperature $T_{liquidus}$. Therefore, the liquid at the interface will be undercooled, and this is referred to as constitutional undercooling. The term constitutional indicates that the undercooling arises from a change in composition and not in temperature. If potent substrate particles are present ahead of the advancing interface, equiaxed grains may nucleate and grow from these sites, as shown in Figure 1.18. Under certain conditions they may completely override the columnar grain formation.

In Figure 1.20, different types of non-metallic inclusions in steel are ranked in terms of their ability to nucleate delta ferrite during solidification. It follows from this plot that the undercooling is closely related to planar lattice disregistry, which, in turn, can be regarded as a measure of the embryo/substrate interfacial energy γ_{ES} defined previously in Figure 1.16. Since the degree of undercooling associated with constitutional undercooling is small, typically less than one degree Celsius, only specific inclusions such as CeS, CaS, Re_2O_3 and TiN have the ability to act as potent nucleation sites for delta ferrite during solidification of low alloy steels.

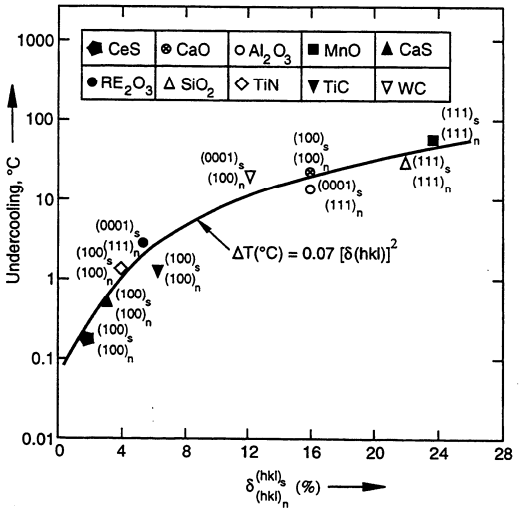

Figure 1.20 Relationship between undercooling and the planar lattice disregistry between the nucleas (i.e. delta ferrite) and the substrate for different nucleating particles in low alloy steels[15].

1.4.2 Solid state transformation behaviour

Normally, when steel sheets and beams are joined together, the weld must exhibit at least similar properties as the base steel. This is possible because of acicular ferrite formation during fusion welding of low alloy steel. Acicular ferrite is an intragranular form of ferrite, which can greatly improve the properties of welds. Acicular ferrite usually forms naturally in welds as a consequence of the rapid cooling and the presence of a fine distribution of non-metallic inclusions. Although the importance of acicular ferrite has been recognized since the seventies, the nature of the microstructure component is still being debated. But its good characteristics have been the origin of several attempts to develop steel products that exhibit similar microstructure.

1.4.2.1 Conditions for acicular ferrite formation

Historically, almost all knowledge involving the nature of acicular ferrite comes from weld metals. The reason for this is that acicular ferrite forms intragranularly on nucleating particles during the γ to α transformation in the displacive transformation temperature region. Since welding is associated with high cooling rate and entrapment of deoxidation particles, acicular ferrite may easily form in welds. It is the interaction of the liquid weld metal with its surrounding gasses, together with the use of strong deoxidising elements such as silicon, aluminium and titanium, and protective slag forming compounds which causes the entrapment

of complex multiphase non-metallic inclusions in the solid at the advancing δ-ferrite/liquid interface. Although most of the theory and schematic diagrams describing acicular ferrite formation are based on weld metals, they are also applicable for casting of steel under similar conditions. The term acicular means shaped like a pointed needle, but it is generally recognised that acicular ferrite has in three-dimensions the morphology of thin, lenticular plates. The shape of acicular ferrite is sometimes stated to be rod-like, but in a two-dimensional section, as shown in Figure 1.21, the acicular ferrite appears like plates rather than rods.

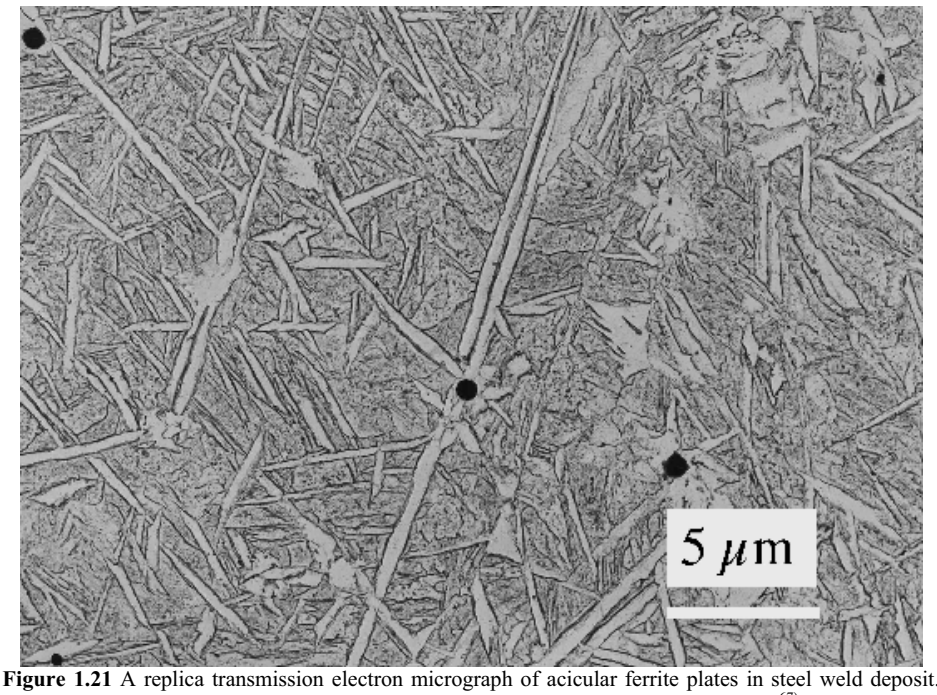

Figure 1.21 A replica transmission electron micrograph of acicular ferrite plates in steel weld deposit. Shown are plates of ferrite pointing in different directions along crystallographic planes[67].

An acicular ferrite microstructure is usually assumed to be good for achieving high cleavage toughness. This is because the plates of ferrite points in many different directions, and hence are able to frequently deflect cracks[67]. This should give better toughness when compared with allotriomorphic ferrite, or even Widmanstätten ferrite or bainite.

Traditionally, low alloy steel products are clean, as described previously in Section 1.2, and exhibit a good combination of strength and toughness, where fine allotriomorphic ferrite forms on the boundaries of small austenite grains during the γ to α transformation. In cases where the steel contains a fine distribution of potent nucleating particles, the ferrite may shift from being

grain boundary nucleated to being intragranularly nucleated[25,75-77]. In Figure 1.22, this is schematically illustrated in a continuous cooling transformation (CCT) diagram in the context of the overall microstructure evolution during cooling from the liquid state to room temperature (RT).

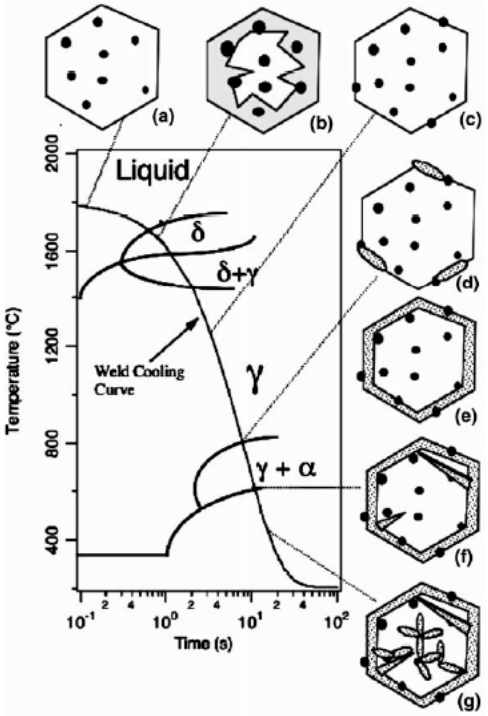

Figure 1.22 Schematic illustration of a weld cooling curve in a hypothetical CCT-diagram, which shows different phase transformations that may occur during cooling from the liquid state to room temperature[78].

According to Figure 1.22, the sequence of reactions that occurs during cooling of a steel weld can be summarised as follows[78]: (a) In the temperature range between 2000 to 1700 ˚C the dissolved oxygen and the added deoxidation elements during welding start to react to form complex oxide particles. Another possibility, as will be discussed later, could be to add a master alloy, containing these particles to the liquid steel, just before casting. (b) As the cooling path is entering the delta ferrite region the liquid starts to solidify, which is discussed extensively in the previous section. The particles are now entrapped in the austenite matrix (c), and grain growth may occur during cooling from 1500 to 800 ˚C. The growth may be retarded by the same particles according to the restraining force from pinning particles. When the temperature reaches about 800 ˚C the γ to α transformation starts at the grain boundaries (d). This is mainly

because the grain boundaries can easier than the inclusions adopt an orientation relationship with the ferrite. As the ferrite transformation progresses at the prior austenite grain boundaries (e), ferrite sideplates will start to appear and grow into the grain interior (f). This occurs in a temperature range where the reconstructive transformation, which is controlled of diffusion, becomes slow, which gives way for displacive reactions such as bainite and martensite. At some point in this temperature range there is sufficient undercooling to overcome the barrier against intragranular nucleation of ferrite. Acicular ferrite will then start to grow from inclusions, as shown in Figure 1.22(g).

Earlier, acicular ferrite was thought to be a single transformation product. Some suggested it was intragranularly nucleated Widmanstätten ferrite[68)], while others again called it intragranularly nucleated bainite[79)]. According to Thewlis *et al.*[80,81)] acicular ferrite can consist of both types of intragranular transformation products. Thus the individual fractions formed of these two constituents depend on the particle size and the amount of alloying elements in the weld.

The development of acicular ferrite microstructure is complex and involves both grain boundaries and intragranular transformations, and the amount of acicular ferrite formed depends on several factors. First of all, large inclusions are expected to be more effective in nucleating acicular ferrite since the curvature of the inclusion/nucleus interface then will be reduced, analogues to that schematically illustrated in Figure 1.17 for solidification. It is also important to bear in mind that large inclusions can easier nucleate voids during ductile fracture development, or cleavage cracks, during brittle fracture development. Secondly, the number of available nucleation points is important. If the aim is to increase the amount of acicular ferrite, the nucleation has to be shifted from the grain boundaries to the inclusions, as schematically illustrated in Figure 1.23.

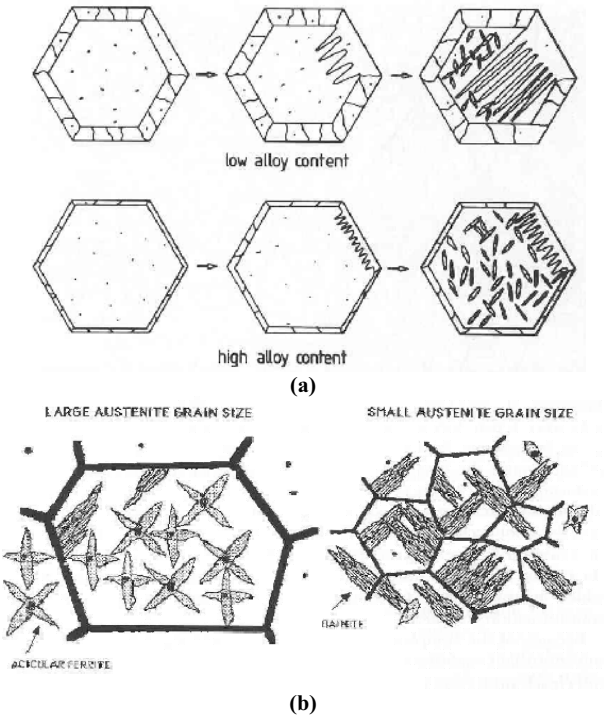

Figure 1.23 Schematic diagram illustrating the effect of austenite grain size and alloy content on the nucleation of acicular ferrite. **(a)** An increase in alloy content will increase the intragranular nucleation of ferrite and **(b)** a large grain size implies a small grain boundary surface area available for nucleation and hence acicular ferrite will dominate[67].

It follows that acicular ferrite development can be regarded as competition between nucleation and growth of ferrite at austenite grain boundaries and ferrite at inclusions. In Figure 1.23(a) the γ to α transformation is illustrated in terms of low and high alloy content. It is shown that a high alloy content will increase the amount of acicular ferrite. The same is also true if the austenite grain size increases, as shown in Figure 1.23(b). Then there will be fewer nucleation points for ferrite sideplates, which is favourable for the acicular ferrite formation. In three dimensions, the variation in surface area of austenite grain boundaries with respect to the grain size will be as shown in Figure 1.24.

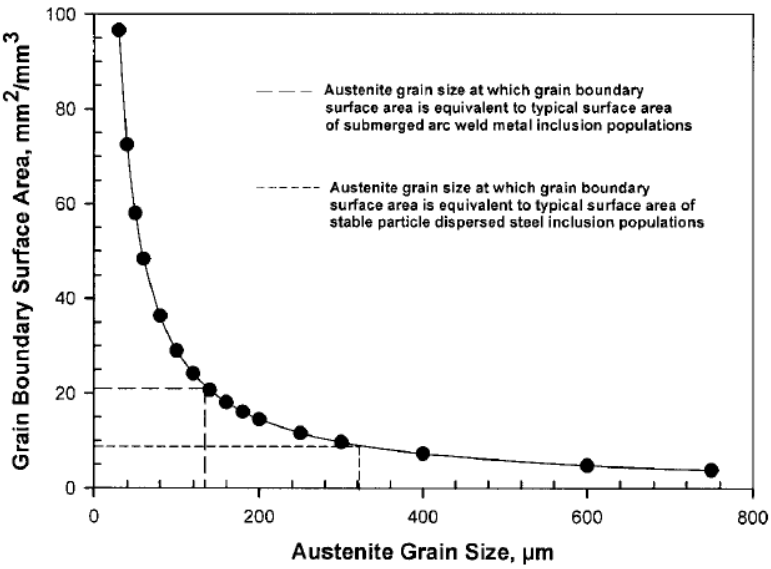

Figure 1.24 A graph showing the variation in austenite grain boundary surface area with respect to the grain size. Typical values for when the overall austenite grain boundary surface area are equivalent to typical surface area of stable particles for particle dispersed steels and submerged arc weld metals are superimposed on the graph[69].

Figure 1.24 shows that there is a sharp decrease in the grain boundary surface area when the grain size drops from 200 to 100 µm and vice versa, meaning that a small increase in grain size may result in a relatively large decrease in grain boundary nucleated ferrite. In Figure 1.24, typical values for when the overall austenite grain boundary surface area are equivalent to typical surface area of stable particles for particle dispersed steels and submerged arc weld metals, respectively, are superimposed on the graph[69]. In the coarse grain heat affected zone (CGHAZ), for a particle dispersed steel, the grain size is normally between 100 and 200 µm. Comparing with Figure 1.24, this grain size is substantially lower then the equivalent austenite grain boundary surface area needed to suppress the formation of allotriomorphic ferrite, which indicates that intragranular ferrite nucleation may be kinetically difficult to achieve. A greater density of particles may therefore be required to shift the balance. However, in this analysis the particles are considered as inert substrates, where only the size, number and shape of the particles controls the intragranular ferrite nucleation. Since it is well know that there are inclusions that are more efficient in nucleating acicular ferrite than others, the equivalent austenite grain size value may be somewhat lower for different types of inclusions.

Because of the complex nature of the inclusions, and the difficulties involved in conducting controlled experiments with welds, the factors controlling the nucleation potency of inclusions

are not clearly understood. Still four types of mechanisms have been proposed to explain intragranular ferrite nucleation, and these are schematically illustrated in Figure 1.25.

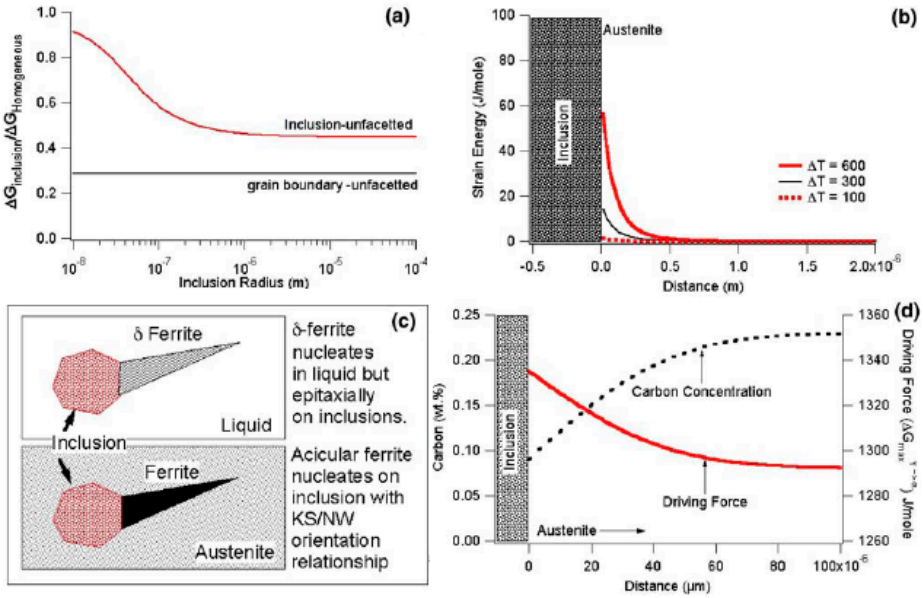

Figure 1.25 Schematic illustration of different mechanisms for nucleation of acicular ferrite on inclusions. **(a)** Inclusions surface acts as an inert surface for nucleation and therefore large inclusions are potent sites, **(b)** strain energy near the inclusion may increase due to difference in thermal expansion between austenite and inclusion, which might reduce the activation energy for nucleation, **(c)** matching between ferrite and inclusion lattice will decrease the interfacial energy between inclusion and ferrite in comparison to incoherent inclusion–austenite interface and **(d)** local depletion of hardening elements such as carbon and/or manganese which might lead to an increase in driving force for nucleation of ferrite from austenite[78].

The first mechanism, Figure 1.25(a), suggests that inclusions, as mentioned above, are inert substrates. The calculations show that the ratio of the activation energy for nucleation on inclusions to that for homogeneous nucleation decreases with an increasing inclusion diameter. The second theory, Figure 1.25(b), proposes that the nucleation is controlled by the presence of localised stresses between the austenite matrix and the inclusion, as a result of a difference in thermal contraction. Both these two mechanisms have been reviewed by Jones[70] and found insufficient to adequately explain the relative nucleation potency of inclusions. The most popular idea is the third mechanism, Figure 1.25(c), which suggests that those inclusions showing the best lattice matching with ferrite are most effective in nucleating the ferrite. The lattice matching can be expressed in terms of a planar misfit between the substrate and the embryo, where the ferrite nucleates epitaxially on a low index plane of a faceted inclusion. Mills

et al.[71] have calculated the misfit in percent between different substrates and ferrite, as shown in Table 1.1.

Table 1.1 Misfit values between different substrates and ferrite[71].

Inclusion	Orientation	Plane of Epitaxy	Misfit %
TiO	Bain	{100}	3.0
TiN	Bain	{100}	4.6
γ-alumina	Bain	{100}	3.2
Galaxite	Bain	{100}	1.8
CuS	Cube	{111}	2.8

The lattice matching concept stems originally from grain refining of aluminium, which involves solidification and not solid state transformation. The extrapolation of the concept to the γ to α transformation may not be totally justified. However, experiments have confirmed that there is an orientation relationship between γ-alumina, Galaxite and TiN with acicular ferrite in low alloy steel, which falls within the Bain orientation region[72], as indicated in Table 1.1. The bain orientation relationship is a typical orientation relationship between a face-centred cubic structure and a body-centred cubic structure. It has also been reported that there is an orientation relationship between acicular ferrite and the austenite it grows in, which also falls within the Bain orientation region[73]. This indicates that the acicular ferrite needs to bear an orientation relationship within the Bain region with both the substrate and the austenite in order to be efficiently nucleated. Since the nucleating particles form in the liquid state, and thus have been randomly entrapped in the austenite matrix, this requirement seems difficult. Nevertheless, statistical calculations have shown that at least 12% of the inclusions purely by chance can have this orientation relationship[72], which would be a satisfactory amount of nucleating particles for promoting a fine interlocking grain structure. These calculations are also based on the fact that the nucleating particle usually consists of several phases, which increase the probability of having a lattice coherency with both the ferrite and the austenite. The last mechanism describing the intragranular ferrite nucleation is given in Figure 1.25(d). It shows local depletion of elements such as carbon, manganese and silicon in the austenite in the vicinity of an inclusion, due to solid state formation of specific phases (e.g. MnS) at the inclusions surface. This depletion may lead to a local increase in the driving force for the nucleation of ferrite from austenite at the inclusion surface. Measurements have shown evidence of a manganese depleted zone around inclusions[74,82], which makes the proposed mechanism plausible.

1.4.2.2 Acicular ferrite formation in Ti deoxidized steels

In the previous chapters the importance of the steel cleanliness has been emphasised. Nevertheless, indigenous particles can have a beneficial effect on steel properties by promoting the development of a fine interlocking grain structure in weld deposits, as discussed in the previous chapter. Recently, the transfer of this technology to wrought steels has been attempted, by deoxidising low alloy steels with Ti (120-140 ppm) at low Al levels (<30 ppm)[25,75-77,82-85]. In general, the possibility of forming different non-metallic inclusions with the potential of nucleating acicular ferrite is found to be good for Ti deoxidised steels. This is also in accordance with Table 1.1, which shows that TiO and TiN have a low crystallographic misfit with respect to ferrite, and may thus epitaxially nucleate ferrite. There is strong circumstantial evidence that the effectiveness of particles for intragranular nucleation is markedly improved as the titanium content increases. However, the question about the potency of these inclusions still remains controversial. This is partly because non-metallic inclusions found in commercial steels usually consist of a mixture of several crystalline and/or amorphous phases so that identification of the specific phase responsible for the nucleation becomes difficult. A schematic illustration of a multi-phase particle commonly found in a Ti deoxidised steel is shown in Figure 1.26.

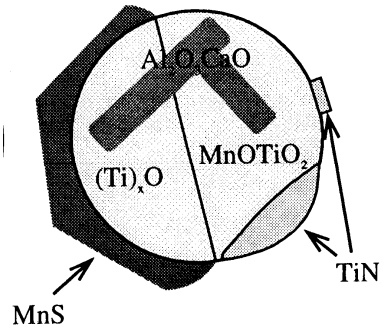

Figure 1.26 Schematic illustration of a multi-component particle found in a Ti deoxidised steel[85].

The particle in Figure 1.26 consists of five constituents; Al_2O_3, $MnOTiO_2$, $(Ti)_xO$, TiN and MnS, which probably form sequentially before, during and after the solidification. In this case it is difficult to point out the actual nucleation mechanisms, although the formation of MnS at the surface leads to a Mn-depleted zone in the surrounding matrix. This corresponds to one of the four nucleation mechanisms referred in Figure 1.25.

Although the Ti-containing inclusions exhibit a high ability to nucleate acicular ferrite, they do not efficiently grain refine low alloyed wrought steels. This is because wrought steels usually

obtain a good combination of strength and toughness through process techniques that require a fine austenite grain structure prior to the γ to α transformation. This makes intragranular nucleation difficult because of the large grain boundary surface area of austenite compared to the relatively low number density of the Ti particles (typically $<<10^6$ particles per mm^3)[15]. Still a fine distribution of Ti particles can improve the weldability, particularly with respect to the heat affected zone (HAZ) toughness. During welding, austenite grain growth will occur close to the fusion boundary due to local heating, which results in the formation of a coarse grain heat affected zone (CGHAZ) close to the weld pool, as shown schematically in Figure 1.27(a) and 1.27(b).

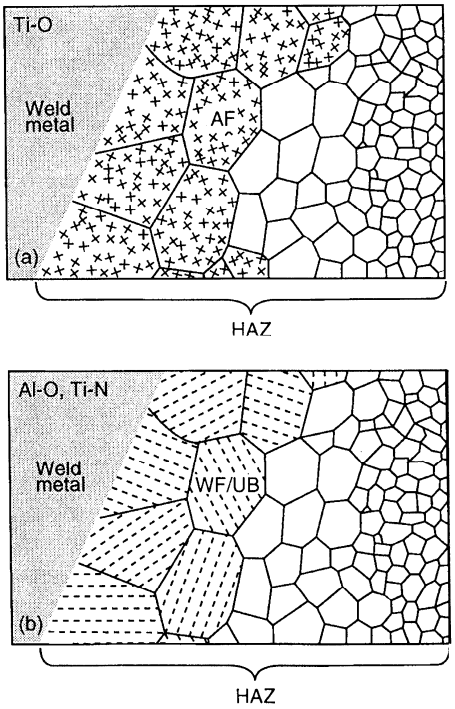

Figure 1.27 Schematic illustration of the transformation behaviour in the coarse grain heat affected zone (CGHAZ) during high heat input welding. **(a)** Formation of acicular ferrite in the CGHAZ of a Ti deoxidised steel and **(b)** formation of Widemanstätten ferrite and upper bainite in the CGHAZ of a conventional Al-Ti microalloyed steel[15].

According to Figure 1.27(b), Widmanstätten ferrite and upper bainite form in CGHAZ, which are the common microstructural constituents observed in traditional Al deoxidised steels[86]. In a

Ti deoxidized steel this formation will be suppressed, and instead acicular ferrite is promoted, as schematically illustrated in Figure 1.27(a).

1.4.2.3 Acicular ferrite formation in CeS dispersed steels

For many years it has been a desire to find alternative methods for grain refinement of steels, where the austenite grains by nature are coarse, e.g. air cooled forging steels and CGHAZ in weldments. As shown in the previous section, Ti oxides play such a role in the CGHAZ. Another inclusion type that is capable of nucleating acicular ferrite is cerium sulphide. Cerium combines with sulphur in the liquid state and forms CeS, which exhibits a good lattice coherency with respect to ferrite. It is known that very effective nucleants can oppose the austenite grain boundary transformation at relative fine austenite grain size. The lattice parameter of the cubic cerium sulphide cell is 5.778 Å, which approximately equals the size of two cubic cells of ferrite. This makes CeS an efficient nucleant for acicular ferrite in steels, according to the misfit theory. Still, the use of cerium sulphide as a grain refining component in steels is relatively unknown.

In the recent work of Thewlis[87], the efficiency of cerium sulphide particles in promoting fine acicular ferrite formation has been investigated. Several casting experiments were carried out, where different amounts of cerium (0.04-0.18%) and sulphur (0.01-0.04%) were added to a 50 kg batch of clean molten steel. The sulphur was added just before casting to minimize the time available for growth, coarsening and removal of the inclusions, while the oxygen was kept as low as possible to avoid cerium oxide formation. The study shows that the sulphide dispersed steels produced contained sulphur levels up to 350 ppm. Compared to submerged arc steel weld metals, which typically contain 300-400 ppm of oxygen, the sulphide dispersed steels display the same volume fraction of dispersed particles. Still the nucleating potency with respect to acicular ferrite is expected to be greater in submerged arc welds because of the finer particle size. In the CeS dispersed steels the inclusions number densities were of the order of 0.7 to 6.1×10^6 mm^{-3}, with mean diameters ranging between 0.63 and 1.70 μm[87]. This is sufficient to promote acicular ferrite formation during the γ to α transformation. In addition, the microstructure contained various amounts of primary ferrite and ferrite sideplates, depending on the base metal chemical composition and cerium sulphide particle dispersion. Figure 1.28 shows typical acicular ferrite formation in one of the castings, where also some primary ferrite can be seen in the vicinity of the prior austenite grain boundaries.

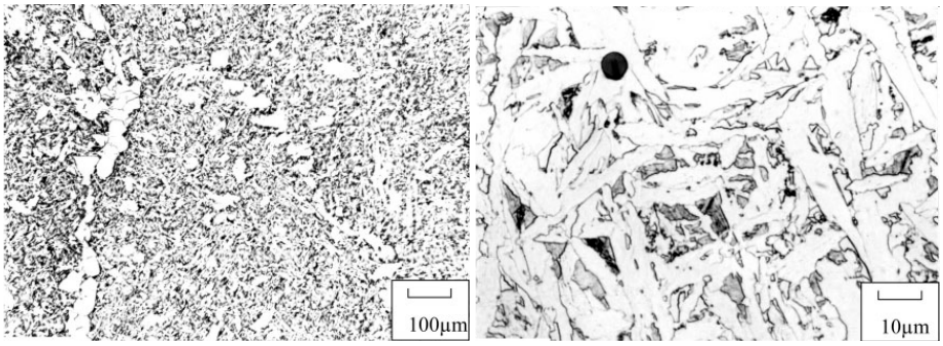

(a) **(b)**

Figure 1.28 Microstructure at base of the billet. **(a)** Fine distribution of acicular ferrite with primary ferrite on prior austenite grain boundaries and **(b)** nucleation of acicular ferrite on cerium sulphide particles[87].

Another set of casting experiments were simultaneously carried out by Thewlis[87]. In this case 3-4 ton billets of the same base steel material as in the 50 kg vacuum melts were cast containing the additions of cerium and sulphur. In Figure 1.29 the resulting inclusion number densities per unit volume and mean particle sizes in different regions of the billet are compared with the corresponding numbers for the 50 kg vacuum melts.

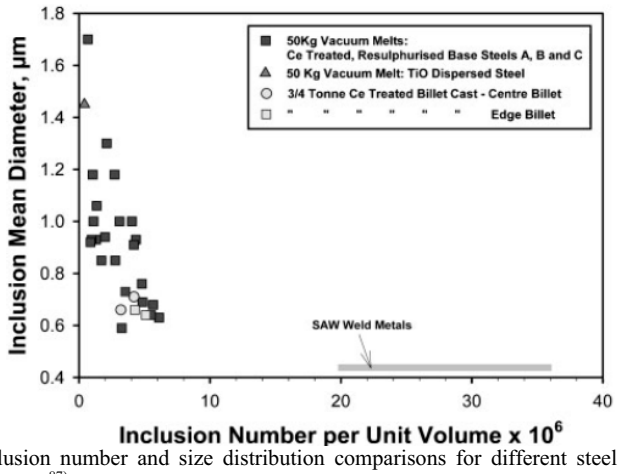

Figure 1.29 Inclusion number and size distribution comparisons for different steel castings trails, as reported to by Thewlis[87].

Figure 1.29 also contains data for steel weld metals. It is evident that the inclusion volume fraction and size distribution of the billets are comparable with the 50 kg vacuum melts. However, they are not as good as the submerged arc weld (SAW) materials. Nevertheless, fine

acicular ferrite could readily be observed at the edge of the cast strand where the cooling rate had been fastest.

1.5 Manufacturing and use of grain refiners for steels

It follows from the previous discussion, that relatively large batches of low alloy steels can be grain refined using cerium sulphide particles. These experiments also show that the required particle size distribution for promoting acicular ferrite is obtainable in industrial steelmaking, but to achieve a uniform particle distribution throughout the billet is difficult. Much of the problem lies in that the particles must be created within the system as result of desulphurisation reactions, which makes it difficult to transfer the technology to continuous casting of steel.

As shown in Figure 1.30, the key issue in steel grain refinement is to control the size distribution of the nucleating inclusions, which in the ideal case should both be fine and narrow. In the following, these are referred to as dispersoids to better distinguish between harmful and useful inclusions.

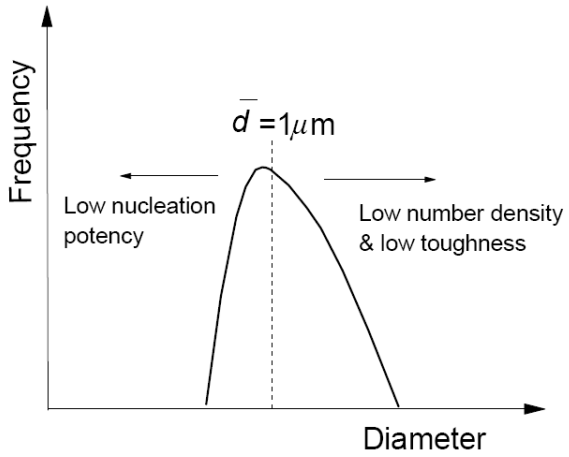

Figure 1.30 Schematic diagram illustrating how the grain refining conditions can be optimised through strict control of the size distribution of the nucleating dispersoids in the steel[31].

Note that the mean value of 1 μm used to characterize the optimum dispersoids size distribution in Figure 1.30 represents a reasonable compromise between two conflicting requirements. On the one hand, a submicron particle size implies that the particles start to lose their potency because a curved interface increases the associated energy barrier against nucleation[15,88,89]. On the other hand, it the particle size is significantly larger than 1 μm the particles may become

detrimental to toughness[15,18,90]. At the same time the particle number density drops rapidly, which makes grain nucleation at such sites less likely.

To achieve this optimum size distribution of particles during conventional steelmaking involving continuous casting is difficult. However, one possibility is to make use of a specially designed grain refiner (referred to as master alloys), analogues to what is done in grain refining of aluminium alloys[30]. A requirement is that the master alloy contains the right volume fraction and number density of particles capable of promoting grain refinement. The master alloy should also be added late in the steelmaking process and in such quantities that it does not affect the steelmaking process itself. Thus, it must contain a relatively high amount of sulphur or oxygen.

Based on simple stoichiometric and stereological relationships it is possible to estimate the minimum amount of oxygen or sulphur needed to obtain a specific target number density of inclusions in the steel. This is done in Figure 1.31 for a limited range in the particle size.

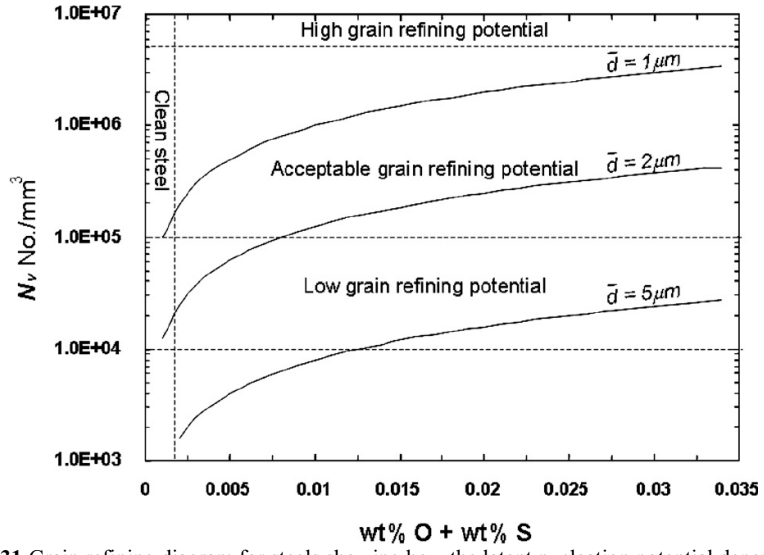

Figure 1.31 Grain refining diagram for steels showing how the latent nucleation potential depends on the number density of oxides and sulphides in the parent material[31].

In Figure 1.31 typical limits for the particle number densities in steel welds metals[15,79] and Ti deoxidised steels[15,83-85] are superimposed. These define the ranges for the high and the acceptable grain refining potentials in the diagram. As expected, the number density is seen to be extremely sensitive to variations in the mean size of the dispersoids. A closer inspection of

the diagram reveals that an acceptable grain nucleation potential requires a very high content of oxygen or sulphur in the steel (0.02 wt% or higher). This is equivalent to the amount of sulphur which needs to be added to the steel melt if a conventional clean steel is to be grain refined by a late addition of a tailor made master alloy. In addition to high sulphur content, the master alloy must also yield a mean particle size in the vicinity of 1 μm to ensure an acceptable grain refining potential, as shown previously in Figure 1.31.

Another important aspect is the limited amount of alloy addition which can be made to liquid steel late in the process without interfering with the steelmaking process itself. In industrial steelmaking a sensible level of addition is between 0.2 and 0.5 percent by weight[31]. It follows from the diagram in Figure 1.32 that this requires the use of highly concentrated master alloys with, oxygen or sulphur contents close to 10 wt%.

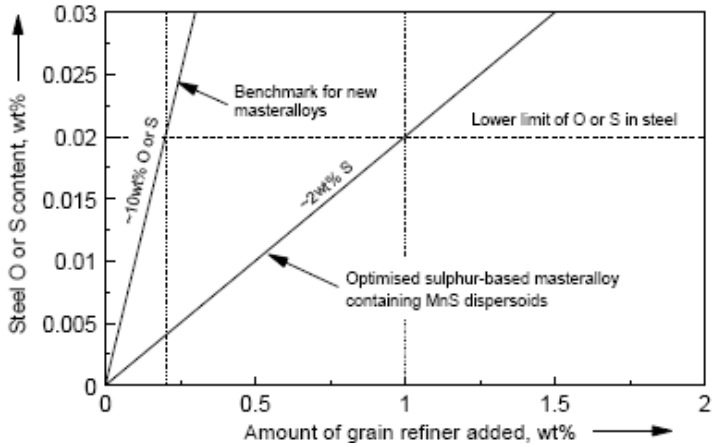

Figure 1.32 Diagram showing the potential of developing new master alloys with improved efficiency for grain refinement of continuously cast steels. In this case the level of addition should be kept as low as possible, and the ultimate goal is 0.2% by weight[31].

However, such grain refiners, where the dispersoids occupy about 50% of the volume, can only be produced through smart alloy design in combination with novel manufacturing methods, as illustrated in Figure 1.33.

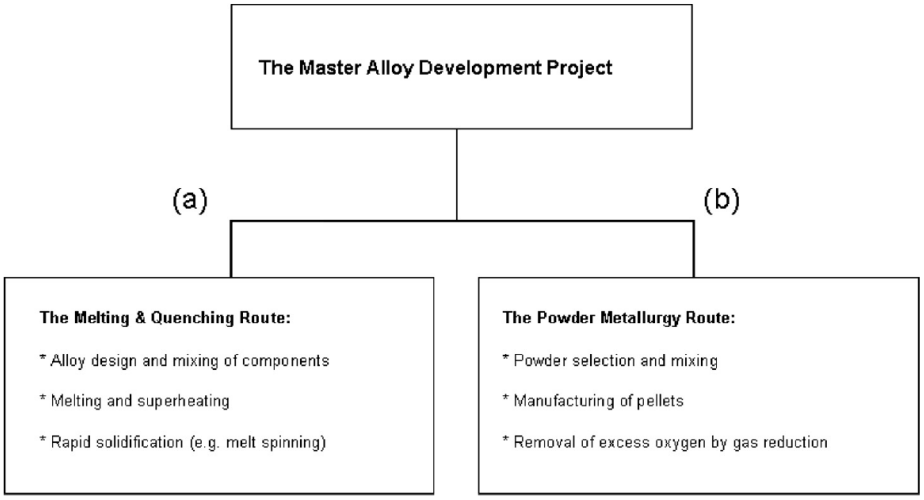

Figure 1.33 Overview of the different methods used to produce the grain refining master alloys. **(a)** The Melting & Quenching Route and **(b)** The Powder Metallurgy Route[31].

Referring to Figure 1.33, the melting & quenching route means that the alloy components first are mixed and melted in an induction furnace under the shield of a protective gas and then superheated to make sure that all elements, including oxygen and sulphur, are in solution. This superheated melt is then rapidly quenched to achieve the desired distribution of the dispersoids in the grain refiner, by means of melt spinning or gas atomization. Alternatively, a powder metallurgy route can be employed. The value-added DRI (Direct Reduced Iron) method involves mixing of iron oxide powder (optionally iron powder) with other metals or oxides. The pellets made from these blends are subsequently reduced in a controlled atmosphere at high temperatures to remove excess oxygen from the master alloy, leaving behind a fine dispersion of stable oxides in the iron matrix.

The development of such novel grain refiner for steel will be a key issue in future research at NTNU/SINTEF, and the ultimate goal of the presented PhD project.

1.6 References

(1) *World Steel in Figures, International Iron and Steel Institute*, (2009), ISSN: 1379-9746.

(2) J. -P. Birat: *Ironmaking Steelmaking*, **28**(1999). 152.

(3) H. V. Atkinson and G. Shi: *Progress in Mater. Science*, **48**(2003), 457.

(4) L. Zhang and B. G. Thomas: *ISIJ Int.*, **43**(2003), 271.

(5) W. C Leslie: The Physical Metallurgy of Steels, McGraw-Hill, New York, (1981).

(6) M. Fernandes, N. Cheung and A. Garcia: *Materials Characterization*, **48**(2002), 255.

(7) A. W. Cramb: *Scandinavian Journal of Metallurgy*, **26**(1997), 2.

(8) E. T. TurkDogan: Fundamentals of Steelmaking, The Institute of Materials, London, (1996).

(9) K. W. Lange: *Int. Mat. Rev.*, **33**(1988), 53.

(10) K. Uemura, M. Takahashi, S. Koyama and M. Nitta: *ISIJ Int.*, **32**(1992), 150.

(11) S. Taniguchi and J. K. Brimacombe: *ISIJ Int.*, **34**(1994), 722.

(12) R. Kiessling: *Encyclopedia of Materials: Science and Technology*, (2003), 6278.

(13) T. Skaland, Ø. Grong and T. Grong: *Metall. Mater. Trans. A*, **24A**(1993), 2321.

(14) T. Skaland, Ø. Grong and T. Grong: *Metall. Mater. Trans. A*, **24A**(1993), 2347.

(15) Ø. Grong: Metallurgical Modelling of Welding-2nd Ed., The Institute of Materials, London, (1997).

(16) A. R. Mills, G. Thewlis and J. A. Whiteman: *Mater. Sci. Technol.*, **3**(1987), 1051.

(17) S. S. Babu, S. A. David, J. M. Vitek, K. Mundra and T. Debroy: *Mater. Sci. Technol.*, **11**(1995), 186.

(18) Ø. Grong and D. K. Matlock: *Int. Met. Rev.*, **31**(1986), 27.

(19) B. Q. Han and S. Yue: *Journal of Materials Processing Technology*, **136**(2003), 100.

(20) Y. Nuri, T. Ohashi, T. Hiromoto and K. Kitamura: *Trans. ISIJ*, **22**(1982), 399.

(21) W. G. Wilson, L. J. Heaslip and I. D. Sommerville: *JOM*, **39**(1985), 36.

(22) R. W. K. Honeycombe and H. K. D. H. Bhadeshia: Steels-Microstructure and Properties, Edward Arnold, London, (1995).

(23) B. L. Bramfitt: *Metall. Trans.*, **1**(1970), 1987.

(24) J. H. Shim, Y. J. Oh, J. Y. Suh, Y. W. Cho, J. D. Shim, J. S. Byun and D. N. Lee: *Acta Mater.*, **49**(2001), 2115.

(25) F. Ishikawa, T. Takahashi and T. Ochi: *Metall. Mater. Trans. A*, **25A**(1994), 929.

(26) F. Ishikawa and T. Takahashi: *ISIJ int.*, **25**(1995), 1128.

(27) J. M. Gregg and H. K. D. H. Bhadeshia: *Acta Mater.*, **45**(1997), 739.

(28) I. Madariaga, J. L. Romero and I. Gutierrez: *Metall. Mater. Trans. A*, **29A**(1998), 1003.

(29) Ø. Grong, T. Grong and T. Skaland: Proc. 7th Inter. Ferroalloys Congress (INFACON 9), The Norwegian Ferroalloys research Organisation, Trondheim, Norway, (1995), 697.

(30) Ø. Grong, P. Jönsson and O. -S. Klevan: Proc. 9th Inter. Ferroalloys Congress (INFACON 9), The Ferroalloys Association, Quebec, Canada, (2001), 562.

(31) Ø. Grong, L. Kolbeinsen, C. van der Eijk and G. Tranell: *ISIJ Int.*, **46**(2006), 824.

(32) S. Seetharaman – Ed, D. Sichen: Fundamentals of Metallurgy, Cambridge Boca Raton : Woodhead Pub. and Maney Pub. on behalf of the Institute of Materials, Minerals and Mining CRC Press, (2005), 370.

(33) T. Rosenqvist: Principles of Extractive Metallurgy, 2nd Ed., Tapir Academic Press, Trondheim, (2004).

(34) B. Deo and R. Boom: Fundamentals of Steelmaking Metallurgy, Prentice Hall International, New York, (1993).

(35) M. S. Millman and G. Thornton: *Revue de Métallurgie-CIT*, **95**(1998), 477.

(36) M. S. Millman: *Ironmaking Steelmaking*, **26**(1999), 169.

(37) S. K. Dutta and A. B. Lele: *Tool & Alloy Steels*, **321**(1998), 10.

(38) J. K. Cotchen, D. Tembergen and R. Teworte: *AISE Steel Technology*, **80**(2003), 40.

(39) M. R. Ozgu: *Canadian Metallurgical Quarterly*, **35**(1996), 199.

(40) D. Mazumdar and R. I. L. Guthrie: *ISIJ Int,*, **39**(1999), 524.

(41) G. E. Dieter, D. Bacon: Mechanical Metallurgy, McGraw-Hill, London, (1988).

(42) V. I. Trefilov: *Powder Metallurgy and Metal Ceramics*, **41**(2002), 548.

(43) J. R. Rice: *NATO ASI Series, Series E: Applied Sciences*, **130**(1987), 23.

(44) S. K. Paul and A. Ray: *Journal of Materials Engineering and Performance*, **6**(1997), 27.

(45) W. C. Leslie: *Transactions of the Iron & Steel Society of AIME*, **2**(1983), 1.

(46) P. F. Thomason: *Fatigue & Fracture of Engineering Materials & Structures*, **21**(1998), 1105.

(47) W. M. Garrison Jr. and N. R. Moody: *Journal of Physics and Chemistry of Solids*, **48**(1987), 1035.

(48) P. Neumann: *Materials Science and Engineering*, **25**(1976), 217.

(49) J. Pospiech: *Journal of Materials Engineering and Performance*, **41**(1995), 82.

(50) A. Griffith: *Philos. Trans. R . Soc*. London, **22A**(1920), 163.

(51) E. Orowan: Fatigue and Fracture of Metals, a Symposium held at the Massachusetts Institute of Technology, John Wiley & Sons Inc., New York, (1952).

(52) G. T. Hahn, W. S. Owen, B. L. Averbach and M. Cohen: *Welding Journal*, **38**(1959), 367.

(53) D. Broek: *International Metallurgical Reviews*, **19**(1974), 135.

(54) W. L. Server: *ESIS Publication*, **30**(2002), 205.
(55) D. Francois: *ESIS Publication*, **30**(2002), 21.
(56) N. L. Parr: *Engineer (London)*, **227**(1969), 487.
(57) G. Charpy: *Mémoires et Comptes Rendus de la Société des Ingénieurs Civilis de France*, (1901), 848.
(58) R. W. K. Honeycomb: Steels Microstructure and Properties, Edward Arnold (Publishers) Ltd., London, (1981).
(59) P. de T. V. Gomes, J. R. B. Cruz, E. G. Rabelo and M. M. Neto: *Materials Research*, **8**(2005), 57.
(60) L. P. Zhang, C. L. Davis and M. Strangwood: *Metall. Mater. Trans. A*, **30A**(1999), 2089.
(61) T. Koseki: *Welding in the World*, **49**(2005), 22.
(62) D. J. Abson and R. J. Pargeter: *Int. Met. Rev.*, **31**(1986), 141.
(63) D. A. Porter and K. E. Easterling: Phase Transformations in Metals and Alloys, Chapman & Hall, London, (1992), 10.
(64) M. C. Flemings: Solidification Processing, Tapir Academic Press, Trondheim, (2001), 291.
(65) D. G. McCartney: *Int. Met. Rev.*, **34**(1989), 247.
(66) W. Kurtz and D. J. Fisher: Fundamentals of Solidification, Trans. Tech. Publications, Switzerland, (1998).
(67) H. K .D. H. Bhadeshia and L. E. Svensson: Mathematical Modelling of Weld Phenomena, Institute of Materials, London, (1993), 109-177.
(68) R. A. Ricks, P. R. Howell and G. S. Barritte: *J. Materials Science*, **17**(1982), 732.
(69) T. Koseki and G. Thewlis: *Mater. Sci. Technol.*, **21**(2005), 867.
(70) S. J. Jones: Ph.D. Thesis, University of Cambridge, Cambridge, (1996).
(71) A. R. Mills, G. Thewlis and J. A. Whiteman: *Mater. Sci. Technol.*, **3**(1987), 1051.
(72) Ø. Grong, A. O. Kluken, H. K. Hylund, A. L. Dons and J. Hjelen: *Metall. Mater. Trans. A*, **26A**(1995), 525.
(73) J. R. Yang and H. K. D. H. Bhadeshia: *Mater. Sci. Technol.*, **5**(1989), 93.
(74) H. Mabuchi, R. Uemori and M. Fujioka: *ISIJ Int.*, **36**(1996), 1406.
(75) Y. Nagai, H. Fukami, H. Inoue, T. Nakashima, A. Kojima, T. Kajitani, T. Adachi and Y. Yoshida: Proceedings of OMAE03, 22nd International Conference on Offshore Mechanics and Arctic Engineering, Cancun, Mexico, (2003), OMAE2003-37436.
(76) Y. Terada, A. Kojima, A. Kiyose, T. Sawai, R. Uemori, K. Tanaka, T. Nakashima, T. Kadoya, M. Murata and T. Kawaguchi: Proceedings of OMAE03, 22nd International

Conference on Offshore Mechanics and Arctic Engineering, Cancun, Mexico, (2003), OMAE2003-37391.

(77) I. Madariaga and I. Gutierrez: *Acta. Mater.*, **47**(1999), 951.

(78) S. S. Babu: *Current Opinion in Solid State & Materials Science*, **8**(2004), 267.

(79) H. K. D. H. Badeshia: *Bainite in Steels*, The Institute of Materials, London, (1992).

(80) G. Thewlis, J. A. Whiteman and D. J. Senogles: *Mater. Sci. Technol.*, **13**(1997), 257.

(81) G. Thewlis: *Sci. Tech. Weld. Joining*, **5**(2000), 365.

(82) J. -S. Byun, J. -H. Shim, Y. W. Cho and D. N. Lee: *Acta Mater.*, **51**(2003), 1593.

(83) H. Goto, K. -I Miyazawa and K. Tanaka: *ISIJ Int.*, **35**(1995), 286.

(84) J. -H. Shim, Y. -J. Oh, J. -Y. Suh, Y. W. Cho, J. -D. Shim, J. -S. Byun and D. N. Lee: *Acta Mater.*, **9**(2001), 2115.

(85) C. van der Eijk, Ø. Grong and J. Walmsley: *Mater. Sci. Technol.*, **16**(2000), 55.

(86) Ø. Grong and O. M. Akselsen: *Metal Constructions*, **18**(1986), 557.

(87) G. Thewlis: *Mater. Sci. Technol.*, **22**(2006), 153.

(88) R. A. Ricks, G. S. Barritte and P. R. Howell: Proc. Inter. Conference on Solid-Solid Phase Transformation, The Metallurgical Society of AIME, Pittsburgh, Pennsylvania, USA, (1982), 463.

(89) F. J. Barbaro, P. Krauklis and K. E. Easterling: *Mater. Sci. Technol.*, **5**(1989), 1057.

(90) A. Nicholson and T. Gladman: *Ironmaking Steelmaking*, **13**(1986), 53.

Part II: Oxygen control during manufacturing of CeS-based grain refiners for steel

2.1 Introduction

Cerium-treatment is widely used for inclusion engineering and grain size control of steel[1-3]. This is because cerium will form complex oxides and sulphides when added to liquid steel, with the ability to nucleate different types of ferrite during subsequent steel processing in the solid state[4]. However, a major problem with the use of pure cerium as an alloying element is that the element is not protected by a stable oxide layer, meaning that it will gradually disintegrate in contact with air. This disintegration is believed to be related to an intermediate formation of Ce_2O_3 on the cerium surface. The Ce_2O_3 oxide will subsequently be converted into the more stable CeO_2 oxide, which continuously destroys the protective film and allows the oxidation process to proceed in a destructive manner[5,6].

Also during manufacturing of CeS-based grain refiners for steel, which in the present case involves melting, superheating and quenching of a premixed Ce+FeS_2+Al blend[7], the combination of a high oxygen affinity and the lack of protection from a dense surface oxide layer creates serious problems. In practice, it is extremely difficult to achieve sufficiently low p_{O_2} levels in the surrounding gas atmosphere which will eliminate the oxidation of liquid cerium. One option is to use a vacuum furnace equipped with a graphite heating element. Following refilling with a high-purity shielding gas (e.g. argon) such heating elements can protect the molten cerium from oxidising at temperatures approaching 2000 ˚C because carbon will be in control of the oxygen level at these temperatures[8]. Still cerium will be unprotected within an intermediate temperature range, where its affinity to oxygen is higher compared with carbon[9]. This, in turn, requires the use of rapid heating of the melt in order to avoid severe oxidation of cerium due to reactions with the surrounding gas atmosphere.

The main objective of the present investigation is to clarify the conditions under which CeS-based grain refiners can be manufactured without excessive cerium oxide formation during liquid metal processing. The experiments will be carried out in a small laboratory furnace equipped with a graphite heating element, where both the temperature-time programme and the partial pressure of oxygen can be accurately controlled and monitored throughout the melting trials. Optical and electron microscopy is then employed to characterise the different phases which form following heating and cooling of the samples. At the same time their thermodynamic stability at elevated temperatures is evaluated and compared based on calculations of the critical oxygen partial pressure for cerium oxide and cerium oxysulphide formation.

2.2 Methodology

2.2.1 Small-scale vacuum furnace

Figure 2.1 shows a schematic illustration of the vacuum furnace used in the melting experiments. This furnace is originally designed for in-situ wetting angle measurements. As a consequence, the furnace is only equipped with a sample holder capable of heating substrates/crucibles with an outer diameter of 10 mm. Small tantalum crucibles were therefore machined to fit this sample holder. Tantalum has good refractory properties, is easy to machine and has a low solubility in contact with liquid cerium.

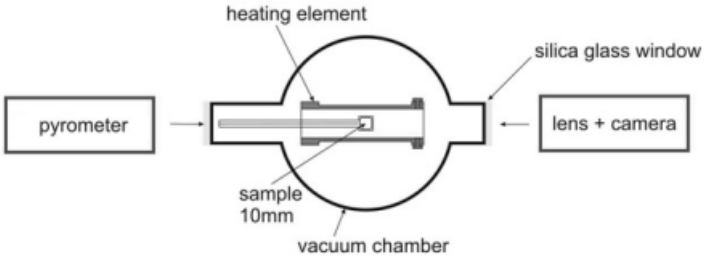

Figure 2.1 Schematic illustration of the vacuum furnace, which consists of an outer vacuum chamber, a graphite heating element and a sample holder. A camera system and pyrometer are mounted on the outside on each side of the furnace.

To protect the sample from oxidising the vacuum chamber is constantly flushed with high purity argon during the experiments. The argon flowing out of the furnace passes through a zirconia oxygen sensor (Sensotec RX2100), which measures the partial pressure of oxygen. The RX2100 sensor can measure a partial pressure of oxygen from 1 to 10^{-26} atm with an accuracy of +/- 1%[10]. When starting the argon flushing, the oxygen partial pressure will after a certain period of time stabilize itself at around 10^{-15} atm. Such low oxygen levels are obtainable because the argon passes through a separate furnace, containing heated magnesium, before entering the vacuum furnace.

The heating element is constructed of graphite, as are all the other heated parts of the furnace. A calibrated pyrometer, with an operating temperature range from 900-2400 ˚C, continuously measures the temperature of the crucible. In-situ photography of the crucible is also possible during the experiments, as shown in Figure 2.2.

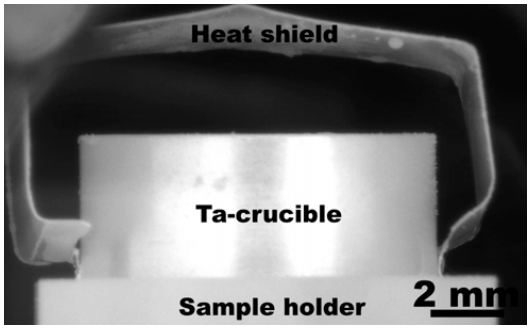

Figure 2.2 In-situ photography of the tantalum crucible during heating.

2.2.2 Charge materials

The charge materials used in the melting experiments are Ce, FeS_2 and Al. These have a purity of at least 99.9% and were obtained from different commercial manufacturers. To avoid oxygen contamination of the charge materials, an argon-filled glove box with oxygen and humidity levels <<0.1 ppm was used for storage. All charging of materials into the tantalum crucibles was done inside the glove box.

2.2.3 Melting experiments

In order to evaluate the extent of oxygen absorption during superheating of the melt up to 2000 ˚C, two different heating rates were employed, i.e. 60 and 1000 ˚C/min. In both cases the blend of Ce+FeS_2+Al was adjusted to achieve the target composition of 86.8 wt% Ce, 6 wt% S, 5.2 wt% Fe and 2 wt% Al. Note that the aluminium is added to promote Ce_3Al formation in the as-solidified samples, since previous experiments have shown that this level is sufficient to stabilise cerium during subsequent storage in air at room temperature.

2.2.4 Optical microscopy

Standard metallographic techniques were used to prepare cross section samples for optical microstructure characterisation. Because cerium corrodes vigorously in water, wet grinding was carried out using an alcohol based lubricant. The microstructure was readily revealed in the optical microscope without etching. Metallographic examination was preformed using a conventional Zeiss reflecting light optical microscope.

2.2.5 Microprobe analyses

A JEOL JXA-8500F electron probe micro analyser (EPMA) was used to study the as-solidified microstructures of the samples. The JXA-8500F is a high performance thermal field emission electron microprobe analyser and is equipped with 5 wavelength dispersive X-ray spectrometers

(WDS) and a backscatter electron (BSE) detector. A cross-section of each sample was prepared and the different phases characterised and identified using BSE imaging and WDS analyses. All these investigations were carried out at an acceleration voltage of 15 keV and a probe current of 30 nA.

2.3 Results

In the following, the main results from the microstructure and phase characterisations will be presented.

2.3.1 Measured oxygen levels inside the vacuum furnace during heating and cooling

Figure 2.3 shows plots of the recorded crucible temperature and the measured p_{O_2} level inside the vacuum furnace as a function of time during a typical rapid heating cycle (i.e. ~1000 ˚C/min).

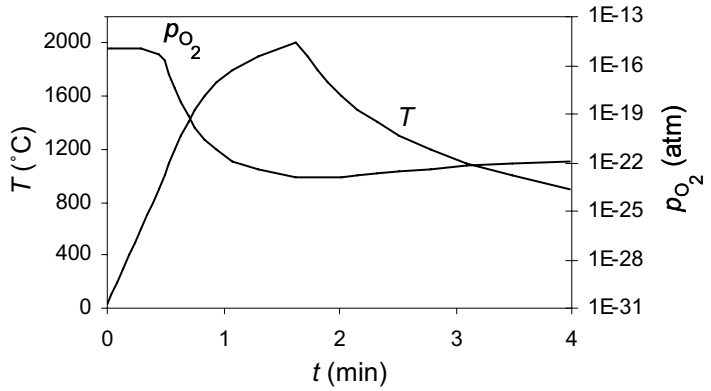

Figure 2.3 Graphical representations of the measured crucible temperature T and the partial pressure of oxygen p_{O_2} inside the vacuum furnace during a typical rapid heating cycle (~1000 ˚C/min).

As expected, the use of a separate gas cleaning system implies that the partial pressure of oxygen in the argon shielding gas is reduced to about 10^{-15} atm before it is allowed to enter the vacuum furnace. During initial heating of the sample, p_{O_2} starts to decrease as the temperature inside the furnace increases, reaching a lower threshold of about 10^{-22} atm after about 1 min when T > 1800 ˚C. This oxygen level is then largely maintained throughout the remaining melting experiment, also when the crucible temperature drops again below 1000 ˚C on subsequent cooling.

2.3.2 Phase characterisation

Figures 2.4(a) and 2.4(b) show two BSE images of the as-solidified microstructures taken at high magnification.

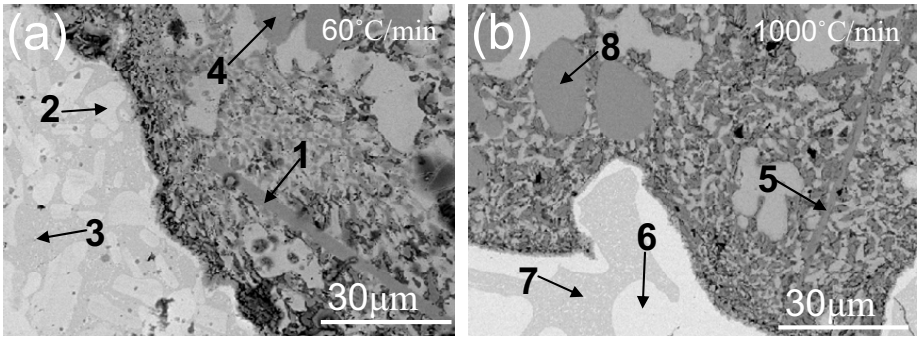

Figure 2.4 Two BSE images showing the as-solidified microstructures at high magnification. The applied heating rates of the samples in image **(a)** and **(b)** are 60 and 1000 ˚C/min, respectively. The arrows in the images indicate the position of the eight point analyses reported in Table 2.1.

The eight WDS point analyses shown in Table 2.1 were carried out at the surface positions indicated by the arrows in the two electron micrographs. In the point analyses 1, 5, 4 and 8 the ratio between the constituent elements corresponds to the two intermetallic phases Ce_2O_2S and CeS, respectively. In addition, separate phases of Ta and Fe are present, as indicated by the point analyses 2, 3, 6 and 7. This shows that some reaction has occurred between Fe dissolved in the melt and the Ta crucible during heating and cooling.

Table 2.1 WDS point analyses of various phases detected in the as-solidified samples. Point analyses No. 1-4 refer to the sample being heated at 60 ˚C/min, whereas point analyses No. 5-8 refer to the sample being heated at 1000 ˚C/min. The numbers are given in at%.

No.	Al	O	S	Ta	Ce	Fe	Total
1	0.0	39.5	19.2	0.1	41.0	0.2	100.0
2	0.9	6.2	0.0	85.7	0.6	6.6	100.0
3	2.4	4.1	0.0	56.7	0.5	36.3	100.0
4	0.0	2.0	47.3	0.0	50.6	0.1	100.0
5	0.0	40.9	18.7	0.0	40.3	0.1	100.0
6	0.9	5.6	0.3	84.0	0.4	8.8	100.0
7	1.9	6.9	0.1	53.0	0.9	37.2	100.0
8	0.1	2.8	46.0	0.0	51	0.1	100.0

Figures 2.5(a) and 2.5(b) show optical micrographs of the same surface areas being displayed previously in Figures 2.4(a) and 2.4(b). These are taken at low magnification. The Ce_2O_2S and CeS phases, which have been identified by point analyses in Table 2.1, can also be recognised in these optical images by their morphologies, as shown by the arrows in Figure 2.5. A qualitative comparison between the two micrographs in Figure 2.5 reveals that the fraction of Ce_2O_2S needles in image (a) is significantly higher than in image (b). At the same time the fraction of CeS particles is seen to be highest in image (b). These results show that oxygen absorption from the surrounding shielding gas, as affected by the applied heating rate, is critical in the sense that it affects the phase balance between Ce_2O_2S and CeS in the as-solidified samples.

Moreover, it is evident from Figure 2.5 that the Ta-Fe reaction has mainly occurred at the interface between the Ta crucible and the melt. Apparently, the Ta-Fe compound formation is most severe in the sample being heated at 60 ˚C/min, suggesting that this is also a kinetic-controlled reaction.

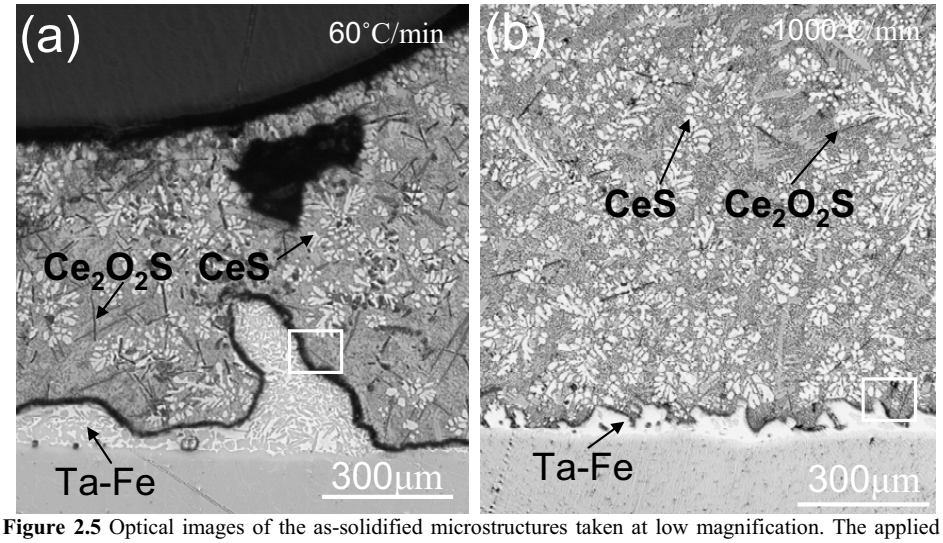

Figure 2.5 Optical images of the as-solidified microstructures taken at low magnification. The applied heating rates of the samples in image **(a)** and **(b)** are 60 and 1000 ˚C/min, respectively. The different phases which previously have been identified by WDS point analyses are indicated by the arrows in the micrographs.

2.4 Discussion

In the following, the conditions for oxidation formation during manufacturing of CeS-based grain refiners for steel will be discussed more in detail, starting with an analysis of factors controlling the partial pressure of oxygen in the shielding gas at elevated temperatures.

2.4.1 Oxygen purification efficiency of graphite

As shown previously Figure 2.3, the oxygen level inside the furnace remains unchanged up to about 800 ˚C during heating. At higher temperatures p_{O_2} drops by several orders of magnitude. Similar oxygen profiles have been reported for resistant-heated graphite furnaces used for atomic absorption spectrometry[11,12]. In the latter case it is believed that the oxygen purification effect is caused by the following reaction[13]:

$$O_2(g) + 2C(s) = 2CO(g) \tag{2.1}$$

At low temperatures this reaction is kinetically limited by a high activation energy for formation of carbon-oxygen bonds at the graphite surface. But at higher temperatures the activation energy is greatly reduced, which means that the graphite becomes increasingly reactive towards oxygen[14]. Under such conditions the oxygen partial pressure is controlled by the rate at which the oxygen can diffuse towards the graphite surface, allowing p_{O_2} to drop below 10^{-22} atm, as observed in the present investigation.

It should be noted that the physical meaning of such a low p_{O_2} in terms of numbers of O_2 molecules inside the furnace is that the oxygen content is practically zero. This means that any O_2 molecules entering the furnace chamber will immediately be picked up by the graphite heating element. It is therefore reasonable to assume that the oxidation of cerium will mainly occur during heating in the temperature range below, say, 1600 to 1800 ˚C, where p_{O_2} is significantly higher than 10^{-22} atm.

2.4.2 Critical oxygen partial pressure for cerium oxide and cerium oxysulphide formation

During heating of cerium and sulphur in the presence of oxygen, the following three oxidation reactions may occur:

$$2Ce + O_2(g) + S = Ce_2O_2S \tag{2.2}$$

$$2Ce + 1.5O_2(g) = Ce_2O_3 \quad (2.3)$$

$$Ce + O_2(g) = CeO_2 \quad (2.4)$$

By utilizing appropriate input data for the Gibbs energy of cerium oxide and oxysulphide formation[8], the critical p_{O_2} needed to form Ce_2O_2S, Ce_2O_3 and CeO_2 as a function of temperature has been calculated. In Figure 2.6 these p_{O_2} values have been superimposed on the measured temperature and oxygen profiles shown previously in Figure 2.3.

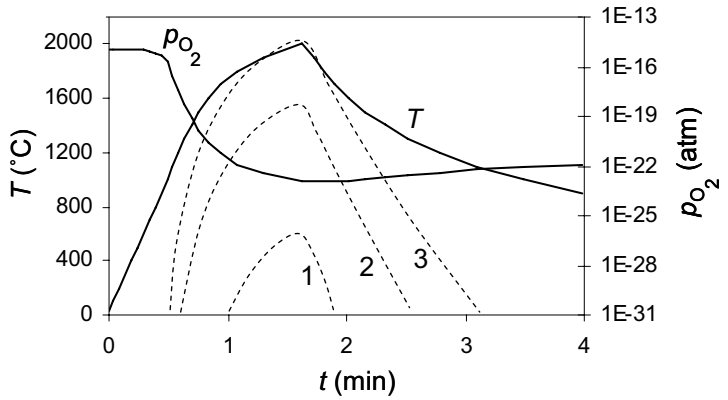

Figure 2.6 Graphical representation of the measured temperature *T* and the partial pressure of oxygen p_{O_2} inside the vacuum furnace during a typical rapid heating cycle (~1000 ˚C/min). Plots 1-3 show the corresponding partial pressure of oxygen needed to form (1) Ce_2O_2S, (2) Ce_2O_3 and (3) CeO_2, respectively at different temperatures. These calculations are done using thermodynamic input data from Kubaschewski[8].

As the time evolves and the temperature inside the furnace increases, the stability of the different oxides decreases correspondingly, as shown in Figure 2.6. When the temperature exceeds 1800 ˚C the measured oxygen level inside the furnace drops below the partial pressure needed to form CeO_2 and Ce_2O_3. On the other hand, Ce_2O_2S may still form and hence, Ce_2O_2S is the most likely oxide phase to be found in the as-solidified samples. This agrees well with the WDS point analyses in Table 2.1.

2.4.3 Kinetics of oxygen absorption during heating

Figure 2.7 shows a schematic drawing of the Ta crucible inside the vacuum furnace, where the partial pressure gradient of oxygen between the bulk gas phase $p^b_{O_2}$ and the bare cerium surface $p^s_{O_2}$ also is indicated.

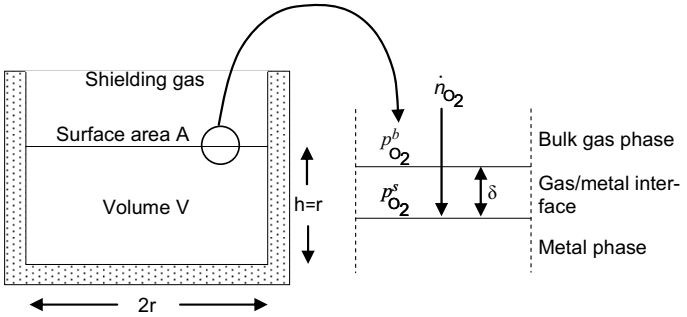

Figure 2.7 Idealised kinetic model for absorption of oxygen during heating of the Ce-melt inside the vacuum furnace.

Referring now to this figure, the molar flux $\dot{n}_{O_2}$ of O_2 (in mol s^{-1}) across the stagnant gaseous boundary layer of thickness δ (in m) at the gas/metal interface can be expressed as[15]:

$$\dot{n}_{O_2} = \frac{dn_{O_2}}{dt} = \frac{D_{O_2} A}{\delta RT}\left(p^b_{O_2} - p^s_{O_2}\right) = k_{O_2} A\left(p^b_{O_2} - p^s_{O_2}\right) \tag{2.4}$$

where D_{O_2} is the oxygen diffusivity (in m^2 s^{-1}), R is the universal gas constant (in m^3 atm K^{-1} mol^{-1}), T is the absolute temperature (in K) and k_{O_2} is the overall mass transfer coefficient of oxygen (in mol m^{-2} s^{-1} atm^{-1}).

Based on Eq. (2.4) it is possible to obtain a simple expression for the molar concentration of atomic oxygen per unit volume of the Ce-melt C_O (in mol m^{-3}). Taking the surface area to volume A/V ratio of the Ce-melt equal to $1/r$ (where r is the radius of the cylindrical Ta crucible), we arrive at:

$$C_O = 2\frac{A}{V}\int_0^t k_{O_2}\left(p^b_{O_2} - p^s_{O_2}\right)dt = \frac{2}{r}\int_0^t k_{O_2}\left(p^b_{O_2} - p^s_{O_2}\right)dt \tag{2.5}$$

In the limiting case, where both k_{O_2}, $p^b_{O_2}$ and $p^s_{O_2}$ are constant and independent of temperature (and thus time), the integral reduces to:

$$C_O = \frac{2}{r} k_{O_2} \left(p^b_{O_2} - p^s_{O_2} \right) t \tag{2.6}$$

Eq. (2.6) shows, in an explicit manner, the main variables that come into play and contribute to the absorption of oxygen during heating of cerium inside the vacuum furnace. In general, the use of a small Ta crucible implies that the oxygen pick-up will be favoured by a large *A*/*V* ratio of the Ce-melt. Under such conditions oxygen purification of the shielding gas becomes extremely important. It follows that gas cleaning, employing heated magnesium powder in combination with the protection provided by the graphite heating element, are sufficient to avoid extensive oxidation at temperatures above, say, 1600 to 1800 ˚C. Still, cerium is unprotected within an intermediate temperature range where $p^b_{O_2} >> p^s_{O_2}$. This, in turn, requires the use of rapid heating of the melt in order to minimise oxygen pick-up from the surrounding gas atmosphere. In the present small-scale laboratory experiments a heating rate of about 1000 ˚C/min is required to limit the conversion of CeS to Ce_2O_2S, which is an undesirable microconstituent in the grain refiners.

2.5 Conclusions

The basic conclusions that can be drawn from this investigation are as follows:

1. In a pure metallic form, cerium is a difficult element to handle because it will readily oxidise and disintegrate at room temperature in contact with air. Thus, in order to avoid oxygen contamination of the cerium both charging and storage of the material must be done inside a glove box under the shield of an inert gas.

2. Also during manufacturing of CeS-based grain refiners for steel, the high reactivity of cerium towards oxygen creates serious problems. In particular, in small-scale melting trials involving the use of cerium, oxygen purification of the shielding gas becomes extremely important. Experiments carried out inside the laboratory vacuum furnace show that gas cleaning, employing heated magnesium powder in combination with the protection provided by the graphite heating element, are sufficient to prevent cerium from oxidising at temperatures above, say, 1600 to 1800 ˚C.

3. However, at intermediate temperatures cerium is unprotected and will readily oxidise, unless the reaction is kinetically suppressed through the use of rapid heating. For example, when a blend of Ce+FeS_2+Al is melted inside a Φ 8 mm Ta crucible, a heating rate of about 1000 ˚C/min is required to limit the conversion of CeS to Ce_2O_2S. The cerium oxysulphide is the thermodynamic stable phase in the presence of oxygen and sulphur, but is an undesirable microconstituent in the grain refiners and should therefore be avoided.

2.6 References

(1) A. Ohmori, F. Kawabata and K. Amano: Patent EP 1 035 222 A1, (2000).

(2) Ø. Grong and O. S. Klevan: Patent WO 2001/57280, (2001).

(3) P. Grahle, R. Ruch and H. Stiegeler: Patent WO 2005/026396, (2005).

(4) G. Thewlis: *Mater. Sci. Technol.*, **22**(2006), 153.

(5) J. Loriers: *Compt. rend.*, **229**(1949), 547.

(6) W. L. Phillips Jr.: *J. Less-Common Metals*, **7**(1964), 139.

(7) Ø. Grong, L. Kolbeinsen, C. van der Eijk and G. Tranell: *ISIJ Int.*, **46**(2006), 824.

(8) O. Kubaschewski and C. B. Alcock: Metallurgical Thermochemistry. Pergamon Press, Sydney, (1979).

(9) W. G. Wilson, D. A. R. Kay and A. Vahed: *JOM*, **26**(1974), 14.

(10) Sensotec RX2100: http://www.cambridge-sensotec.co.uk/pdfs/Rapidox_2100_Instruction_Manual_version_1.5.pdf, (2004), Access Date: 12.08.2008.

(11) B. V. L'vov. and G. N. Ryabchuk: *Spectrochimica Acta*, **37B**(1982), 673.

(12) S. B. Chang, C. L. Chakrabarti, T. J. Huston and J. P. Byrne: *Fresenius Z. Anal. Chem.*, **322**(1985), 567.

(13) R. E. Sturgeon, K. W. M. Siu and S. S. Berman: *Spectrochimica Acta*, **39B**(1984), 213.

(14) A. Blanchard: Appendix 2: The Thermal Oxidation of Graphite, IAEA-TECDOC-1154, (2003), 207.

(15) T. Rosenqvist: Principles of Extractive Metallurgy, 2nd Ed., Tapir Academic Press, Trondheim, (2004).

Part III: Phase relations in Ce-Al-Fe-S based grain refiners for steels

3.1 Introduction

Currently, structural steels are strengthened by a series of different techniques. Usually a fine grain structure is achieved by combining heat treatment and thermo-mechanical processing. The energy saving potential of applying cheaper and faster strengthening methods is great and highly interesting in a time where access to energy is predicted to decline. For example, adding a specially designed master alloy with the ability to produce a fine grain structure in steel is possible and also to some extent exploited by the steel manufactures[1-3].

Several systems with the potential of being used as grain refiners for steel have been studied over the last ten years. One of the most promising ones is the cerium-sulphur system[4]. Cerium has a strong affinity to sulphur and will, almost always, form a compound with sulphur when both elements are present in molten steel[5,6]. A fine distribution of CeS particles in the steel matrix during the austenite to ferrite transformation can shift the nucleation process from the austenite grain boundaries to sites located intragranularly[7]. This process has been studied extensively since the nineteen seventies in low alloy steel weld metals, where complex oxide and sulphur inclusions contribute to acicular ferrite formation[8-11]. Acicular ferrite has a plate like structure offering a combination of high strength and toughness. Acicular ferrite can only be achieved if the number density of CeS particles in the steel matrix is sufficiently high[12,13]. Unfortunately, modern steelmaking involving continuous casting does not allow large additions of ferroalloys late in the process due to practical problems related to a severe temperature drop after the addition and incomplete dissolution and mixing of the alloy in the liquid. Therefore, in order to maintain a good nucleation potential, the master alloy needs to be highly concentrated and contain between 5 and 10 wt% sulphur[12]. Cerium is in this context interesting, since it can dissolve large amounts of sulphur in the liquid state[14]. By fully exploiting the potential of cerium as a sulphur carrier, effective grain refiners can also be produced for continuously cast steels containing a high number density of embedded CeS particles.

A major problem with cerium is that the metal is not protected by a stable oxide layer[15], meaning that it will gradually disintegrate in contact with air. However, as shown in Part II of the thesis, balanced aluminium additions are beneficial to stabilise cerium during storage in an oxygen-rich environment, due to the resulting Ce_3Al compound formation. All melting trials with cerium preformed in the present investigation are therefore carried out using aluminium as an alloying element, along with FeS_2 (pyrite) acting as the sulphur source. However, oxidation of the cerium melt (i.e. Ce_2O_2S formation) may still occur during heating if the oxygen level in

the furnace is not kept extremely low. One way to overcome this problem is to use a furnace equipped with a graphite heating element, which will act as an oxygen scavenger at elevated temperatures due to the increased affinity of carbon towards oxygen. This, in combination with rapid heating of the melt, makes it possible to reduce the oxygen pick-up from the surrounding gas atmosphere to an acceptable level, as previously shown in Part II of the thesis.

The binary phase diagram which exists today for Ce-S is not fully established within the composition range of specific interest (i.e. from zero and up to 50 at% S)[14]. Therefore, the liquidus temperature is only indicated by a dotted line, suggesting a solubility of sulphur in cerium at 2000 ˚C of about 33 at% sulphur (10 wt% sulphur). The main objective of the present study is thus to provide new and more accurate information about the solubility of sulphur in liquid cerium, and in particular how elements such as aluminium and iron influence the CeS formation and the resulting phase relations. This is done using microprobe and optical microscopy for characterisation of the different constituent phases in the as-solidified samples, and point counting for quantitative volume fraction measurements.

3.2 Experimental

In the following, the experimental setup will be presented in more details. Some of the experimental techniques and equipments used in this investigation have previously been described in the Part II of the thesis, including:

- Microprobe investigation
- Optical microscopy
- Small-scale vacuum furnace

3.2.1 Materials

A key issue in the manufacture of CeS-based grain refiners for steel is to use an appropriate sulphur source that does not lead to undesirable side reactions and a low sulphur yield. Therefore, sulphur cannot be added in a pure form because the boiling point is too low, which means that the element will evaporate during heating. A better solution would be to use FeS_2 (99.9%) as a sulphur source, as done in the present investigation, because FeS_2 is easy to obtain, is richer in sulphur compared to FeS and more stable than elemental sulphur at elevated temperatures. The two other charge materials used were cerium and aluminium metal with 99.9% and 99.999% purity, respectively. These materials were obtained from different commercial manufacturers, i.e. Alfa Aesar, PI-KEM, and Hydro Aluminium.

To avoid oxygen contamination of the charge materials, an argon filled glove box with oxygen and humidity levels <<0.1 ppm was used for storage. All materials were charged into the tantalum crucibles inside the glove box.

3.2.2 Melting experiments

Four different levels of sulphur additions in cerium were investigated. In addition, 2 and 5 wt% aluminium was added to promote Ce_3Al formation. This gives a total of eight melting experiments for the four different nominal sulphur levels aimed at; 0, 2, 4 and 6 wt%, respectively. The weight of each sample was approximately 0.8 g and the targeted chemical compositions are listed in Table 3.1.

Table 3.1 Target chemical compositions of the eight different charge mixtures in wt%.

Sample No.	Al added	Fe added	S added	Balance
1	2	0	0	Ce
2	2	1.7	2	Ce
3	2	3.5	4	Ce
4	2	5.2	6	Ce
5	5	0	0	Ce
6	5	1.7	2	Ce
7	5	3.5	4	Ce
8	5	5.2	6	Ce

According to the Ce-S phase diagram[14], the desired solubility level of sulphur can only be achieved if cerium is melted and superheated to about 2000 ˚C. Figure 3.1 shows a record of the actual crucible temperature and the partial pressure of oxygen (p_{O_2}) in the surrounding gas atmosphere inside the furnace during a typical melting experiment.

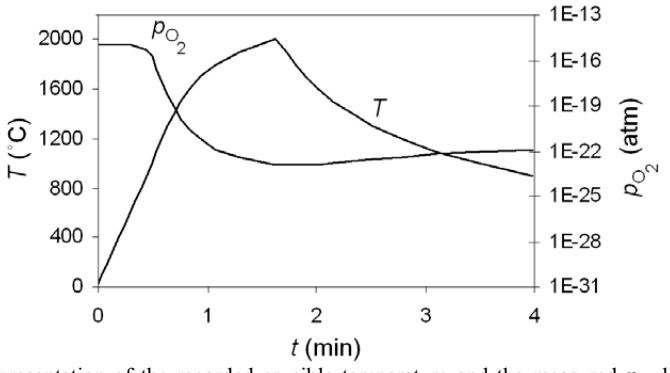

Figure 3.1 Representation of the recorded crucible temperature and the measured p_{O_2} level inside the vacuum furnace as a function of time during a typical rapid heating cycle (i.e. ~1000 ˚C/min).

As the temperature in the furnace is rising, the p_{O_2} is decreasing due to the increased affinity of carbon towards oxygen at elevated temperatures. Oxygen pick-up in the melt during heating will primarily occur within the intermediate temperature range below 1600 to 1800 ˚C, where the protection provided by the graphite heating element is low, as previously shown in Part II of the thesis.

3.2.3 Volume fraction measurements

Standard point counting techniques were used to measure the volume fraction of the different constituent phases present in each sample[16]. This was done employing an optical microscope, equipped with an 11x11 ocular grid at 200x magnification. A total of six different fields were counted per sample, from which the mean values and the standard deviation of the means were calculated. The measured volume fractions can then be compared with the calculated ones, based on the following equation:

$$f_{CeS} = \frac{m_{CeS} / \rho_{CeS}}{m_{alloy} / \rho_{alloy}} \tag{3.1}$$

where m_{alloy} is the total weight of the samples and m_{CeS} is the total mass of CeS in the alloy, assuming 100% sulphur yield. The symbols ρ_{alloy} and ρ_{CeS} in the equation represent the corresponding densities of the two phases.

In order to ensure a highest possible confidence in the calculations, measured values for ρ_{alloy} should be used. In the present investigation, the Archimedes principle of buoyancy was adopted to measure the density of samples No. 1, 4, 5 and 8. By extrapolating the data between the limits 0 to 6 wt% S, separate density plots for the two different aluminium levels were constructed, as shown in Figure 3.2.

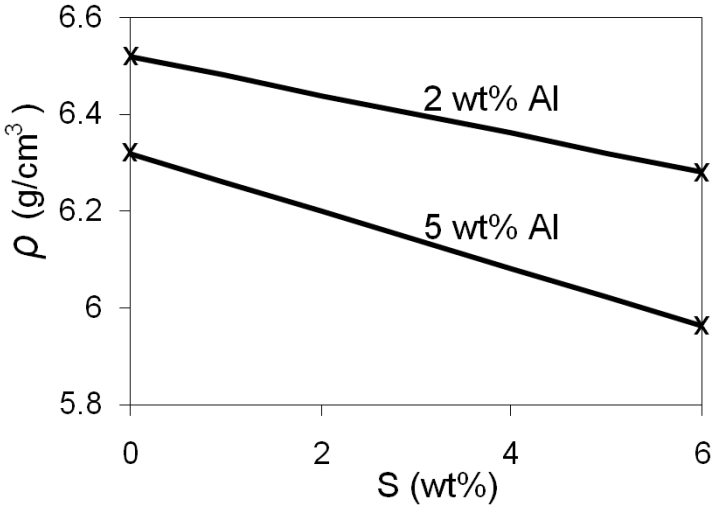

Figure 3.2 Plots showing the measured density of the Ce-2 wt% Al and the Ce-5 wt% Al base alloys, respectively as a function of the added sulphur content.

3.3 Results

In the following, the main results from the microstructure and phase characterisations will be presented. Note that the chemical analyses reported below refer to samples No. 4 and 8, which contains a representative selection of the phases being present in all eight samples.

3.3.1 Microprobe investigation of sample No. 4

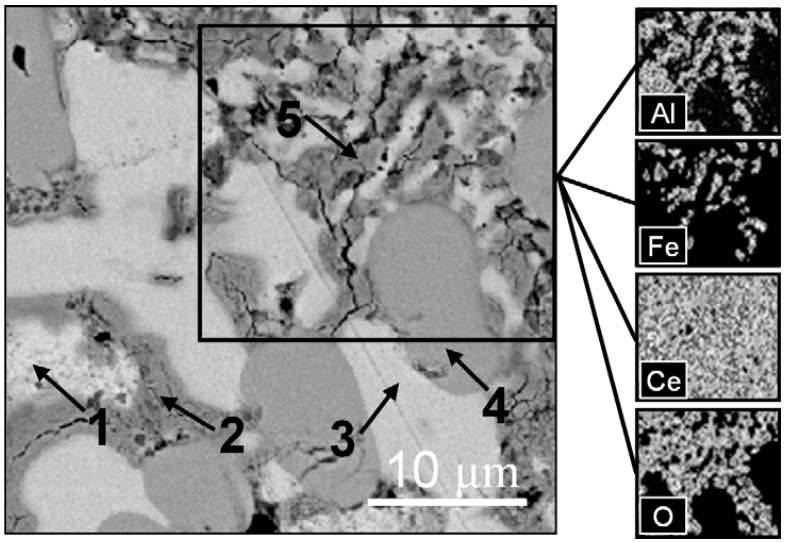

Figure 3.3 BSE image of sample No. 4 along with element distribution maps for aluminium, iron, cerium and oxygen. The arrows indicate the position of the five point analyses reported in Table 3.2.

Figure 3.3 shows measured element distribution maps for aluminium, iron, cerium and oxygen in sample No. 4. The scanned area is indicated by the rectangular box in the upper right corner of the BSE image. In addition, five WDS point analyses have been carried out at the surface positions indicated by the arrows in the electron micrograph. The results from the point analyses are summarised in Table 3.2.

Table 3.2 Point analyses of various phases detected in sample No. 4. The numbers are given in at%.

No.	O	S	Ta	Al	Ce	Fe
1	14.8	0.0	0.1	0.9	84.1	0.1
2	63.6	0.1	0.0	0.4	35.8	0.1
3	3.9	0.1	0.1	23.3	72.5	0.1
4	2.8	46.1	0.0	0.1	51.0	0.0
5	3.7	0.0	0.0	0.0	33.3	62.9

The main elements found in positions 1 and 2 are cerium and oxygen. Because this area shows signs of surface corrosion, it is reasonable to assume that the γ-Ce has been oxidised either during or immediately after the metallographic preparation. Hence, this phase is most likely γ-Ce provided with a surface layer of Ce_2O_3 or CeO_2. In point analyses 3, 4 and 5 the ratio between the constituent elements corresponds to the intermetallic phases Ce_3Al, CeS and Fe_2Ce, respectively. Therefore, sample No. 4 contains a mixture of the four constituent phases Ce_3Al, CeS, Fe_2Ce and γ-Ce. A lamella-shaped ternary eutectic is also present, being encircled by the rectangular box in Figure 3.3. As judged from the element distribution maps this eutectic phase consists of Ce_3Al, Fe_2Ce and γ-Ce.

3.3.2 Microprobe investigation of sample No. 8

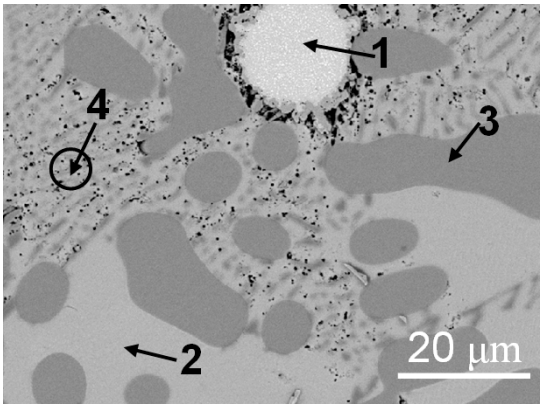

(a)

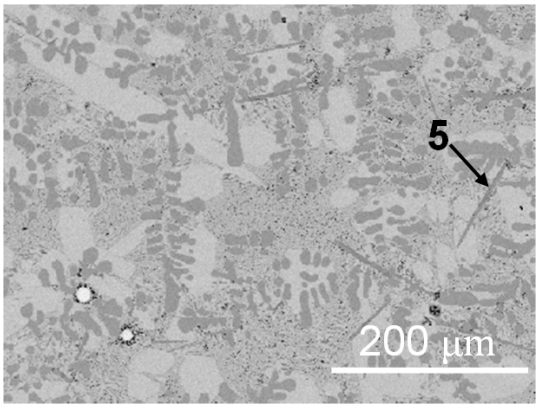

(b)

Figure 3.4 BSE image of sample No. 8 at **(a)** high and **(b)** low magnification, respectively. The arrows indicate the position of the five point analyses reported in Table 3.3.

Figures 3.4(a) and 3.4(b) show two BSE images of sample No. 8 at high and low magnification, respectively. The five point analyses shown in Table 3.3 were carried out at the surface positions indicated by arrows in the electron micrographs.

Table 3.3 Point analyses of various phases detected in sample No. 8. The numbers are given in at%.

No.	O	S	Ta	Al	Ce	Fe
1	4.9	0.2	52.7	4.5	1.2	36.5
2	3.3	0.3	0.1	23.0	73.2	0.1
3	1.2	47.0	0.0	0.2	51.4	0.2
4	6.6	0.1	0.0	20.4	59.6	13.3
5	35.9	20.0	0.0	0.3	43.5	0.3

The main elements found in position 1 are iron and tantalum. This shows that some reactions have occurred between iron dissolved in the melt and the tantalum crucible. The amount of tantalum found in the as-solidified structure is relatively small. However, near the crucible wall the Ta-Fe reaction is more vigorous, as can be seen from the segment delimited by the rectangular box in Figure 3.5.

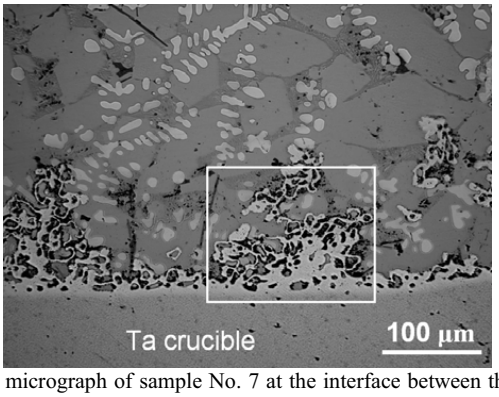

Figure 3.5 Light optical micrograph of sample No. 7 at the interface between the tantalum crucible and the as-solidified microstructure. The area encircled by the rectangular box shows how the dissolved iron has reacted with the tantalum crucible.

The phases observed in positions 2 and 3 are Ce_3Al and CeS. The phases in position 4, on the other hand, are too small to be analysed separately. However, by increasing the electron beam diameter, the average composition within the encircled area in Figure 3.4(a) can be measured. The point analysis from position 4 suggests a eutectic phase consisting of Ce_3Al and Fe_2Ce. In position 5 the ratio between the constituent elements points toward Ce_2O_2S, which is the most stable cerium oxysulphide, as previously shown in Part II of the thesis.

3.3.3 Microstructural evolution in samples No. 1 to 4

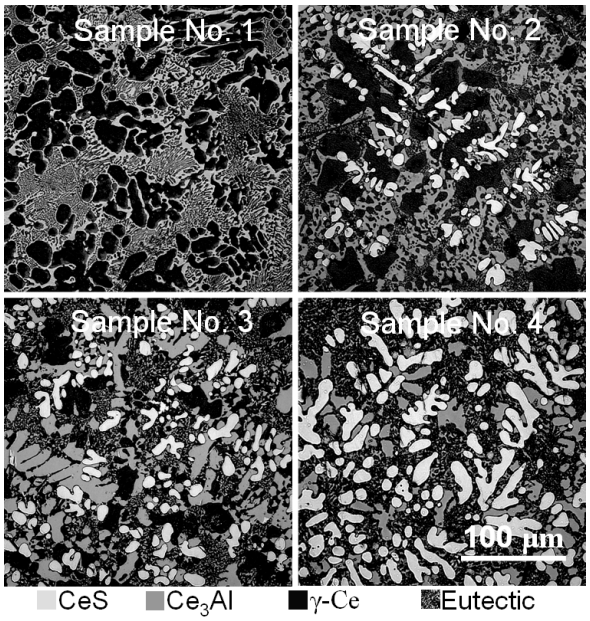

Figure 3.6 Light optical micrographs of samples No. 1, 2, 3 and 4.

Figure 3.6 shows four light optical micrographs of samples No. 1, 2, 3 and 4. In these micrographs different greytone levels are used to display the three main constituent phases CeS, γ-Ce and Ce_3Al, ranging from bright to dark. In-between these phases, the ternary eutectic is located, forming a fine dispersion of grey particles in the image. By comparing the images, the microstructural changes that occur due to the sulphur additions can be qualitatively observed. It is evident that cerium to an increasing extent reacts and form CeS when sulphur is added.

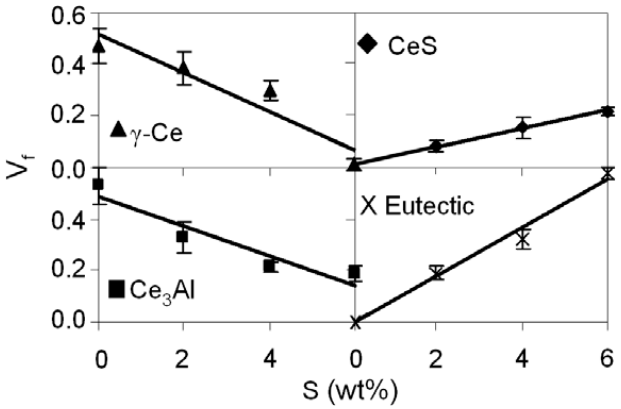

Figure 3.7 Summary of the results from the quantitative metallographic examinations of samples No. 1, 2, 3 and 4. The plots show how the phase distribution changes with increasing sulphur additions. The error bars in the graphs indicate the standard deviation of the volume fraction measurements.

In Figure 3.7 the results from the quantitative volume fraction measurements of the same phases are presented graphically. A closer inspection of the trend lines shows that increased sulphur addition promotes both the CeS component formation and the formation of the ternary eutectic phase consisting of Ce_3Al, Fe_2Ce and γ-Ce. Therefore, a corresponding reduction in the free Ce_3Al content is also observed because more Ce_3Al will be tied-up in the ternary eutectic phase as the sulphur level increases. Moreover, it follows from Figure 3.7 that the homogeneity of the samples is very good, as evidenced by the small error bars in the graphs representing the standard deviation of the measurements

3.3.4 Microstructural evolution in samples No. 5 to 8

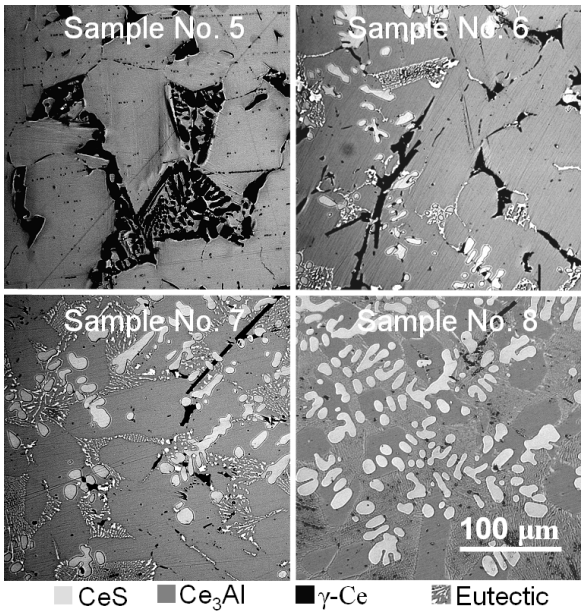

Figure 3.8 Light optical micrographs of samples No. 5, 6, 7 and 8.

Figure 3.8 shows four light optical micrographs of samples No. 5, 6, 7 and 8. As already pointed out in the previous section, the main constituents in the micrographs (CeS, γ-Ce and Ce_3Al) are displayed by their different greytone levels ranging from bright to dark, respectively. In between these phases, the eutectic phase forms a bright lamella structure. Also the amount of CeS is seen to increase when more sulphur is added to the samples.

Finally, the results from the quantitative volume fraction measurements carried out on samples No. 5, 6, 7 and 8 are presented graphically in Figure 3.9.

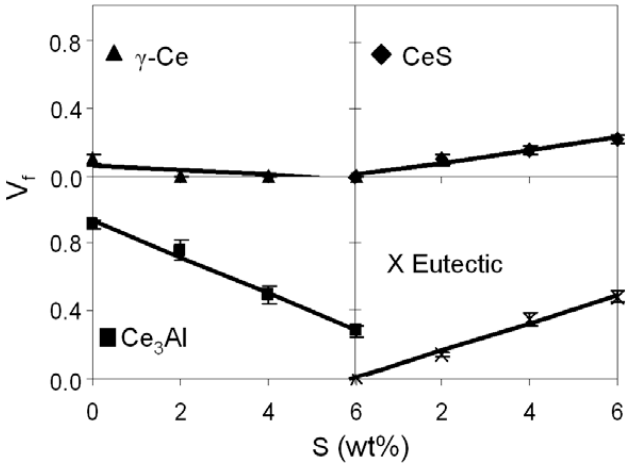

Figure 3.9 Summary of the results from the quantitative metallographic examinations of samples No. 5, 6, 7 and 8. The plots show how the phase distribution changes with increasing sulphur additions. The error bars in the graphs indicate the standard deviation of the volume fraction measurements.

As for the 2 wt% Al samples, the sulphur additions promote formation of CeS and a eutectic phase, which in this case consists of Ce_3Al and Fe_2Ce. Also a corresponding reduction in the free Ce_3Al content is observed with increasing sulphur additions as more Ce_3Al becomes tied-up in the eutectic phase.

3.4 Discussion

In the following, the conditions for CeS formation and the subsequent precipitation reactions occurring during cooling due to the FeS_2 and aluminium additions to liquid cerium will be discussed more in detail, starting with an analysis of the sulphur yield in the samples.

3.4.1 Sulphur yield using pyrite as charge material

In the melting experiments pyrite (FeS_2) is used as a charge material because it is rich in sulphur. However, this mineral is not stable at elevated temperatures, since it will start to dissociate at 743 ˚C, leading to $S_2(g)$ formation[14]:

$$FeS_2 = FeS + 1/2S_2(g) \tag{3.2}$$

Still, the $S_2(g)$ being released can dissolve in the cerium melt and in the limiting case lead to 100 wt% yield of sulphur, according to the overall dissolution reaction:

$$FeS_2 = \underline{Fe} + 2\underline{S} \tag{3.3}$$

In the other extreme, the $S_2(g)$ will just evaporate, which means that the sulphur yield is comparable with that of using pure FeS, in which only one mol of sulphur dissolves in the melt per mol iron added:

$$FeS_2 = \underline{Fe} + \underline{S} + 1/2S_2(g) \qquad (3.4)$$

In the latter case the advantage of using FeS_2 compared to FeS as a sulphur source is questionable, since Reaction (3.4) implies that all $S_2(g)$ is lost to the surrounding atmosphere.

The actual amount of sulphur being retained in the samples as CeS after the FeS_2 addition can be calculated from Eq. (3.1), using the measured volume fraction data for CeS reported previously in Figures 3.7 and 3.9 and the corresponding density data for the samples provided in Figure 3.2. The measured sulphur content in each sample is then plotted as a function of the total amount of sulphur added to the Ce-Al base alloys. The results are shown graphically in Figures 3.10(a) and 3.10(b).

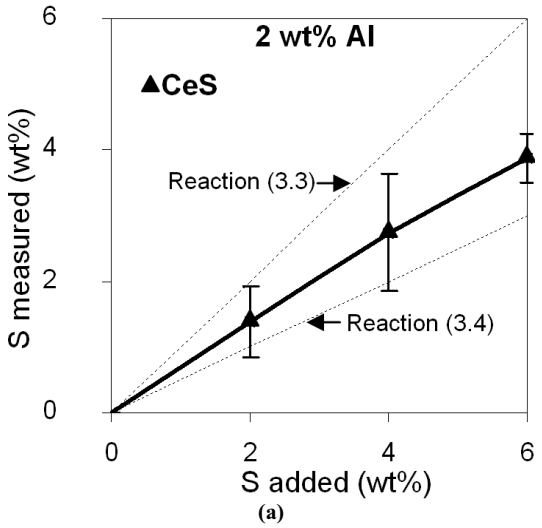

(a)

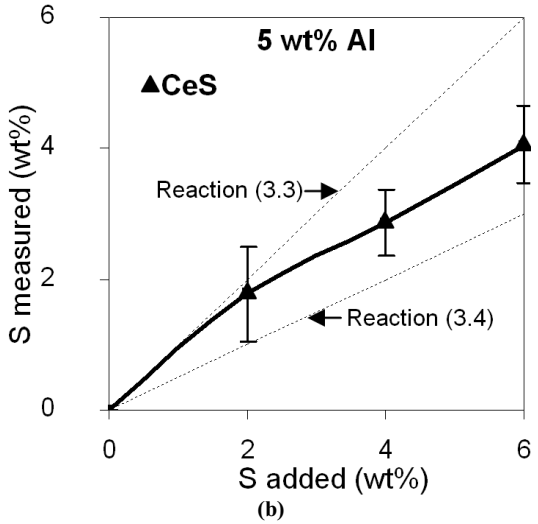

Figure 3.10 Plots showing the measured sulphur content in the samples as a function of the total amount of sulphur added. **(a)** Ce-2 wt% Al base alloy and **(b)** Ce-5 wt% Al base alloy.

It is evident that the measured sulphur content falls between that calculated for 100% yield of FeS_2 and FeS, respectively, as indicated by the dotted lines in the graphs. This essentially means that a significant fraction of the S_2(g) being released by the decomposition of FeS_2 re-dissolves in the melt and combines with cerium to form CeS. Hence, there is an advantage of using FeS_2 compared to FeS as a sulphur source during manufacturing of CeS-based grain refiners because of the opportunities pyrite offers in minimising the iron content for a given target sulphur level.

3.4.2 Phase relations within the Ce-Al-Fe-S system

Currently, there is no phase diagram available for the quaternary Ce-Al-Fe-S system. However, the results from the quantitative phase detection in Sections 3.3.1 and 3.3.2 show that both Ce_3Al, Fe_2Ce and CeS are present in the as-solidified samples. These are intermetallic compounds that are known from the binary phase diagrams[14]. Whereas CeS is a high melting point phase (T_m = 2450 ˚C), Ce_3Al and Fe_2Ce are low melting point compounds (T_m = 655 ˚C and 932, respectively), which together with cerium (T_m = 795 ˚C) constitute the two different eutectic phases detected in the present investigation. None of these eutectic phases have previously been reported in the literature and their melting range and precipitation sequence are therefore not known. However, based on the results from microprobe investigation summarised in Figures 3.3 and 3.4 schematic drawings of the ternary and binary eutectic phases have been made. These are presented in Figure 3.11 and provide further information about their morphology and internal phase distribution.

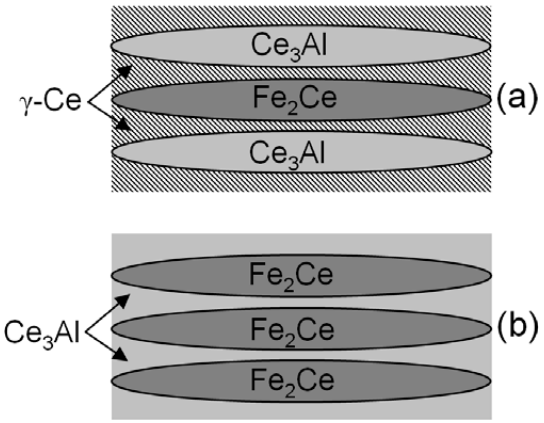

Figure 3.11 Schematic drawings of the two different eutectic phases observed in the as-solidified samples. **(a)** Ternary eutectic phase detected in the Ce-2 wt% Al base alloy and **(b)** binary eutectic phase detected in the Ce-5 wt% Al base alloy.

In addition, a cerium oxysulphide phase is observed in the as-solidified samples, which is the result of an undesirable reaction between CeS and oxygen at elevated temperatures. The WDS point analyses referred to in Section 3.3.2 suggest that its composition is close to Ce_2O_2S. Calculated values for the critical p_{O_2} needed to form (1) Ce_2O_2S, (2) Ce_2O_3 and (3) CeO_2 within the temperature range applicable to these experiments have previously been reported in Part II of the thesis. In Figure 3.12 these p_{O_2} values are superimposed on the measured temperature and oxygen profiles shown previously in Figure 3.1. It follows that Ce_2O_2S is the most stable oxide compound at all relevant temperatures and therefore the most likely phase to form during manufacturing of Ce-based grain refiners for steel.

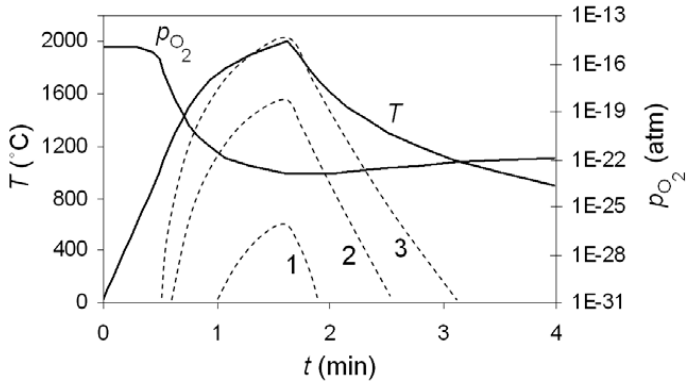

Figure 3.12 Graphical representation of the measured temperature *T* and the partial pressure of oxygen (p_{O_2}) inside the vacuum furnace during a typical rapid heating cycle (i.e. ~1000 ˚C/min). The dotted lines show the corresponding partial pressure of oxygen needed to form (1) Ce_2O_2S, (2) Ce_2O_3 and (3) CeO_2 at the different temperatures (previously calculated in Part II of the thesis).

3.4.3 Upper limit for the sulphur addition using pyrite

The results summarised in Figures 3.10(a) and 3.10(b) show that a sulphur content of about 3.5 wt% can be obtained in the as-solidified samples by adding 6 wt% of sulphur to the melt in the form of FeS_2. At this level of FeS_2 addition, wetting of the tantalum crucible by the melt starts to become a problem, although the solubility limit of sulphur at 2000 ˚C is not exceeded. The wetting is caused by reactions between iron and tantalum, as shown previously in Figure 3.5. The problem becomes much greater at higher iron levels. An example of this is contained in Figure 3.13, which shows a photograph of the tantalum crucible after 8 wt% of sulphur addition using pyrite. In this case the reaction is so vigorous that most of the melt has run over the crucible rim and started to attack the outside walls as well.

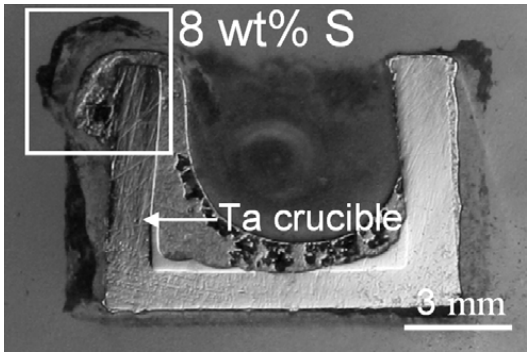

Figure 3.13 Light optical image of the tantalum crucible after a melting experiment with a Ce-5 wt% Al-8 wt% S alloy using pyrite as a sulphur source. The applied heating sequence is shown in Figure 3.1.

Due to this wetting problem sulphur additions based on FeS_2 should be restricted to about 4 wt%. This corresponds to approximately 3 wt% of sulphur retained in the grain refiners, as shown previously in Figures 3.10(a) and 3.10(b), or a volume fraction of CeS close to 0.16.

3.4.4 Stability of the CeS-based grain refiners during long-term storage in air

All samples have been re-examined after 10 months of air exposure. The two base alloys containing no sulphur (No. 1 and 5) show good stability, although the Ce-2 wt% Al sample is prone to surface oxidation. The remaining Ce-2 wt% Al samples containing sulphur (No. 2, 3, and 4), on the other hand, reveal extensive volume expansion and surface cracking. An example of this is shown in Figure 3.14(a) for sample No. 3.

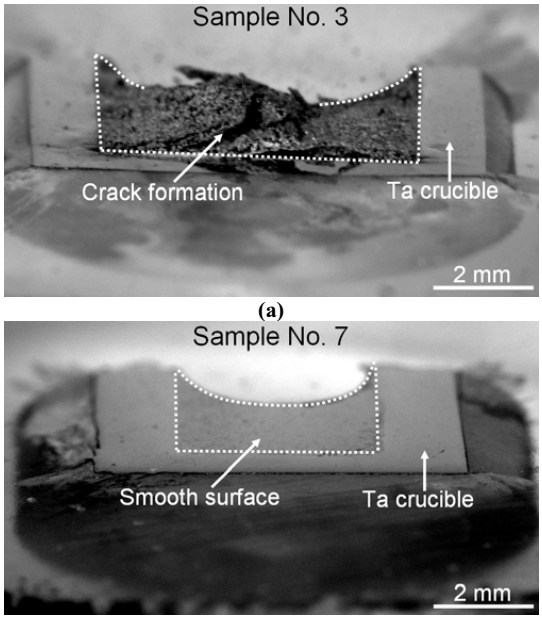

Figure 3.14 Two light optical images **(a)** and **(b)** of samples No. 3 and 7, respectively after 10 months of exposure in air.

Obviously, the CeS compound formation results in a microstructure being vulnerable to internal oxidation, which, in turn, leads to fast deterioration of the γ-Ce phase. Higher aluminium levels are therefore required to stabilise the master alloy in order to ensure that all free cerium is tied-up as Ce_3Al. It follows from Figure 3.14(b) that a 5 wt% aluminium addition will have the necessary stabilising effect at all relevant sulphur levels. This amount of aluminium can be added without affecting the solubility of sulphur, as shown previously in Figure 3.10(b), and

will later be transferred to the liquid steel in an intermetallic form where it will dissolve and act as a deoxidiser.

3.5 Conclusions

The basic conclusions that can be drawn from this investigation are as follows:

1. CeS-based grain refiners can be produced from high-purity charge materials of cerium, aluminium and FeS_2 which are melted and superheated in tantalum crucibles under the shield of cleaned argon. However, to prevent cerium from oxidising due care must be taken to restrict the supply of oxygen from the surrounding gas atmosphere during manufacturing.

2. The phases detected in the as-solidified samples are CeS, Ce_3Al, Fe_2Ce and γ-Ce, along with Ce_2O_2S, which is an undesirable microconstituent in the grain refiners. Both Ce_3Al, Fe_2Ce and γ-Ce are inclined to form low melting eutectics, whereas the stable high-temperature phase CeS constitute a discontinuous dendritic network within the grain refiners.

3. Although pyrite decomposes at 743 ˚C to FeS and $S_2(g)$, the sulphur yield using FeS_2 is significantly higher than that calculated for pure FeS. This is a considerable advantage, because less iron in this way will be charged into the system for a given target composition of sulphur.

4. The melting experiments show that pyrite can be used as a sulphur source up to about 4 wt% sulphur added. At higher levels the Fe-Ta interaction becomes so vigorous that tantalum does no longer act as an inert refractory metal and wetting becomes a major problem. Eventually, this will force the melt to run over the crucible rim and lead to attacks on the outside walls as well.

5. Finally, an evaluation of the stability of grain refiners during long-term storage in air shows that they are prone to volume expansion and surface cracking due to internal oxidation of γ-Ce. In practice, the problem can be overcome by balanced aluminium additions, which will tie-up all free cerium in the form of Ce_3Al.

3.6 References

(1) A. Ohmori, F. Kawabata and K. Amano: Patent EP 1 035 222 A1, (2000).

(2) Ø. Grong and O. S. Klevan: Patent WO 2001/57280, (2001).

(3) P. Grahle, R. Ruch and H. Stiegeler: Patent WO 2005/026396, (2005).

(4) G. Thewlis: *Mater. Sci. Technol.*, **22**(2006), 153.

(5) W. G. Wilson, D. A. R. Kay and A. Vahed: *JOM*, **26**(1974), 14.

(6) W. K. Lu and A. McLean: *Ironmaking Steelmaking*, **1**(1974), 228.

(7) S. S. Babu: *Current Opinion in Solid State & Materials Science*, **8**(2004), 267.

(8) D. J. Abson and R. J. Pargeter: *Int. Met. Rev.*, **31**(1986), 141.

(9) Ø. Grong and D. K. Matlock: *Int. Met. Rev.*, **31**(1986), 27.

(10) A. R. Mills, G. Thewlis and J. A. Whiteman: *Mater. Sci. Technol.*, **3**(1987), 1051.

(11) G. Thewlis, W. T. Chao, P. L. Harrison and A. J. Rose: *Mater. Sci. Technol.*, **24**(2008), 771.

(12) Ø. Grong, L. Kolbeinsen, C. van der Eijk and G. Tranell: *ISIJ Int.*, **46**(2006), 824.

(13) T. Koseki and G. Thewlis: *Mater. Sci. Technol.*, **21**(2005), 867.

(14) T. B. Massalski: Binary alloy phase diagrams, Vol.1, American Society for Metals, Ohio, (1986), 101, 709, 737, 1103.

(15) J. Loriers: *Compt. rend.*, **229**(1949), 547.

(16) E. E. Underwood: Quantitative Stereology, Addison-Wesley Publishing Company, Menlo Park, California, (1970), 5.

Part IV: Conditions for CeS formation during manufacturing of Ce-S-Al based grain refiners for steels

4.1 Introduction

The harmful effects of inclusions on steel properties arise from their ability to act as initiation sites for micro-voids and cleavage cracks during service. Hence, the use of clean steels is normally considered to be an advantage from a toughness point of view[1,2]. On the other hand, it is now widely accepted that non-metallic inclusions also display some positive attributes by virtue of their ability promote grain refinement during solidification and/or in the solid state by a process of heterogeneous nucleation[3,4]. Such particles are sufficiently small to be harmless from a toughness point of view[5,6], but at the same time large enough to act as potent nucleation sites during phase transformation[7-9]. For example, the phenomenon of intragranular nucleation of acicular ferrite at oxides and sulphides is well known from low-alloy steel weld metals, where the characteristic high number density of such inclusions results in the development of a fine-grained microstructure within the as-deposited material[10-13]. Later, the concept has been transferred to wrought steels products, leading to the introduction of the titanium deoxidised steels in the early nineties[14-16]. Currently, a wide variety of different steels in which non-metallic inclusions are used to control the microstructure evolution in the solid state have been patented, both in Europe and Japan[17-19]. This reflects an increasing interest among the international steel manufacturers to exploit the possibility offered by the technology to produce new low-cost steel grades with unique transformation characteristics on a commercial basis.

Several systems with the potential of being used as grain refiners for steel have been studied over the last ten years. One of the most promising ones is the cerium-sulphur system[20]. Cerium has a strong affinity to sulphur and will, almost always, form a compound with sulphur when both elements are present in molten steel[21,22]. A fine distribution of CeS particles in the steel matrix during the austenite to ferrite transformation can shift the nucleation process from the austenite grain boundaries to sites located intragranularly[23]. Unfortunately, modern steelmaking involving continuous casting does not allow large amounts of ferroalloys to be added late in the process due to the practical problems this will cause in terms of a severe temperature drop and incomplete alloy dissolution and mixing in the liquid. Therefore, in order to maintain a good nucleation potential, the master alloy needs to be highly concentrated and contain between 5 and 10 wt% S[24]. Cerium is in this context interesting, since it can dissolve large amounts of sulphur in the liquid state[25]. Thus, by fully exploiting the potential of cerium as a sulphur carrier, effective grain refiners can also be produced for continuously cast steels containing a high number density of embedded CeS particles.

It was demonstrated in Part III of the thesis that CeS-based grain refiners can be produced from high-purity charge materials of Ce, Al and FeS_2 (pyrite), which are melted and superheated to about 2000 ^oC in tantalum crucibles under the shield of cleaned argon. However, in order to prevent cerium from oxidising due care must be taken to restrict the supply of oxygen from the surrounding gas atmosphere during manufacturing. The phases observed within the as-solidified samples are CeS, Ce_3Al, Fe_2Ce and Ce, along with Ce_2O_2S, which is an undesirable microconstituent in the grain refiners. Both Ce_3Al, Fe_2Ce and Ce are inclined to form low melting eutectics, whereas the stable high-temperature phase CeS constitutes a discontinuous dendritic network within the grain refiners. The indications are that pyrite can be used as a sulphur source up to about 4 wt% S added, corresponding to about 3 wt% of retained sulphur in the grain refiners. At higher levels the Fe-Ta interaction becomes so vigorous that tantalum is no longer an inert refractory metal and wetting becomes a major problem. Eventually, this will force the melt to run over the crucible rim and also lead to attacks on the outside walls, as shown in Part III of the thesis.

In Part IV of this thesis, attempts will be made to produce the CeS-based grain refiners without adding iron by using Ce_2S_3 as the sulphur source. According to the binary Ce-S phase diagram the solubility of sulphur in liquid cerium at 2000 ^oC should be of the order of 10 wt%[25], which is formidable compared to that inferred from other potential systems like Fe-Mn-S and Dy-S but more similar to that of La-S[25,26]. Although between 2 and 5 wt% of aluminium is needed to improve the long-term stability of the grain refiners in contact with air by promoting the Ce_3Al compound formation, such small aluminium additions would not be expected to impose large restrictions on the sulphur solubility, as previously shown in Part III of the thesis. Still, this needs to be verified experimentally by carrying out a series of exploratory measurements of the phase relations within the ternary Ce-S-Al system. The results will then be compared with those obtained employing pyrite as a sulphur source and eventually used to reassess the Ce-S phase diagram, which is believed to provide misleading information about the sulphur solubility in liquid cerium.

4.2 Experimental

Figure 4.1 shows a sketch of the cerium-rich corner of the ternary Ce-S-Al phase diagram and the composition range examined in the present investigation.

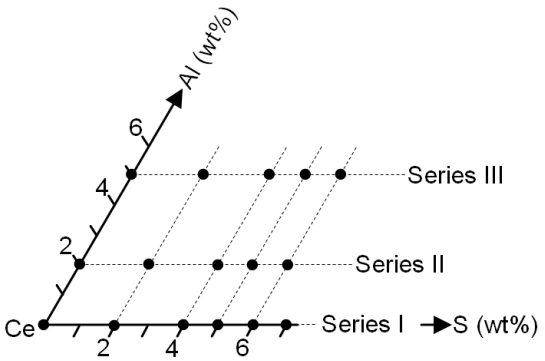

Figure 4.1 Target chemical compositions of the 16 different charge mixtures prepared for the melting trials.

Specifically, the following three different series are included in the experimental programme, i.e. Series I with no Al additions and 0, 2, 4, 5, 6 and 7 wt% S added, Series II with 2 wt% Al additions and 0, 2, 4, 5 and 6 wt% S added and Series III with 5 wt% Al additions and 0, 2, 4, 5 and 6 wt% S added.

4.2.1 Charge materials and sample preparation procedures

The charge mixtures were prepared from high purity raw materials, i.e. γ-Ce, Ce_2S_3 and Al, all with a purity greater than 99.9%. These were obtained from different commercial manufacturers. To prevent the materials from oxidising, an argon-filled glove box with oxygen and humidity levels << 0.1 ppm was used for storage, weighing and subsequent charging of the materials into the small tantalum crucibles used in the melting trials. In the present laboratory experiments the typical sample weight is about 0.8 gram, which can be measured with an accuracy of about ± 0.0001 gram.

After weighing the charged tantalum crucibles were transported to the vacuum furnace inside an argon-filled container.

4.2.2 Melting experiments

The vacuum furnace, which originally is designed for in-situ wetting angle measurements, is equipped with a sample holder capable of heating small tantalum crucibles with an outer diameter of 10 mm. Figure 4.2 shows a drawing of the main parts of the furnace.

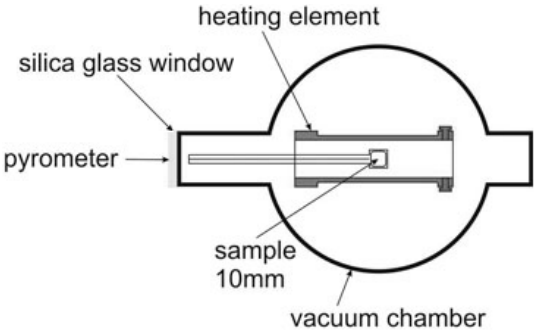

Figure 4.2 Schematic illustration of the vacuum furnace used in the melting experiments.

The heating element is made of graphite, as are all of the other heated parts of the furnace. A calibrated two-colour pyrometer, with an operating temperature range from 900-2400 ^{o}C, continuously measures the temperature of the crucible. To protect the sample form oxidising, the vacuum furnace is constantly flushed with high purity argon. This, together with the oxygen scavenging effect provided by the graphite heating element at temperatures above 1800 ^{o}C, is sufficient to prevent cerium from oxidising during the melting experiments. Further details are given in Part II of the thesis.

Figure 4.3 shows a record of the actual crucible temperature as a function of time during a typical rapid heating cycle at ~1000 ^{o}C/min.

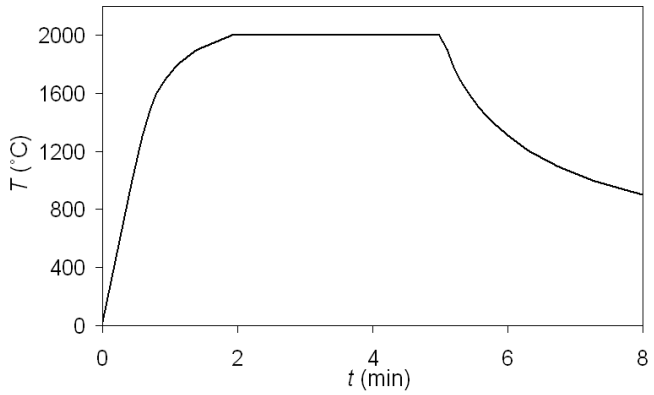

Figure 4.3 Graphical representation of the measured crucible temperature *T* as a function of time during a typical rapid heating cycle (i.e. ~1000 ^{o}C/min).

In these small-scale laboratory experiments it is essential that the heating rate is high enough to kinetically suppress the oxygen absorption from the shielding gas before the graphite takes control of the oxygen level at about 1800 ^{o}C. When the target superheat temperature of 2000 ^{o}C

is reached the samples are held at that temperature for 3 minutes to allow the Ce_2S_3 to dissolve into the melt. This holding time is sufficient to reach sulphur saturation at 2000 ^oC because supplementary test results (not reported here) show that there is no real difference in neither the Ce_2S_3 dissolution behaviour nor the subsequent CeS compound formation during cooling between samples held at 3 and 6 minutes.

4.2.3 Optical and electron microscopy

Standard metallographic techniques were employed to prepare cross section samples for microstructure characterisation. Because γ-Ce corrodes vigorously in water, wet grinding was carried out using an alcohol based lubricant. In the light microscope the microstructure was readily revealed without etching. The optical examination was preformed using a conventional Zeiss reflecting light microscope. In addition, phase characterisation was done employing backscatter electron (BSE) imaging and wavelength dispersive X-ray spectrometry (WDS). These investigations were carried out in a JEOL JXA-8500F electron microprobe, using an acceleration voltage of 15 keV and a probe current of 30 nA.

4.2.4 Volume fraction measurements

Standard point counting techniques were used to measure the volume fraction of the different constituent phases present in each sample[27]. This was done by taking 10 optical micrographs at a magnification of 200X, which subsequently were provided with 10x20 square grids to ease the point counting. The microstructure data were recorded and processed using the Visual Basic point count programme CPCe V3.5[28]. A total of 2000 points was counted for each sample, from which the mean values and the standard deviation of the means were calculated. The measured volume fractions of the different constituent phases (cp) were then compared with the calculated ones, based on the following equation:

$$f_{cp} = \frac{m_{cp}/\rho_{cp}}{m_a/\rho_a} \tag{4.1}$$

Where m_a is the total weight of the alloy and m_{cp} is the total mass of a given phase in the alloy, assuming 100% yield of the charged elements and the formation of stoichiometric compounds. The symbols ρ_a and ρ_{cp} in Eq. (4.1) represent the corresponding densities of the alloy and the constituent phase being considered in the calculations.

In order to ensure the highest possible confidence in the calculations, measured values for the density of the alloys ρ_a should be used. Archimedes principle of buoyancy was therefore adopted to measure the density of samples from the three different series included in the investigation. By extrapolating the experimental data up to 7 wt% S, separate density plots for Series I, II and III were constructed, as shown in Figure 4.4.

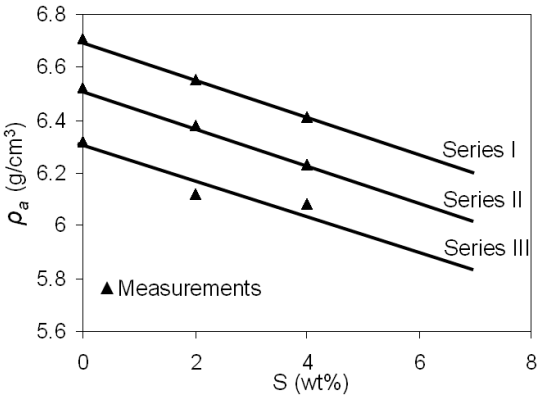

Figure 4.4 Plots showing the measured density of samples from Series I, II and III, respectively as a function of the added sulphur content.

4.3 Results

4.3.1 Phase characterisation

In the following, the main results from the microstructure and phase characterisation will be presented. Note that the microstructure data reported below refer to the 5 wt% S samples from Series I, II and III, which contain a representative selection of the phases being present in the alloys mentioned in Figure 4.1.

4.3.1.1 Series I

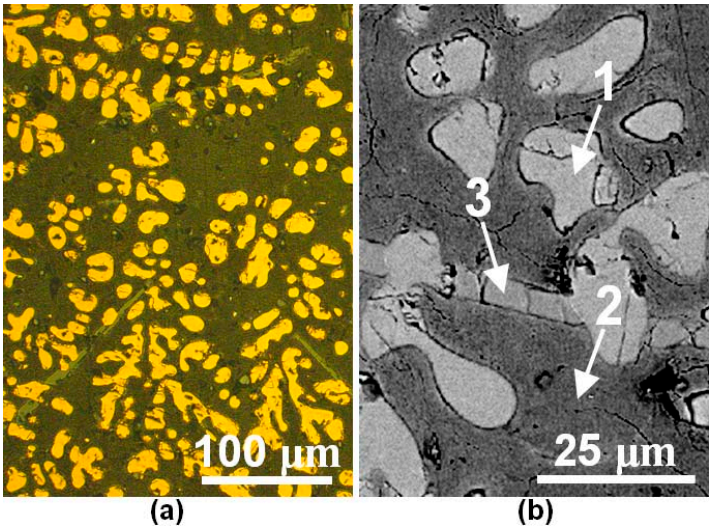

Figure 4.5 (a) Optical and **(b)** BSE micrographs of the 5 wt% S sample from Series I at low and high magnification, respectively. The arrows indicate the position of the three point analyses reported in Table 4.1.

Figure 4.5(a) and 4.5(b) show one optical and one BSE image, respectively at low and high magnification of the 5 wt% S sample from Series I. The three WDS point analyses shown in Table 4.1 were carried out at the surface positions indicated by arrows in the electron micrograph.

Table 4.1 Point analyses of various phases detected in the 5 wt% S sample from Series I. The numbers are given in at%.

No.	Al	O	S	Ta	Ce
1	0.0	3.4	46.1	0.0	50.5
2	0.2	62.9	0.1	0.0	36.8
3	0.0	40.1	17.5	0.0	42.4

The ratio between Ce and S found in phase No. 1 points toward CeS. In this sample all CeS is present in the form of a discontinuous dendritic network within the matrix, as shown by the optical micrograph in Figure 4.5(a). Moreover, it follows that the matrix, corresponding to phase No. 2 in Table 4.1, consists mainly of cerium and oxygen. Because this area shows signs of surface corrosion, it is reasonable to assume that the γ-Ce has been oxidised either during or immediately after the metallographic preparation. Hence, phase No. 2 is most likely γ-Ce with a surface layer of Ce_2O_3 or CeO_2. In addition, needle-shaped particles can also be observed within the microstructure. As judged from the point analysis of phase No. 3 in Table 4.1, this phase is

probably Ce_2O_2S, which is the most stable cerium oxysulphide and therefore will inevitably form in the presence of oxygen, as previously shown in Part II of the thesis.

4.3.1.2 Series II

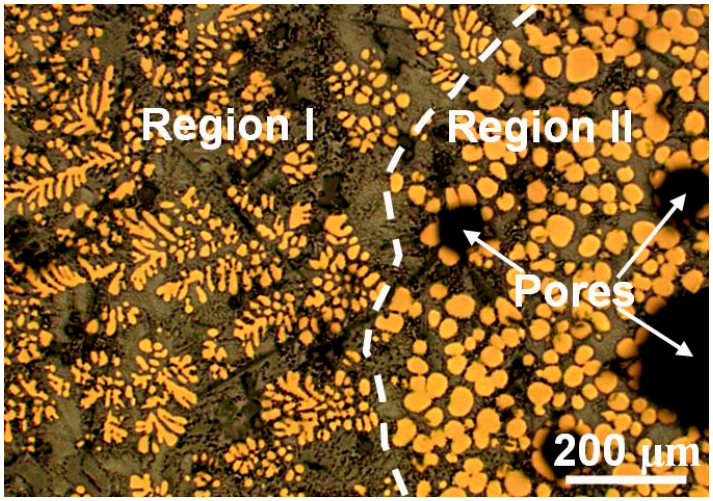

Figure 4.6 Optical micrograph of the 5 wt% S sample from Series II at low magnification. The dotted line indicates the boundary between Region I and II, which contain different forms of CeS.

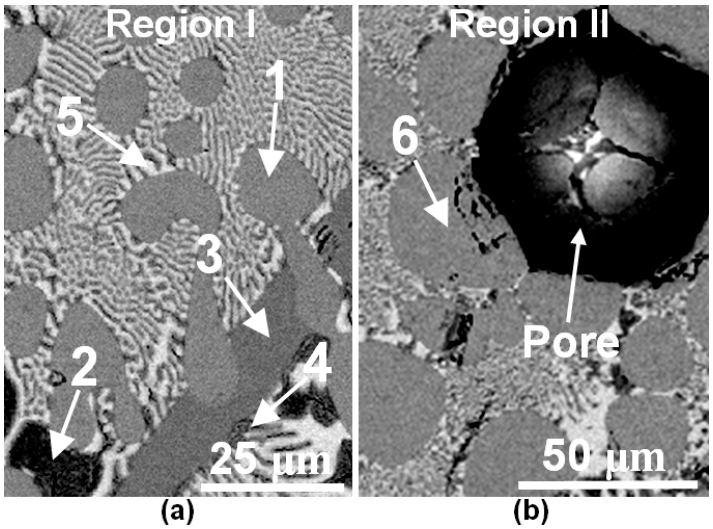

Figure 4.7 BSE images of **(a)** Region I and **(b)** Region II showing close-ups of the microstructures displayed in Figure 4.6. The arrows indicate the position of the six point analyses reported in Table 4.2.

Figure 4.6 shows an optical micrograph of the 5 wt% S sample from Series II at low magnification. Two distinct regions can be detected in this image, i.e. Region I containing CeS

dendrites and Region II containing CeS particulates, which is similar to that observed in Series I at 6 and 7 wt% S added (not shown here). Close-ups of Region I and II are shown by the BSE images in Figure 4.7(a) and 4.7(b), respectively. Note that the arrows in the electron micrographs indicate the position of the six point analyses reported in Table 4.2.

Table 4.2 Point analyses of various phases detected in the 5 wt% S sample from Series II. The numbers are given in at%.

No.	Al	O	S	Ta	Ce
1	0.0	1.9	47.2	0.0	50.9
2	0.2	64.5	0.1	0.0	35.2
3	0.3	62.0	0.2	0.0	37.5
4	22.1	4.5	0.1	0.0	73.3
5	0.1	35.7	20.7	0.1	43.4
6	0.0	1.4	47.7	0.0	50.9

The point analyses No. 1 through 5 refer to Region I in Figure 4.7(a). The phases observed in position 1 and 2 are CeS and γ-Ce (with a surface layer of CeO_2/Ce_2O_3), respectively. In Region I the CeS forms a discontinuous dendritic network similar to that observed for Series I in Figure 4.5. The γ-Ce, on the other hand, is no longer present as an isolated phase, but is part of a lamella-shaped eutectic. It follows from the point analyses of position 3 and 4 in Figure 4.7(a) that the ratio between the constituent elements reported in Table 4.2 corresponds to CeO_2/Ce_2O_3 and Ce_3Al. However, as pointed out in Section 4.3.1.1, the cerium-oxide is probably γ-Ce which has been oxidised during the metallographic preparation. Hence, the eutectic phase consists most likely of γ-Ce and Ce_3Al. In addition, the point analysis carried out in position 5 shows that needle-shaped Ce_2O_2S particles also are present within the sample because of reactions with dissolved oxygen being picked-up from the shielding gas.

Moreover, it is evident from Table 4.2 that Region II also contains CeS as shown by the point analysis of position 6 in Figure 4.7(b). Their characteristic particulate morphology suggests that they are of a different physical origin compared to the CeS dendrites. In-between, a eutectic phase is observed, which probably is the same as the one detected within Region I. This follows from a comparison of the two BSE images in Figure 4.7(a) and 4.7(b), respectively. In addition, a number of large pores can be seen within the microstructure, which are either gaseous or shrinkage pores. Because these always appear together with the CeS particulates, it is reasonable to assume that they are associated with the conversion of Ce_2S_3 to CeS in regions of the melt already saturated with respect to sulphur (to be discussed later).

4.3.1.3 Series III

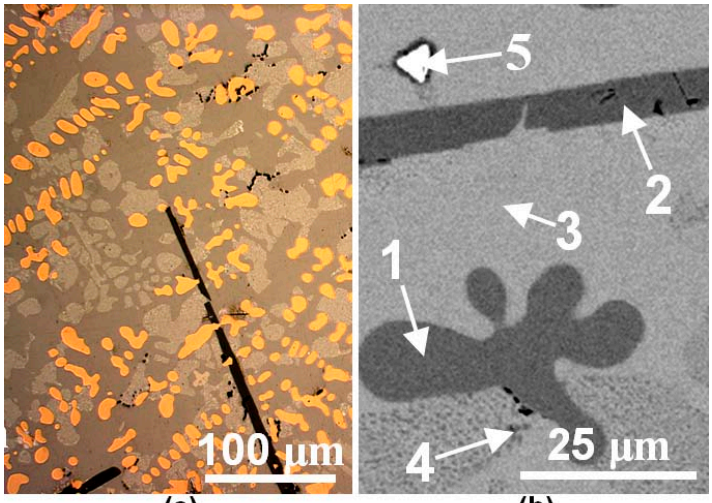

Figure 4.8 (a) Optical and **(b)** BSE micrographs of the 5 wt% S sample from Series III at low and high magnification, respectively. The arrows indicate the position of the five point analyses reported in Table 4.3.

Figure 4.8(a) and 4.8(b) show one optical and one BSE image, respectively at low and high magnification of the 5 wt% S sample from Series III. In this case the arrows in the latter micrograph indicate the position of the five point analyses reported in Table 4.3.

Table 4.3 Point analyses of various phases detected in the 5 wt% S sample from Series III. The numbers are given in at%.

No.	Al	O	S	Ta	Ce
1	0.2	1.3	47.5	0.1	50.9
2	23.1	3.7	0.1	0.0	73.1
3	45.4	2.1	0.1	0.0	52.4
4	22.8	3.8	0.1	0.0	73.3
5	2.1	4.3	0.2	90.9	2.5
6	0.0	1.6	48.3	0.0	50.1
7	0.0	1.2	55.7	0.0	43.1

It follows from Table 4.3 that the two phases observed in position 1 and 2 are CeS and Ce_3Al. Adjacent to these, the eutectic phase is located, which according to the point analyses of position 3 and 4 consists of CeAl and Ce_3Al, respectively. Furthermore, the phase observed in position 5 is tantalum. This tantalum stems from reactions with the crucible, which at 2000 °C has a limited solubility in liquid cerium[25].

In addition to the CeS dendrites observed in Figure 4.8(a) the 5 wt% S sample from Series III also contained CeS particulates analogous to that documented for Series II in Figure 4.6. For an addition of 6 wt% S the CeS particulate formation is even more pronounced, as shown in Figure 4.9(a). At the same time remnants of an intermediate reaction product are present at the interface between the pores and the surrounding CeS particulates, as evidenced by the electron micrograph in Figure 4.9(b). It follows from Table 4.3 that the phase detected in position 7 adjacent to the CeS in position 6 is Ce_3S_4. This suggests that the conversion of Ce_2S_3 to CeS occurs in steps via the intermediate Ce_3S_4 phase, which results in $S_2(g)$ rejection and subsequently pore formation along with CeS particulate precipitation in regions of the melt already saturated with respect to sulphur.

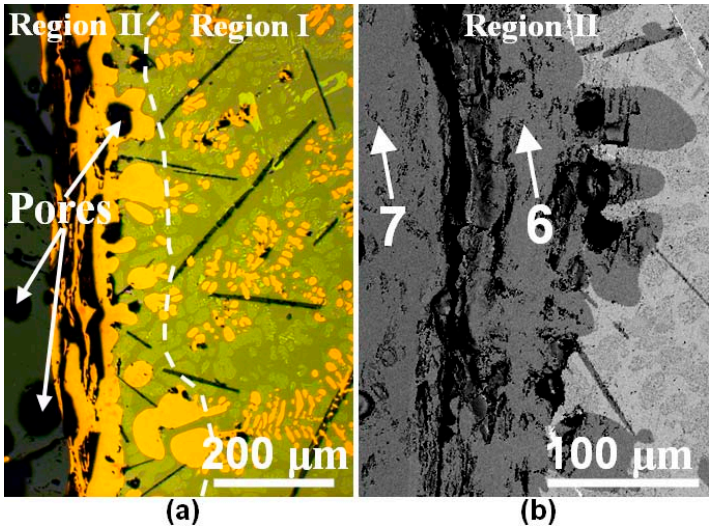

Figure 4.9 (a) Optical and **(b)** BSE micrographs of the 6 wt% S sample from Series III at low and high magnification, respectively. The dotted line indicates the boundary between Region I and II (defined previously in Figure 4.6), whereas the arrows indicate the position of the two point analyses reported in Table 4.3.

4.3.2 Quantitative volume fraction measurements

In Table 4.4, the results from the quantitative metallographic examination of the various phases detected in the samples from Series I, II and III are summarised. Included is also the standard deviation in the measurements, which provides a good indication of the samples homogeneity in each case. Note that the volume fraction measurements have only been carried out within Region I. The CeS particulates are excluded from these analyses, as they form in regions of the

melt already saturated with respect to sulphur, and are thus of a different physical origin compared to the CeS dendrites.

Table 4.4 Summary of the results from the quantitative volume fraction measurements of the various phases detected in the samples from Series I, II and III.

Series No.	Phases detected	wt% S added					
		0	2	4	5	6	7
I	CeS	0.00	0.12±0.04	0.23±0.02	0.30±0.03	0.34±0.04	0.35±0.02
	γ-Ce	0.99±0.01	0.85±0.05	0.73±0.04	0.67±0.04	0.61±0.05	0.56±0.05
	Ce_2O_2S	0.01±0.01	0.02±0.01	0.03±0.02	0.03±0.01	0.04±0.02	0.08±0.02
	Ta	0.00	0.01±0.01	0.01±0.00	0.00	0.01±0.00	0.01±0.01
II	CeS	0.00	0.10±0.02	0.23±0.03	0.24±0.04	0.24±0.03	-
	γ-Ce	0.63±0.03	0.52±0.05	0.41±0.05	0.39±0.03	0.37±0.02	-
	Ce_3Al	0.36±0.03	0.36±0.04	0.33±0.02	0.34 0.03	0.35±0.05	-
	Ce_2O_2S	0.01±0.01	0.02±0.01	0.03±0.02	0.03±0.01	0.04±0.02	-
	Ta	0.00	0.00	0.00	0.00	0.00	-
III	CeS	0.00	0.11±0.02	0.22 0.03	0.18±0.05	0.18±0.03	-
	γ-Ce	0.15±0.02	0.08±0.02	0.00	0.00	0.00	-
	Ce_3Al	0.84±0.02	0.79±0.03	0.64±0.05	0.62±0.02	0.58±0.03	-
	CeAl	0.00	0.00	0.11±0.03	0.17±0.03	0.20±0.03	-
	Ce_2O_2S	0.01±0.01	0.02±0.01	0.03±0.01	0.03±1.64	0.03±0.01	-
	Ta	0.00	0.00	0.00	0.00	0.01±0.01	-

Figure 4.10(a) and 4.10(b) show graphical representations of the measured volume fractions of CeS, γ-Ce, Ce_3Al and CeAl in the samples from Series I, II and III as a function of the added sulphur content. The dotted lines in Figure 4.10(a) represent the calculated volume fractions of CeS assuming 100% sulphur yield, according to Eq. (4.1).

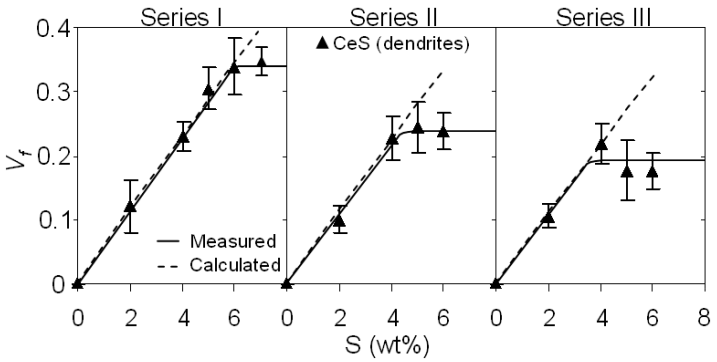

(a)

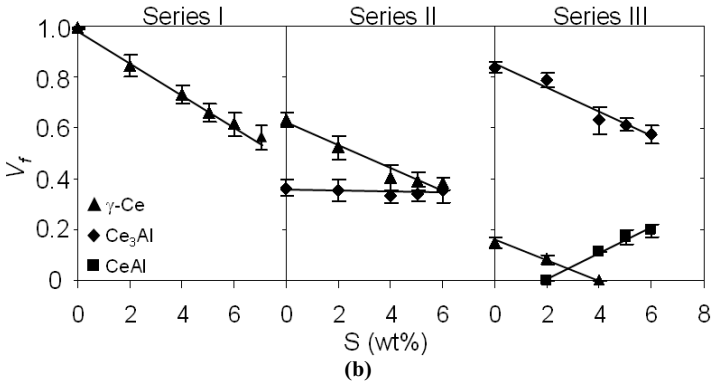

Figure 4.10 Graphical representations of the measured volume fractions of **(a)** CeS and **(b)** γ-Ce, Ce_3Al and CeAl in the samples from Series I, II, and III as a function of the added sulphur content. The error bars in the graphs represent the standard deviation of the measurements, whereas the dotted lines are the calculated volume fractions of CeS based on Eq. (4.1).

A closer inspection of the trend lines in Figure 4.10(a) shows that the use of Ce_2S_3 as a sulphur source implies a yield of 100% up to the point where saturation is reached. In the case of the binary Ce-S system (Series I) sulphur saturation at 2000 ^oC is reached at about 6 wt% added, corresponding to a volume fraction of CeS of approximately 0.34 in the as-solidified sample. At this point the CeS particulates start to appear within the microstructure, which suggests that the two phase field region is entered. When aluminium is added the overall picture is similar. Still, the aluminium additions have a marked effect on the sulphur solubility, which at 5 wt% Al is reduced to about 3.3 wt%, corresponding to a volume fraction of CeS of 0.19.

Because sulphur ties-up an equivalent (stoichiometric) amount of cerium, the content of free γ-Ce decreases when Ce_2S_3 is added to the melt, as shown in Figure 4.10(b). At high aluminium levels this reduction in the γ-Ce content is also accompanied by a change in the phase balance between Ce_3Al and CeAl, leading to the displacive behaviour observed in the graph for Series III.

4.4 Discussion

In the following, the conditions for CeS formation and the subsequent precipitation reactions occurring during cooling following the Ce_2S_3 and aluminium additions to liquid cerium will be discussed in more detail.

4.4.1 Phase relations within Region I

Within Region I the results from the quantitative phase detection show that both CeS, Ce_3Al and CeAl are present in the as-solidified samples. These are intermetallic compounds that are known

from the binary phase diagrams[25]. Figure 4.11 shows a sketch of the cerium-rich corner of the ternary Ce-S-Al phase diagram, in which the tie-lines connecting the observed coexisting phases within Series I, II and III are included.

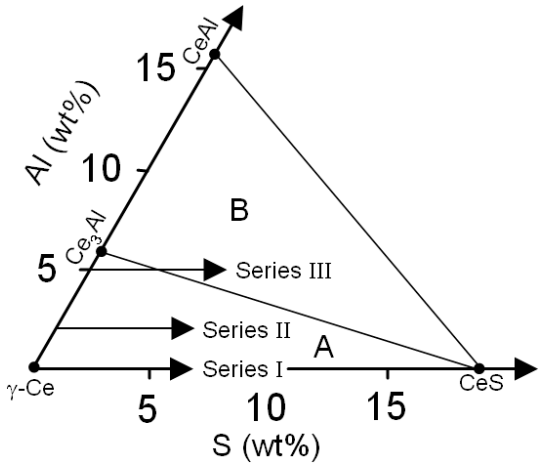

Figure 4.11 Sketch of the cerium-rich corner of the ternary Ce-S-Al phase diagram where the tie-lines connecting the observed phases within Series I, II and III are included.

It follows from Figure 4.11 that the three coexisting phases within phase-field A are γ-Ce, Ce_3Al and CeS, where the former ones also constitute the two eutectic phases shown schematically in Figure 4.12(a) and 4.12(b) being observed at 2 and 5 wt% Al, respectively. The third eutectic phase displayed in Figure 4.12(c) forms when all free γ-Ce in Series III is tied-up with sulphur and aluminium. This occurs when the sulphur level exceeds 4 wt% and the composition shifts to phase-field B in Figure 4.11, yielding the three coexisting phases Ce_3Al, CeAl and CeS.

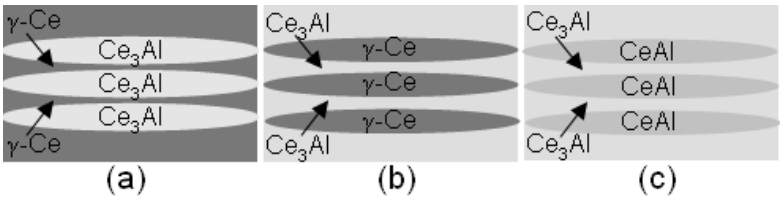

Figure 4.12 Schematic drawings showing the three different eutectic phases observed in the samples from Series II and Series III. The eutectics refer to phase-fields A and B in Figure 4.11.

Beside the quantitative phase characterisation reported in the present investigation, no information is available in the scientific literature about the phase relations within the ternary

Ce-S-Al system. This prevents a more in-depth analysis of the precipitation sequence and the thermodynamic stability of the three eutectic phases visualised in Figure 4.12.

4.4.2 Phase relations within Region II

Region II refers to parts of the melt already being saturated with respect to sulphur. Therefore, the remnants of the phases detected in Figure 4.9 conceal details of the dissolution kinetics of Ce_2S_3 within the two-phase region "liq + CeS". Figure 4.13 shows a sketch of the binary Ce-S phase diagram, which is a useful model system to unravel the reaction sequence.

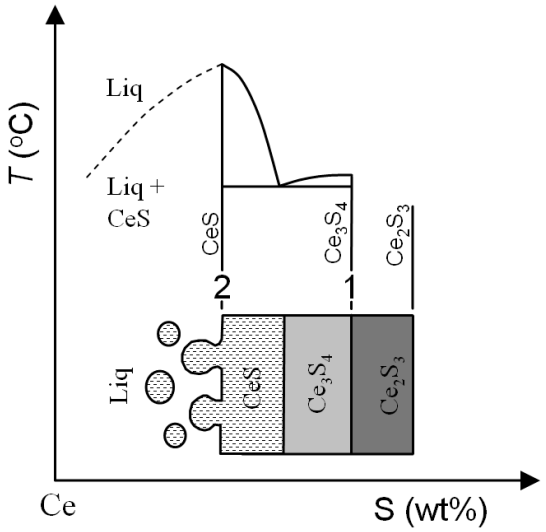

Figure 4.13 Sketch of the binary Ce-S phase diagram showing the sequence of reactions occurring during conversion of Ce_2S_3 to CeS within the two-phase region "liq + CeS" (i.e. Region II in Figure 4.9).

It follows that Step 1 involves conversion of Ce_2S_3 to Ce_3S_4, according to the reaction:

$$3Ce_2S_3 = 2Ce_3S_4 + 1/2S_2(g) \qquad (4.2)$$

This conversion gives rise to the release of $S_2(g)$ bubbles and subsequent pore formation within the interior of the as-solidified samples, as shown previously in Figures 4.6 and 4.7. In addition, the in-situ photograph of the tantalum crucible provided in Figure 4.14 suggests that some of the gas bubbles also escape from the surface during the melting experiments. This is another indication that sulphur saturation is reached at 2000 °C and explains why the curves in Figure 4.10(a), representing the sulphur yield, suddenly flatten out when the solubility limit is reached at the different aluminium levels.

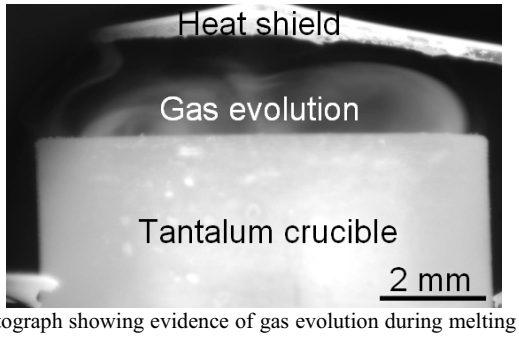

Figure 4.14 In-situ photograph showing evidence of gas evolution during melting of the 5 wt% S sample from Series III.

Moreover, Step 2 involves conversion of Ce_3S_4 to CeS, most probably according to the reaction:

$$Ce_3S_4 + Ce = 4CeS \tag{4.3}$$

Because Eq. (4.3) implies that cerium must diffuse through the CeS reaction layer in order to reach the CeS/Ce_3S_4 interface, a high conversion rate can only be maintained throughout the process if the CeS particulates are continuously rejected at the liq/CeS interface, as indicated in Figure 4.13. This leads to the characteristic "two-phase region" microstructures shown previously in Figures 4.6 and 4.9.

4.4.3 Solubility of sulphur in liquid Ce and Ce-Al melts

The results from the CeS volume fraction measurements in Figure 4.10(a) provide a good indication of the sulphur solubility in liquid cerium and Ce-Al melts at 2000 ^{o}C. At this temperature pure cerium can dissolve as much as 6 wt% of sulphur, which is reduced to 4.1 wt% at 2 wt% Al and further to 3.3 wt% at 5 wt% Al. Although the measured sulphur solubility is formidable, it is considerably lower than that inferred from the binary Ce-S phase diagram, which suggests that the solubility should be close to 10 wt% at 2000 ^{o}C[25)].

In Figure 4.15 the new liquidus line representing the sulphur solubility within the Ce-S system is indicated, based on the results obtained in the present investigation. Two other points on the curve are also provided, i.e. at 1800 and 1500 ^{o}C. These results have been obtained from a series of up-scaled melting experiments carried out in an induction furnace filled with cleaned argon and are sufficiently accurate to be incorporated in the present data collection. Further details about these experiments are provided in Part V of the thesis.

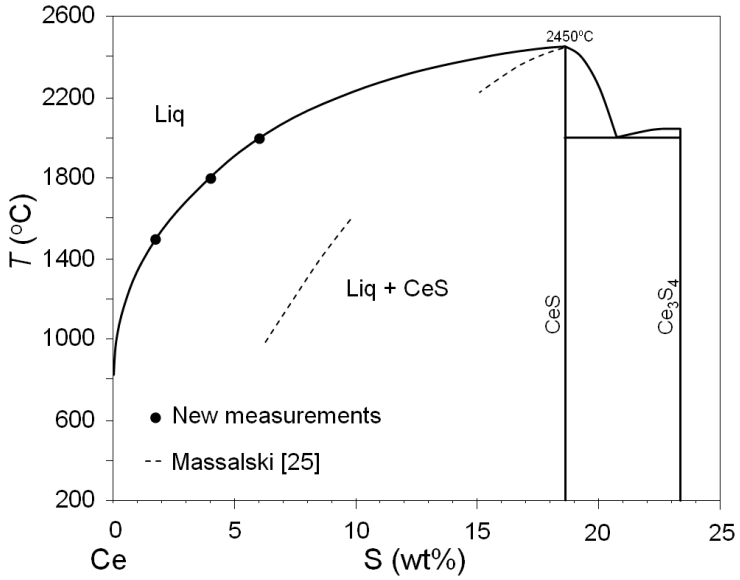

Figure 4.15 The revised Ce-S phase diagram containing new and more reliable information about the solubility of sulphur in liquid cerium at elevated temperatures.

As expected, the sulphur solubility is seen to decrease with decreasing temperatures, reaching a value of about 1.8 wt% at 1500 °C. This new liquidus line is believed to be more accurate than the previous one quoted by Massalski[25]. At the same time it is consistent with what one would expect from a comparison with the La-S phase diagram[25], which appears to be more firmly established and is thus a good benchmark for the present measurements.

4.4.4 Long-term stability of the grain refiners during storage in air

It has previously been shown in Part III of the thesis that aluminium additions are required to prevent the grain refiners from disintegrating during long-term storage in air when pyrite (FeS_2) is used as a sulphur source. By replacing FeS_2 with Ce_2S_3 the problem with internal oxidation of free cerium is largely eliminated, as evidenced by the optical photographs in Figure 4.16(a) and 4.16(b), suggesting that the observed disintegration is mainly associated with the presence of the Fe_2Ce phase in the grain refiners.

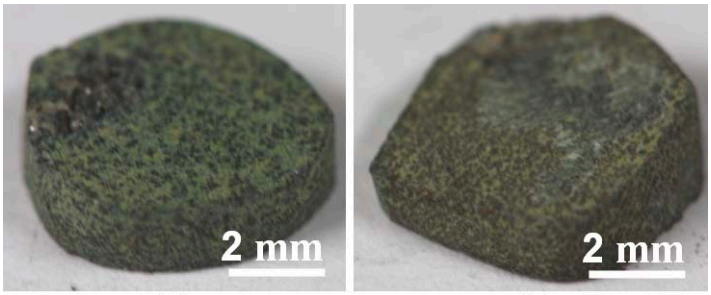

Figure 4.16 Two light optical images of samples from Series I after 8 months of air exposure. **(a)** 2 wt% S added and **(b)** 4 wt% S added.

Therefore, alloying with aluminium is no longer a crucial issue and should thus be restricted if the highest possible sulphur solubility is desired in the liquid state. In this way, the benchmark previously set for the sulphur content in the grain refiners can be met[24].

4.5 Conclusions

The basic conclusions which can be drawn from this investigation are as follows:

1. CeS-based grain refiners can be produced from high-purity charge materials of cerium, aluminium and Ce_2S_3, which are melted and superheated in tantalum crucibles under a shield of cleaned argon.

2. During melting the dissolution of Ce_2S_3 occurs in steps via the intermediate Ce_3S_4 phase, which results in $S_2(g)$ evolution and subsequently CeS particulate formation. In spite of this decomposition reaction, the observed sulphur yield is close to 100% up to the point where saturation is reached, meaning that both components are fully absorbed within the liquid cerium melt.

3. The phases detected in the as-solidified samples are CeS, Ce_3Al, CeAl and γ-Ce, along with Ce_2O_2S, the latter one being an undesirable microconstituent in the grain refiners. Both Ce_3Al, CeAl and γ-Ce are inclined to form low melting point eutectics, whereas the stable high-temperature phase CeS constitutes a discontinuous dendritic network within the grain refiners.

4. The results show that pure cerium can dissolve up to 6 wt% of sulphur at 2000 ^{o}C, which is reduced to about 1.8 wt% at about 1500 ^{o}C. This solubility is considerably

lower than that inferred from the binary Ce-S phase diagram, which suggests that it should be close to 10 wt% at 2000 ^{o}C.

5. Based on the results obtained in the present investigation the binary Ce-S phase diagram has been revised to comply with the new solubility data. The liquidus line being constructed is believed to be more accurate than the one previously reported in the literature. At the same time it is consistent with what one would expect from a comparison with the La-S system, which appears to be more firmly established and is thus a good benchmark for the present measurements.

6. Moreover, it is confirmed that alloying with aluminium has a clear negative effect on the solubility of sulphur in liquid cerium. Thus, at 2000 ^{o}C it drops from initially 6 wt% to 4.1 wt% at 2 wt% Al added and further to 3.3 wt% at 5 wt% Al added.

7. In addition, when Ce_2S_3 is used as the sulphur source in replacement of pyrite (FeS_2) the previously experienced problem with internal oxidation of free cerium in the grain refiners is largely eliminated. Therefore, alloying with aluminium is no longer crucial and should thus be restricted if the highest possible sulphur solubility is desired in the liquid state.

4.6 References

(1) H. V. Atkinson and G. Shi: *Prog. Mater. Sci.*, **48**(2003), 457.

(2) L. Zhang and B. G. Thomas: *ISIJ Int.*, **43**(2003), 271.

(3) Ø. Grong: Metallurgical Modelling of Welding-2nd Ed., The Institute of Materials, London, (1997), 387-476.

(4) H. K. D. H. Bhadeshia: Bainite in Steels, The Institute of Materials, London, (1992), 245-287.

(5) K. W. Lange: *Int. Mater. Rev.*, **33(**1988), 53.

(6) A. Nicholson and T. Gladman: *Ironmaking Steelmaking*, **13**(1986), 53.

(7) F. J. Barbaro, P. Krauklis and K. E. Easterling: *Mater. Sci. Technol.*, **5**(1089), 1057.

(8) T. –K. Lee, H. J. Kim, B. Y. Kang and S. K. Hwang: *ISIJ Int.*, **40**(2000), 1260.

(9) R. A. Ricks, G. S. Barritte and P. R Howell: Proc. Int. Conf. on Solid-Solid Phase Transformations, The Metallurgical Society of AIME, Pittsburgh, Pennsylvania, USA, (1981), 463.

(10) Ø. Grong and D. K. Matlock: *Int. Met. Rev.*, **31**(1986), 27.

(11) A. R. Mills, G. Thewlis and J. A. Whiteman: *Mater. Sci. Technol.*, **3**(1987), 1051.

(12) S. S. Babu, S. A. David, J. M. Vitek, K. Mundra and T. Debroy: *Mater. Sci. Technol.*, **11**(1995), 186.

(13) G. Thewlis, W. T. Chao, P. L. Harrison and A. J. Rose: *Mater. Sci. Technol.*, **24**(2008), 771.

(14) F. Ishikawa, T. Takahashi and T. Ochi: *Metall. Mater. Trans. A*, **25A**(1994), 929.

(15) C. van der Eijk, Ø. Grong and J. Walmsley: *Mater. Sci. Technol.*, **16**(2000), 55.

(16) J. H. Shim, Y. J. Oh, J. Y. Suh, Y. W. Cho, J. D. Shim, J. S. Byun and D. N. Lee: *Acta Mater.*, **49**(2001), 2115.

(17) A. Ohmori, F. Kawabata and K. Amano: Patent EP 1 035 222 A1, (2000).

(18) Ø. Grong and O. S. Klevan: Patent WO 2001/57280, (2001).

(19) P. Grahle, R. Ruch and H. Stiegeler: Patent WO 2005/026396, (2005).

(20) G. Thewlis: *Mater. Sci. Technol.*, **22**(2006), 153.

(21) W. G. Wilson, D. A. R. Kay and A. Vahed: *JOM*, **26**(1974), 14.

(22) W. K. Lu and A. McLean: *Ironmaking Steelmaking*, **1**(1974), 228.

(23) S. S. Babu: *Curr. Opin. Solid State Mater. Sci.*, **8**(2004), 267.

(24) Ø. Grong, L. Kolbeinsen, C. van der Eijk and G. Tranell: *ISIJ Int.*, **46**(2006), 824.

(25) T. B. Massalski: Binary alloy phase diagrams, American Society for Metals, Ohio, (1986), 737, 1006, 1111 and 1472.

(26) V. Raghavan: *Journal of Phase Equilibria and Diffusion*, **25**(2004), 371.

(27) E. E. Underwood: Quantitative Stereology, Addison-Wesley Publishing Company, Menlo Park, California, (1970), 5.

(28) K. E. Kohler and S. M. Gill: *Computers and Geosciences*, **32**(2006), 1259.

Part V: Up-scaled production of CeS-based grain refiners for steels

5.1 Introduction

A fine grain structure in steel is usually achieved by combining heat treatment and thermo-mechanical processing. The energy saving potential of applying cheaper and faster strengthening methods is great and highly interesting in a time where access to energy is predicted to decline. A more economic approach would be to add a specially designed master alloy with the ability to nucleate a fine grain structure in steel. For example, it is well known from low-alloy steel weld metals that intragranular nucleation of acicular ferrite at oxides and sulphides inclusions may results in a fine interlocking microstructure within the as-deposited material[1-4]. The phenomenon has later been transferred to wrought steels products, leading to the introduction of the titanium deoxidised steels in the nineties[5-8]. Currently, a wide variety of different steels in which non-metallic inclusions are used to control the microstructure evolution during solidification and/or in the solid state have been patented, both in Europe and Japan[9-11]. This reflects an increasing interest among the international steel manufacturers to exploit the possibility offered by the technology to produce new low-cost steel grades with unique transformation characteristics on a commercial basis.

One of the most promising systems which has been investigated the recent years is the cerium-sulphur system[12,13]. Cerium has a strong affinity to sulphur and will, almost always, form a compound with sulphur when both elements are present in molten steel[14,15]. A fine distribution of CeS particles in the steel matrix during the austenite to ferrite transformation can shift the nucleation process from the austenite grain boundaries to sites located intragranularly[12,13,16-18]. However, such particles must be sufficiently small to be harmless from a toughness point of view[19,20], but at the same time large enough to act as potent nucleation sites during phase transformation[21-23]. A very fine and narrow particle size distribution close to 1 μm should therefore be aimed at when manufacturing a grain refiner[24]. If the particles size is significantly larger than this, the particles number density will drop rapidly, which makes grain nucleation in steel at such sites less likely. A possible counter measure would be to add the master alloy in larger quantities. Unfortunately, modern steelmaking involving continuous casting does not allow large amounts of ferroalloys to be added late in the process due to the practical problems this will cause in terms of a severe temperature drop and incomplete alloy dissolution and mixing in the liquid. This means that the grain refiner needs to be highly concentrated in order to maintain a high nucleation potential. For continuously cast steel, a sulphur content between 5 and 10 wt% S in the form of small (one micrometer-sized) sulphide particles should be aimed at[24].

In Part IV of the thesis, it was shown that small samples (0.8 g) of CeS-based grain refiners could be manufactured from high purity materials of γ-Ce, Al and Ce_2S_3. The charge mixtures were melted and superheated to 2000 ^{o}C within tantalum crucibles under the protection of cleaned argon using a dedicated laboratory furnace. Due to the small charge volumes involved and the reactive nature of cerium, excessive oxidation of the samples will occur unless the partial pressure of oxygen in the furnace is kept extremely low. However, rapid heating, in combination with the oxygen scavenging effect provided by the heated graphite parts of the furnace, have proved to be sufficient to restrict the supply of oxygen from the shielding gas. The main constituent phases detected in the as-solidified samples are CeS, Ce_3Al, CeAl and γ-Ce, where the CeS phase constitutes a discontinuous dendritic network within the grain refiners. The indications are that pure cerium can dissolve about 6 wt% S at 2000 ^{o}C, which drops to 4.1 wt% at 2 wt% Al added and further to 3.3 wt% at 5 wt% Al added. Aluminium, which has a stabilising effect on the grain refiner during storage in air, should thus be limited if the highest possible sulphur solubility is desired in the liquid state.

In Part V of this thesis, attempts will be made to up-scale the production of the CeS-based grain refiners. Thus, batches of about 0.5 kg will be produced from high purity charge materials of γ-Ce and Ce_2S_3 within a suitable molybdenum crucible using an inductive heating chamber furnace filled with pure argon. As discussed in Part II of the thesis, the indications are that the oxygen pick-up by the molten cerium should be limited by the small surface area to volume (A/V) ratio of the melt compared to that experienced in the small-scale experiments. Still, additional oxygen-cleaning of the shielding gas is needed using a titanium containing resistance furnace, which acts as an efficient oxygen scavenger at temperatures above 600 ^{o}C. Furthermore, attempts will be made to re-melt and rapidly solidify some of the produced grain refiners using melt spinning. This is done to analyse the effect of quenching on the resulting particle size distribution in the grain refiners. Finally, a new up-scaled production method for rapid solidification of CeS-based grain refiners will be suggested, which has the potential for becoming an industrial method in the future.

5.2 Experimental

In the following, the experimental setup will be presented in more details. Some of the experimental techniques used in this investigation have been described in the previous parts of the thesis, including:

- Microprobe investigation (Part II)

- Optical microscopy (Part II)
- Volume fraction measurements (Part IV)

5.2.1 Charge materials and sample preparation procedures

The charge mixtures were prepared from high purity raw materials of γ-Ce and Ce_2S_3, all with purity greater than 99.9%. These were obtained from different commercial manufacturers. To prevent the materials from oxidising, an argon-filled glove box with oxygen and humidity levels <<0.1 ppm was used for storage. The materials were first weighed inside the glove box and then transported inside an argon-filled container to the vacuum furnace unit where they were charged into the Φ 80 mm diameter molybdenum crucible. Note that molybdenum was chosen in these up-scaled melting trials because it is a cheaper refractory metal compared to tantalum and more commercially available.

5.2.2 Furnaces

5.2.2.1 Inductive heating chamber furnace

Figure 5.1 shows an image of the main parts of the furnace used in the up-scaled production of the CeS-based grain refiners. It consists of a vacuum chamber equipped with an induction coil capable of heating crucibles with a diameter up to 100 mm at a maximum power input of 20 kW. The coil is tiltable from the outside. When emptying the crucible the molten material is solidified in the water cooled copper mould located just below the coil, as indicated in Figure 5.1. At the same time, the temperature is carefully logged using a multi-wavelength pyrometer (FMP2), which points directly towards the melt. The FMP2 pyrometer operates in the temperature range between 800 - 2500 ^{o}C with an accuracy of ± 0.25 - 0.75% on non-grey targets.

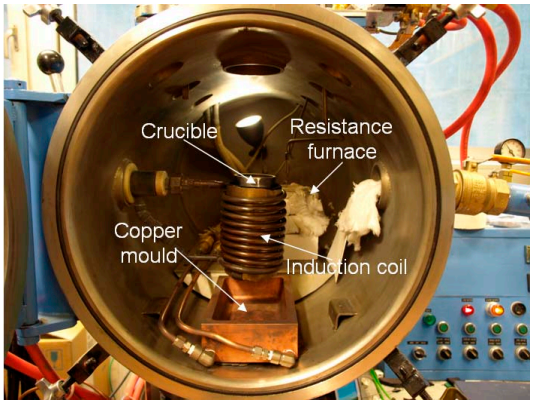

Figure 5.1 Photograph of the inductive heating chamber furnace used in the up-scaled melting experiments.

During melting and superheating due care must be taken to avoid excessive oxidation of the cerium charge material. Therefore, the chamber is first evacuated to about 10^{-6} mbar using a diffusion pump and then back-filled with 99.999% pure argon to reach the desired operating pressure of 650 mbar. Also additional rinsing of the protective atmosphere inside the chamber is carried out, using an electric resistance furnace filled with titanium. When the titanium is heated to about 600 ^{o}C its affinity towards oxygen is sufficiently high to restrict the supply of oxygen to the molten cerium during the melting trials.

5.2.2.2 Melt spinner

The melt spinner is an inductive heating furnace constructed for rapid solidification of molten metals. Figure 5.2 shows a schematic drawing of the main parts of the furnace. The design is simple; the charge is melted and superheated in a Φ 20 mm diameter tantalum crucible, as shown in Figure 5.2. When the desired temperature is reached, the molten material is forced to flow out through the 1 mm hole in the bottom of the crucible, using argon pressure, and then rapidly solidified on the spinning copper wheel. A vacuum pump is connected to the crucible which during heating prevents the molten material to run out prematurely, i.e. when the pressure starts to build up inside the crucible due to S_2(g) gas evolution.

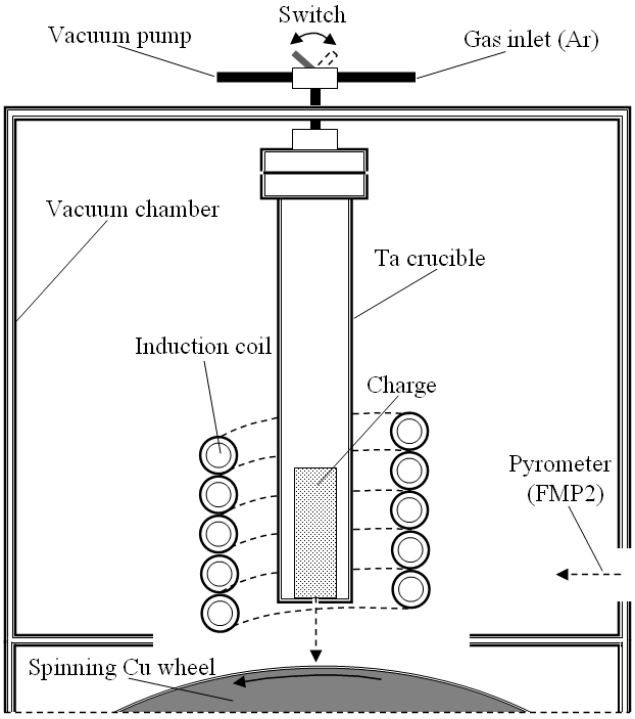

Figure 5.2 Schematic drawing of the main parts of the melt spinner used in the rapid solidification experiments.

The furnace is also provided with a vacuum chamber and pumping system capable of evacuating down to about 0.02 mbar. During the experiments the furnace operates at a 650 mbar argon pressure with a purity of 99.999%. This, together with rapid heating and cooling of the melt, which kinetically suppresses the oxygen absorption from the shielding gas, is sufficient to prevent cerium from oxidising inside the melt spinner.

During melting, superheating and cooling of the melt inside the furnace, the Ta crucible temperature is monitored continuously using the FMP2 pyrometer, as shown schematically in Figure 5.2.

5.2.3 Charge preparation and melt spinning experiments

Two different levels of sulphur additions were investigated in the present work, i.e. 2 and 4 wt% S, as shown in Table 5.1.

Table 5.1 Target chemical compositions of the two different charge mixtures investigated. The corresponding sample weight is also included.

Sample No.	S added	Balance	Mass
1	2 wt%	Ce	642
2	4 wt%	Ce	489

The two charge mixtures (samples No. 1 and 2) were melted and superheated to about 1500 and 1800 ^{o}C, respectively inside the inductive heating chamber furnace. After cooling down to room temperature, approximately 25 g were cut from sample No. 1 and prepared for an additional experiment using the melt spinner. In the melt spinner the sample was melted and superheated to about 1550 ^{o}C and then rapidly solidified onto the spinning copper wheel rotating at 2000 rpm.

5.3 Results

The main results from the metallographic investigation and the complementary phase identifications are summarised below.

5.3.1 Characterisation of sample No. 1 produced in the inductive heating chamber furnace

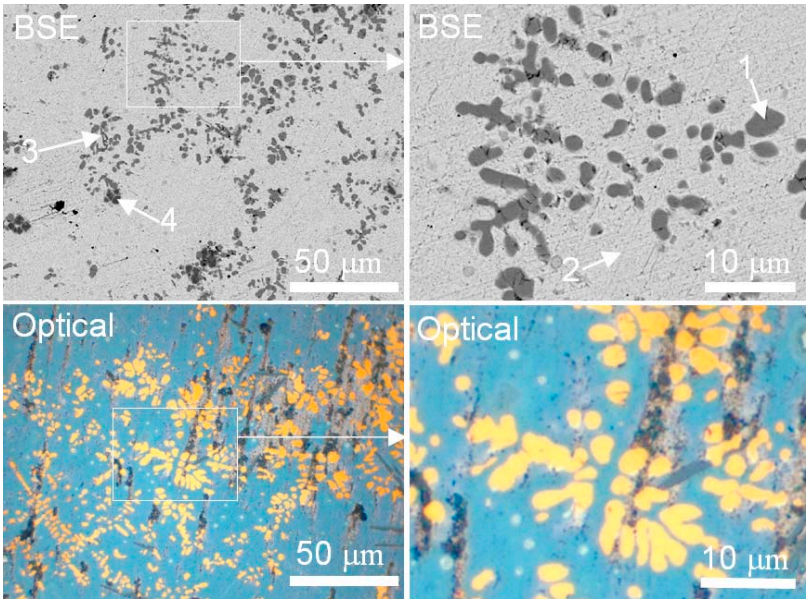

Figure 5.3 Optical and BSE micrographs of sample No. 1 at low and high magnification. The arrows indicate the position of the four point analyses reported in Table 5.2.

Figure 5.3 shows two optical and two BSE images at low and high magnification of sample No. 1 produced in the inductive heating chamber furnace. The four WDS point analyses shown in

Table 5.2 were carried out at the surface positions indicated by arrows in the electron micrographs.

Table 5.2 Point analyses of various phases detected in sample No 1. The numbers are given in at%.

No	O	S	Ce	Mo
1	1.6	48.2	50.0	0.2
2	14.2	2.7	82.1	1.0
3	38.4	17.3	44.2	0.1
4	3.9	5.2	2.8	88.1

The ratio between the elements found in phase No. 1 points toward CeS. The CeS displays a characteristic yellow colour in the optical micrographs and forms a discontinuous dendritic network within the matrix, as shown in Figure 5.3. It follows that the matrix, corresponding to phase No. 2 in Table 5.2, consists mainly of cerium and oxygen. Because this area shows signs of surface corrosion, it is reasonable to assume that the γ-Ce has been oxidised either during or immediately after the metallographic preparation. It has previously been suggested in Part III and IV of the thesis that this phase most likely is γ-Ce with a surface layer of Ce_2O_3 or CeO_2. In addition, a few needle-shaped particles can be seen within the microstructure. As judged from the point analysis of phase No. 3 in Table 5.2, this phase is probably Ce_2O_2S. Finally, point analysis No. 4 shows high concentration of molybdenum. This molybdenum stems from reactions with the crucible, which at 1500 ^oC has a solubility of about 1 wt% in liquid cerium[25].

5.3.2 Characterisation of sample No. 2 produced in the inductive heating chamber furnace

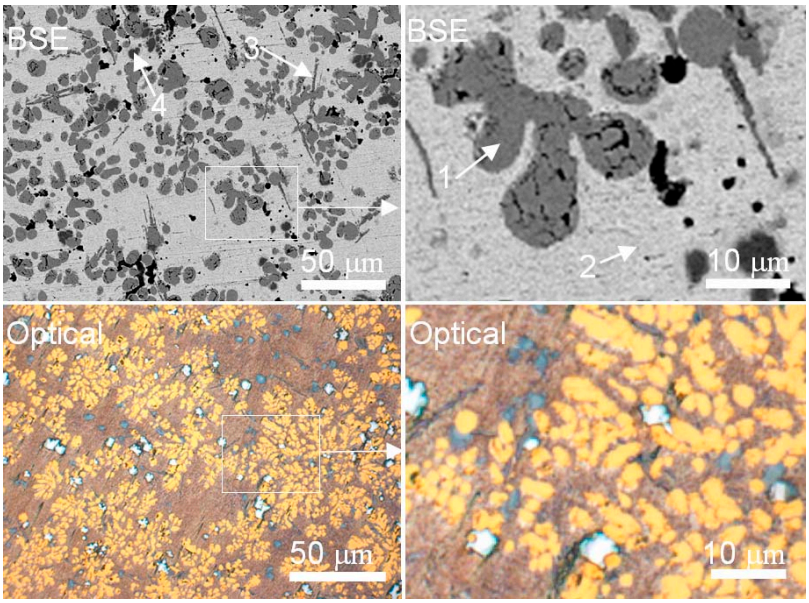

Figure 5.4 Optical and BSE micrographs of sample No. 2 at low and high magnification. The arrows indicate the position of the four point analyses reported in Table 5.3.

Figure 5.4 shows two optical and two BSE images at low and high magnification of sample No. 2 produced in the inductive heating chamber furnace. Note that the arrows in the electron micrographs indicate the position of the four point analyses reported in Table 5.3.

Table 5.3 Point analyses of various phases detected in sample No 2. The numbers are given in at%.

No	O	S	Ce	Mo
1	1.9	48.1	49.8	0.2
2	16.9	0.3	82.8	0.0
3	40.8	18.1	41.0	0.1
4	10.9	4.8	2.1	82.2

The phases shown in position 1 and 2 are CeS and γ-Ce (with a surface layer of CeO_2/Ce_2O_3), respectively. Also in this sample the CeS forms a discontinuous dendritic network similar to that observed in sample No. 1 (see Figure 5.3). Moreover, a few needle-shaped particles can be seen within the microstructure. As judged from the point analysis No. 3, this phase is most likely Ce_2O_2S. The phase observed in position 5 is molybdenum, which can easily be recognised in the optical micrographs as light grey particles. It follows from a comparison with sample No. 1 that the reaction with the crucible is much more extensive at 1800 °C than at 1500 °C. This agrees

well with the Mo-Ce phase diagram, which shows that liquid cerium can dissolve as much as 4 wt% of molybdenum at 1800 ^{o}C[25].

5.3.3 Quantitative volume fraction measurements of phases detected in samples No. 1 and 2 produced in the inductive heating chamber furnace

In Table 5.4, the results from the quantitative metallographic examination of the various phases detected in samples No. 1 and 2 produced in the inductive heating chamber furnace are summarised. Included is also the standard deviation in the measurements, which provides a good indication of the samples homogeneity in each case. Note that the CeS particulates, which were detected in the samples containing the highest amounts of sulphur in Part IV of the thesis, are also present in samples No. 1 and 2 (not shown here). This means that sulphur saturation is reached both at 1800 and 1500 ^{o}C under the prevailing circumstances. The CeS particulates are, however, not included in the quantitative volume fraction measurements. This is because they form in regions of the melt already being saturated with respect to sulphur, and are thus of a different physical origin compared to the CeS dendrites.

Table 5.4 Summary of the results from the quantitative volume fraction measurements of the various phases detected in the samples No. 1 and 2.

Sample No.	**Phases detected**			
	CeS	Ce	Ce_2O_2S	Mo
1	0.10 ± 0.03	0.88 ± 0.03	0.01 ± 0.01	0.01 ± 0.01
2	0.29 ± 0.04	0.66 ± 0.04	0.01 ± 0.01	0.04 ± 0.02

As expected, the results in Table 5.4 show that sample No. 2 contains the highest volume fraction of CeS because it has been superheated to the highest temperature, i.e. 1800 ^{o}C. By reducing the superheating temperature to 1500 ^{o}C the CeS volume fraction drops consistently from 0.29 to 0.10, reflecting a corresponding drop in the sulphur solubility in liquid cerium.

5.3.4 Characterisation of sample No. 1 following remelting and subsequent quenching in the melt spinner

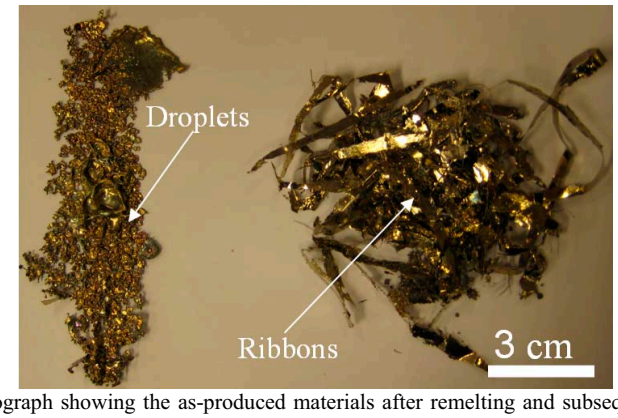

Figure 5.5 Photograph showing the as-produced materials after remelting and subsequent quenching of sample No. 1 in the melt spinner.

Figure 5.5 shows a photograph of the as-solidified materials produced in the melt spinning experiment. In this case, about 50% of the superheated melt was rapidly quenched onto the spinning copper wheel as ribbons, as shown in Figure 5.5. The remaining half did solidify as droplets, probably on the bottom wall of the furnace. Moreover, the characteristic yellow colour of the ribbons indicates a high concentration of CeS within the as-quenched material.

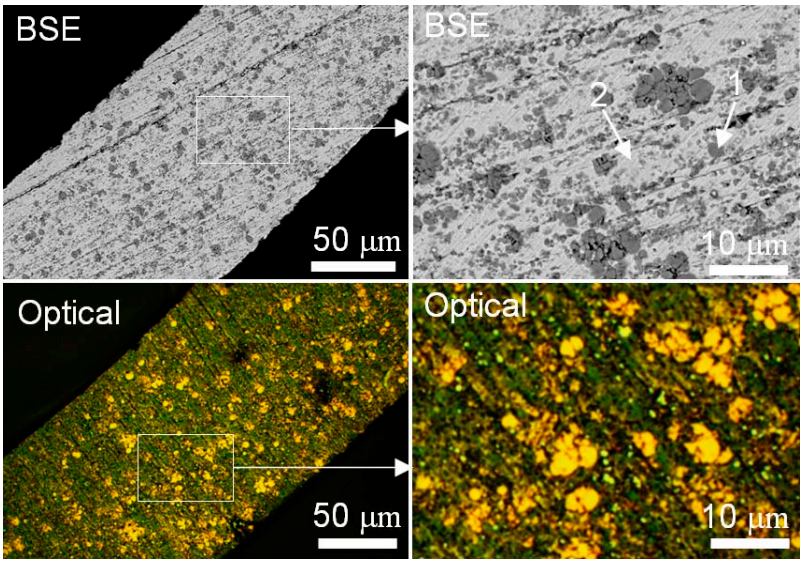

Figure 5.6 Optical and BSE micrographs at low and high magnification of ribbons from sample No. 1 produced in the melt spinning experiment. The arrows indicate the position of the four point analyses reported in Table 5.5.

Figure 5.6 shows two optical and two BSE images at low and high magnification of the ribbons from sample No. 1 produced in the melt spinner. The arrows in the BSE micrograph indicate the position of the two point analyses reported in Table 5.5. Note that the optical and the BSE images are taken from different parts of the surface.

Table 5.5 Point analyses of various phases detected in ribbons of sample No. 1 after remelting and rapid solidification in the melt spinner. The numbers are given in at%.

No	O	S	Ce	Mo	Ta
1	2.2	48.3	49.4	0.1	0.0
2	14.1	0.1	84.8	1.0	0.0

It follows from Table 5.5 that the two phases observed in position 1 and 2 are CeS and γ-Ce (with a surface layer of CeO_2/Ce_2O_3), respectively. The CeS appears in the optical micrographs as yellow spherical-shaped particles. As judged from the images in Figure 5.6, the size of the CeS particles is within the range from 1 to 5 μm. Some molybdenum is also present within the microstructure. These appear as light grey particles in the optical micrograph. Furthermore, no evidence of Ce_2O_2S formation could be observed in the investigated ribbons, which indicates a good oxygen control during the melt spinning experiments.

The two micrographs in Figure 5.7 refer to the droplets which were produced from sample No. 1 in the melt spinning experiment (see Figure 5.5), and give further information about the morphology and distribution of the CeS particles in the as-quenched material. Also in this case the CeS appears as characteristic yellow spherical-shaped particles within the cerium matrix. It follows that most of the particles are less than 3 μm in size, which means that these droplets also have been rapidly cooled during solidification.

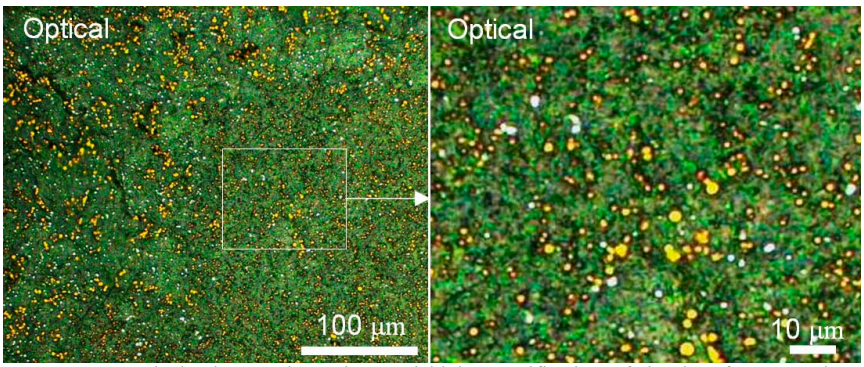

Figure 5.7 Two optical micrographs at low and high magnification of droplets from sample No. 1 produced in the melt spinning experiment.

Finally, Figure 5.8 shows an additional optical micrograph of the as-solidified microstructure of the droplets produced in the melt spinner. In this image some large CeS particulates are also be observed. They are probably remnants of CeS in the charge material being produced in the inductive heating chamber furnace, which during remelting to 1550 ^{o}C are on the verge to dissolve.

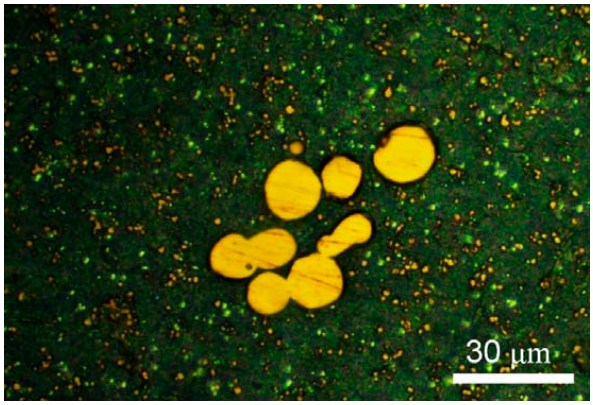

Figure 5.8 Optical micrograph of droplets from sample No. 1 produced in the melt spinning experiment. Note that the large CeS particulates being seen in the image are probably remnants of CeS in the charge material, which during remelting to 1550 ^{o}C are on the verge to dissolve.

5.4 Discussion

In the following, the conditions for CeS formation in the up-scaled laboratory experiments will be discussed in more detail.

5.4.1 Phase relations and sulphur solubility in CeS-based grain refiners

The results from the quantitative phase detection show that the as-solidified microstructures in samples No. 1 and 2 mainly consist of CeS and γ-Ce. Only small amounts of the Ce_2O_2S contamination phase could be observed. This indicates a good oxygen control during melting, superheating and quenching.

Moreover, it is evident that most of the CeS forms by reactions between dissolved sulphur and cerium during cooling of the samples being produced in the inductive heating chamber furnace. At the same time some large CeS particulates are present in parts of the samples, which are remnants of Ce_2S_3 sulphur source. As shown in Part IV of the thesis, the presence of these CeS particulates means that the two-phase “Liq + CeS” region has been entered both in samples No.

1 and 2. Hence, the CeS volume fraction data in Table 5.4 provide a good indication of the sulphur solubility in liquid cerium at 1500 and 1800 ^{o}C, which on a mass basis corresponds to sulphur content of 1.8 and 4.0 wt%, respectively.

5.4.2 Size and morphology of CeS particles in as-quenched samples

The results from the metallographic examination of sample No. 1 after remelting and quenching in the melt spinner show that a fine distribution of CeS particles can be obtained in the grain refiners using rapid solidification. As a matter of fact, the indications are that a mean particle size close to 1 μm is achievable by means of this technique. As pointed out in Part I of the thesis, such particles are sufficiently large to act as efficient nucleation sites for acicular ferrite in steels during the austenite to ferrite transformation, without being harmful with respect to toughness. Furthermore, rapid cooling has also a marked effect on the morphology of the CeS particles, which now appear to be spherical rather than dendritic in nature. This is also beneficial from a toughness point of view.

5.4.3 Long-term stability of the CeS-based grain refiners produced in the inductive heating chamber furnace

Figure 5.9 shows a cross-section micrograph of sample No. 2 re-examined after 4 months of air exposure. The image shows clear indications of oxide layer formation on the surface of the grain refiner. The surface oxide layer thickness is about 90 μm, as shown in Figure 5.9. This is not large compared to the total thickness of the metal piece examined. However, in a rapidly solidified metal ribbon this surface oxidation would become a problem. Therefore, storage of the CeS-based metal ribbons in a sealed argon filled container is probably necessary to avoid disintegration.

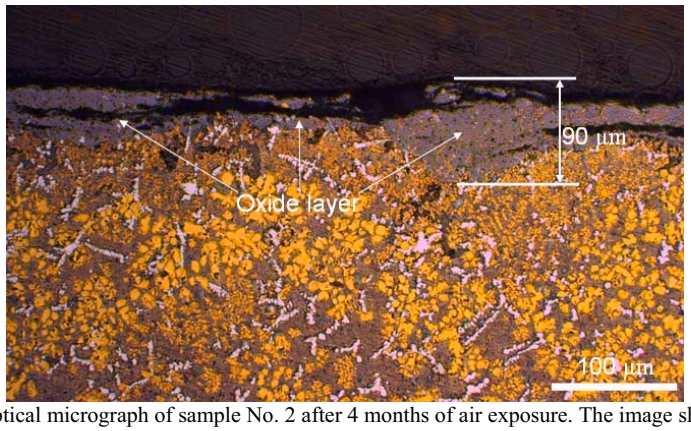

Figure 5.9 Optical micrograph of sample No. 2 after 4 months of air exposure. The image shows evidence of oxide formation on the surface of the grain refiner.

5.4.4 Improved production method for CeS-based grain refiners involving the use of rapid solidification

In the future, new and better production methods for CeS-based grain refiners are needed, which will allow large quantities of materials to be melted, superheated and rapidly quenched in a single batch operation. One possible method, which is commercially available to day, is gas atomization[26,27]. In this process, ultra fine metal powder particles ranging from 15 to 700 μm in diameter can be produced at cooling rates approaching 10^6 °C/s[27]. Figure 5.10 shows a schematic drawing of a possible gas atomization unit which can be used for full-scale production of CeS-based grain refiners.

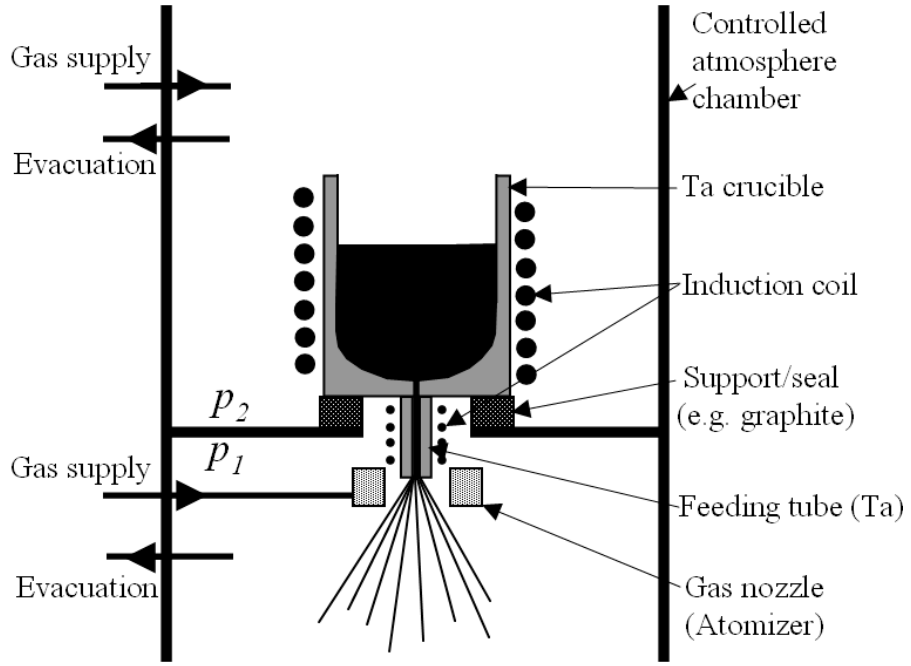

Figure 5.10 Schematic drawing of a gas atomization unit. The charge materials are inductively heated and superheated in a Ta crucible. At the desired temperature the melt is forced to flow out through the feeding tube by a pressure difference between the upper and lower part of the chamber ($p_2 > p_1$) and subsequently rapidly quenched by atomization in the gas nozzle assembly.

The equipment shares a lot of similarities with the traditional inductive heating camber furnace used in the up-scaled laboratory experiments; i.e. the use of a controlled atmosphere chamber and an inductive heated crucible. In this particularly case a tantalum crucible or at least a crucible with tantalum lining should be used to ensure the lowest possible contamination of the

cerium melt. Furthermore, the pressure in the upper and lower parts of the chamber (p_2 and p_1) should be controlled independently, as illustrated in Figure 5.10. Thus, during melting and superheating, the upper chamber is run with an underpressure ($p_2 < p_1$) to prevent the melt escaping prematurely, and during subsequent atomization, with an overpressure ($p_2 > p_1$) to guarantee steady flow of liquid from the melt through the feeding tube. This is the same principles as the one used in the melt spinning experiment. Additional heating of the feeding tube is also required to maintain the necessary fluidity of the liquid cerium until it enters the gas atomization nozzle, as shown schematically in Figure 5.10.

The heart of the atomization equipment is the gas nozzle (atomizer) assembly, where the liquid metal is solidified in the form of metal powder particles. A variety of nozzle designs exists to day[28-32], but the most frequently used ones are the free-fall[33] and the close-coupled[34,35] nozzles, the later being the far most efficient one. Gas atomization is a complex process involving a wide array of physical phenomena. Somewhat simplified, it can be understood as a disintegration process of liquid metal, as gas rapidly expands out of the nozzle at supersonic velocities[35]. A schematic drawing of the break up process of the liquid metal into droplets in a close-coupled nozzle is shown in Figure 5.11.

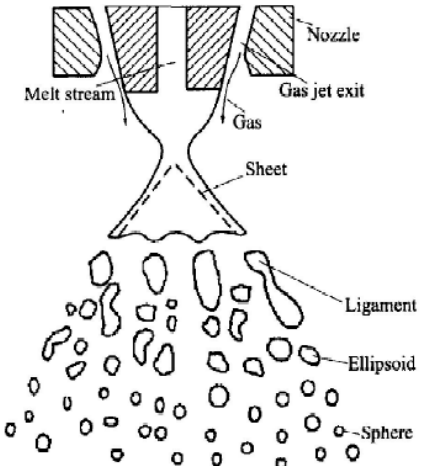

Figure 5.11 Schematic illustration of the fragmentation process of liquid metal into small spherical particles in a close-coupled nozzle during gas atomization[36].

Usually nitrogen gas is used for this task, but also argon and helium systems are available. For production of CeS-based grain refiners, purified argon gas should be used.

The relations between the many parameters controlling the cooling rate and efficiency of the atomization process, e.g. superheat, nozzle geometry, flow rates, material properties, etc, are very complex and have not yet been fully understood[37,38]. Unravelling these parameters here is thus beyond the scope of this thesis. Only in collaboration with a business partner being in possession of such knowledge and equipments it is possible to develop these ideas further and determine whether full-scale production of CeS-based grain refiners by gas atomization can be realised in the future.

5.5 Conclusions

The basic conclusions that can be drawn from this investigation are as follows:

1. Up-scaled production of CeS-based grain refiners is possible from high-purity charge materials of cerium and Ce_2S_3, which are melted and superheated within a suitable molybdenum crucible using an inductive heating chamber furnace.

2. By employing a titanium containing resistance furnace for oxygen cleaning the atmosphere inside the inductive heating chamber furnace becomes sufficiently pure to avoid oxidation of the cerium melt during manufacturing of the CeS-based grain refiners. As a result, the content of the Ce_2O_2S contamination phase is seen to be low in the as-cast samples.

3. The main phases detected in the samples produced in the up-scaled laboratory experiments are γ-Ce and CeS. Following casting in a water-cooled copper mould, the CeS constitute a discontinuous dendritic network within the γ-Ce matrix. This CeS is formed by reactions between dissolved sulphur and cerium during cooling through the two-phase “Liq + CeS” region.

4. Re-melting and quenching of the CeS-based grain refiners in the melt spinner show that a fine distribution of spherical-shaped CeS particles with a mean diameter close to 1 μm can be produced using rapid solidification. This particle size is optimal for the intended future application for steel grain refinement.

5. Finally, a new and improved production method for CeS-based grain refiners has been proposed, which allows large quantities of materials to be melted, superheated and rapidly quenched in a single batch operation. The idea here is to use gas atomization as

the main quenching technique for liquid cerium instead of melt spinning in combination with induction heating and bottom tapping of the crucible.

5.6 References

(1) Ø. Grong and D. K. Matlock: *Int. Met. Rev.*, **31**(1986), 27.

(2) A. R. Mills, G. Thewlis and J. A. Whiteman: *Mater. Sci. Technol.*, **3**(1987), 1051.

(3) S. S. Babu, S. A. David, J. M. Vitek, K. Mundra and T. Debroy: *Mater. Sci. Technol.*, **11**(1995), 186.

(4) Ø. Grong: Metallurgical Modelling of Welding-2nd Ed., The Institute of Materials, London, (1997).

(5) J. -S. Byun, J. -H. Shim, Y. W. Cho and D. N. Lee: *Acta Mater.*, **51**(2003), 1593.

(6) H. Goto, K. -I Miyazawa and K. Tanaka: *ISIJ Int.*, **35**(1995), 286.

(7) J. -H. Shim, Y. -J. Oh, J. -Y. Suh, Y. W. Cho, J. -D. Shim, J. -S. Byun and D. N. Lee: *Acta Mater.*, **9**(2001), 2115.

(8) C. van der Eijk, Ø. Grong and J. Walmsley: *Mater. Sci. Technol.*, **16**(2000), 55.

(9) A. Ohmori, F. Kawabata and K. Amano: Patent EP 1 035 222 A1, (2000).

(10) Ø. Grong and O. S. Klevan: Patent WO 2001/57280, (2001).

(11) P. Grahle, R. Ruch and H. Stiegeler: Patent WO 2005/026396, (2005).

(12) G. Thewlis: *Mater. Sci. Technol.*, **22**(2006), 153.

(13) G. Thewlis, W. T. Chao, P. L. Harrison and A. J. Rose: *Mater. Sci. Technol.*, **24**(2008), 771.

(14) W. G. Wilson, D. A. R. Kay and A. Vahed: *JOM*, **26**(1974), 14.

(15) W. K. Lu and A. McLean: *Ironmaking Steelmaking*, **1**(1974), 228.

(16) T. Koseki and G. Thewlis: *Mater. Sci. Technol.*, **21**(2005), 867.

(17) S. S. Babu: *Current Opinion in Solid State & Materials Science*, **8**(2004), 267.

(18) H. K .D. H. Bhadeshia and L. E. Svensson: Mathematical Modelling of Weld Phenomena, Institute of Materials, London, (1993), 109-177.

(19) K. W. Lange: *Int. Mater. Rev.*, **33(**1988), 53.

(20) A. Nicholson and T. Gladman: *Ironmaking Steelmaking*, **13**(1986), 53.

(21) F. J. Barbaro, P. Krauklis and K. E. Easterling: *Mater. Sci. Technol.*, **5**(1089), 1057.

(22) T. -K. Lee, H. J. Kim, B. Y. Kang and S. K. Hwang: *ISIJ Int.*, **40**(2000), 1260.

(23) R. A. Ricks, G. S. Barritte and P. R Howell: Proc. Int. Conf. on Solid-Solid Phase Transformations, The Metallurgical Society of AIME, Pittsburgh, Pennsylvania, USA, (1982), 463.

(24) Ø. Grong, L. Kolbeinsen, C. van der Eijk and G. Tranell: *ISIJ Int.*, **46**(2006), 824.

(25) O. Madelung (Editor): Landolt-Börnstein - Group IV Physical Chemistry, Springer-Verlag, **5c**(1993), 1.

(26) L. V. M. Antony and R G. Reddy: *JOM*, (March 2003), 14.

(27) L. A. Jacobson and J. McKittrick: *Materials Science and Engineering*, **Rll**(1994), 355.

(28) A. Allimant, M. P. Planche, Y. Bailly, L. Dembinski and C. Coddet: *Powder Technology*, **190**(2009), 79.

(29) L. Achelis and V. Uhlenwinkel: *Materials Science and Engineering A*, **A477**(2008), 15.

(30) I. E. Anderson and R. L. Terpstra: *Materials Science and Engineering A*, **A326**(2002), 101.

(31) S. Markus, U. Fritsching and K. Bauckhage: *Materials Science and Engineering A*, **A326**(2002),122.

(32) S. Lagutkin, L. Achelis, S. Sheikhaliev, U. Sheikhali V. Uhlenwinkel and V. Srivastava: *Materials Science and Engineering A*, **A383**(2004), 1.

(33) D. Singh, R. K. Dube and S. C. Koria: *Powder Metallurgy*, **42**(2003), 181.

(34) R. Unal: *Powder Metallurgy*, **50**(2007), 302.

(35) R. Unal: *Journal of Materials Processing Technology*, **180**(2006), 291.

(36) H. -W. Ouyang, B. -Y. Huang, X. Chen and W. -T. Yu: *Transactions of Nonferrous Metals Society of China*, **15**(2005), 985.

(37) S. P. Mates and G. S. Settles: *Advances in Powder Metallurgy & Particulate Materials*, **1**(1996), 67.

(38) S. P. Mates and G. S. Settles: *Atomization and Sprays*, **15**(2005), 1.